HIGH PERFORMANCE COMPUTING APPLICATION: SOLAR DYNAMO MODEL PROJECT II; CORONA AND HELIOSPHERE COMPONENT INITIALIZATION, INTEGRATION AND VALIDATION

Donald C. Norquist

Boston College, Trustees of Boston College
140 Commonwealth Ave.
Chestnut Hill MA 02467-3853

24 June 2015

Final Report

AIR FORCE RESEARCH LABORATORY
Directed Energy Directorate
3550 Aberdeen Ave SE
AIR FORCE MATERIEL COMMAND
KIRTLAND AIR FORCE BASE, NM 87117-5776

NOTICE AND SIGNATURE PAGE

This report was cleared for public release by the Air Force Research Laboratory RD Public Affairs Office and is available to the general public, including foreign nationals. Copies may be obtained from the Defense Technical Information Center (DTIC) (http://www.dtic.mil).

AFRL-RD-PS-TR-2015-0028 HAS BEEN REVIEWED AND IS APPROVED FOR PUBLICATION IN ACCORDANCE WITH ASSIGNED DISTRIBUTION STATEMENT.

//Jeffrey Yepez//   // James A. Theiss//

_____   _____
JEFFREY YEPEZ , DR-III   JAMES A. THEISS. Lt. Col, USAF
Program Manager   Deputy, Space E-O Division

This report is published in the interest of scientific and technical information exchange, and its publication does not constitute the Government's approval or disapproval of its ideas or findings.

REPORT DOCUMENTATION PAGE

1. REPORT DATE *(DD-MM-YYYY)*	2. REPORT TYPE	3. DATES COVERED *(From - To)*
24-06-2015	Final Report	02/08/2013-08/30/2013

4. TITLE AND SUBTITLE	5a. CONTRACT NUMBER
High Performance Computing Application: Solar Dynamo Model Project II, Corona and Heliosphere Component Initialization, Integration and Validation	FA9453-13-1-0253
	5b. GRANT NUMBER
	5c. PROGRAM ELEMENT NUMBER

6. AUTHOR(S)	5d. PROJECT NUMBER
Donald C. Norquist	
	5e. TASK NUMBER EF122892
	5f. WORK UNIT NUMBER D076

7. PERFORMING ORGANIZATION NAME(S) AND ADDRESS(ES)	8. PERFORMING ORGANIZATION REPORT NUMBER
Boston College, Trustees of Boston College 140 Commonwealth Ave. Chestnut Hill MA 02467-3853	

9. SPONSORING / MONITORING AGENCY NAME(S) AND ADDRESS(ES)	10. SPONSOR/MONITOR'S ACRONYM(S)
Air Force Research Laboratory 3550 Aberdeen Avenue SE Kirtland AFB, NM 87117-5776	AFRL/RDSM
	11. SPONSOR/MONITOR'S REPORT NUMBER(S) AFRL-RD-PS-TR-2015-0028

12. DISTRIBUTION / AVAILABILITY STATEMENT

Approved for public release; distribution is unlimited.

13. SUPPLEMENTARY NOTES

14. ABSTRACT

This report reviews the status of current day solar corona and inner heliosphere modeling; acquiring and executing one of more state-of-art solar corona (SC) and inner heliosphere (IH) research models, including common formulations for beginning (or initializing) numerical simulations. This is should help toward developing and demonstrating similar algorithms that provide initial and boundary values to support SC and IH components of a new solar dynamo model.

15. SUBJECT TERMS

solar plasma boundary conditions, solar corona and inner heliosphere modeling, solar dynamo, Magnetohydrodynamics Around a Sphere (MAS), Space Weather Modeling Framework (SWMF)   Space Weather Modeling Framework (SWMF)

16. SECURITY CLASSIFICATION OF:			17. LIMITATION OF ABSTRACT	18. NUMBER OF PAGES	19a. NAME OF RESPONSIBLE PERSON
a. REPORT	**b. ABSTRACT**	**c. THIS PAGE**	SAR	88	Jeffrey Yepez
Unclassified	Unclassified	Unclassified			**19b. TELEPHONE NUMBER** *(include area code)*

This page was intentionally left blank.

TABLE OF CONTENTS

Approved for public release: distribution is unlimited.

LIST OF FIGURES

1.0 SUMMARY

This grant was originally entitled "High Performance Computing Application: Solar Dynamo Model, Project II: Corona and Heliosphere Component Initialization, Integration, and Validation". BC personnel also submitted a first grant entitled, "High Performance Computing Application: Solar Dynamo Model Project I: Corona and Heliosphere Component Boundary Conditions and Initial State." During the procurement process, the Project I proposal was not awareded. Project II was subsequently awarded several months later. This denial of funding for Project I but approval for Project II presented a problem in that the "boundary conditions and initial state" must always be assigned to a model prior to any steps of "initialization, integration, and validation" could be carried out. In fact, the following quote is taken from the Project II proposal: "The project will be conducted in coordination with Project I. Project I focuses on establishing the model initial state on the computational domain grid. Project II extends the model process to preparing a balanced state that is integrated in time producing future simulated state evaluated subjectively and objectively." In order to address the requirements of Project II, we had to therefore take a broader approach to consider all of the normally used stages of preparation of the models for execution.

As a first effort, we conducted an in-depth literature review for Project II, to identify how best to move forward given that Project I was not funded. This literature review began as an in-kind effort before the project was funded and continued after funding was received. This covered several different types and classes of models and examples of both kinematic and magnetohydrodynamic models. As a result of this review, we considered two potential models that could serve as a reference model in Project II, the Solar Corona (SC) and the Inner Heliosphere (IH) models. Both of these were then extensively reviewed, including the study of relevant details of each one. We described the various methods for providing initial and boundary conditions for the Solar Corona model. Details of this extensive review of the literature are presented in the following section.

2.0 INTRODUCTION

The Sun produces light and heat essential to sustain life on Earth. Its consistent provision of energy drives atmospheric processes and enables mankind to generate power to sustain our lifestyles. But the Sun also emanates tremendous output in the form of solar plasma, consisting of charged particles of ions and electrons, along with the accompanying solar magnetic field. Near the Sun, within about 20-25 solar radii (R_s) of its center, the solar corona forms the outermost portion of the solar "atmosphere" capping the lower layers of the photosphere and chromosphere. The corona is characterized by tenuous plasma of low density, very high temperatures, and a complex structure of magnetic field of open (outward extending) and closed (curved loops) lines. Beyond the corona lies the inner heliosphere, formed by the outward expanding plasma and its magnetic field lines, to distances of 2-3 astronomical units (AU, the mean Sun – Earth distance). The solar plasma, magnetic field, and intense disturbances of radiation, particles and magnetic anomalies from the Sun that propagate into solar system make up what we call space weather.

Modern technology can be vulnerable to space weather, especially the solar storms. Communication and navigation satellite system operations can be interrupted or terminated by powerful solar impulses. People involved in space operations and high altitude aviation can be endangered by radioactive particles from the Sun that are accelerated to near relativistic speeds. On the ground, high tension power line networks and long distance pipeline systems can sustain elevated electrical charges that can knock out service or severely damage hardware. We have become more of a target for space weather due to our technological advancement. This fact provides the impetus for understanding our space environment, and ultimately our ability to anticipate solar disturbances and to guard accordingly. The Sun brings life-giving energy but has the potential to deliver adverse blows for which we must be prepared in order to mitigate their effect.

Since the early 1970s when satellites became available as space probes, scientists have attempted to simulate space weather with numerical models. Magnetohydrodynamics (MHD), the study of the motion of charged matter, has formed the basis for space weather modeling. Though progress has been slow due to our inability to make direct (in situ) measurements in the near solar environment, models of the solar corona (SC) and inner heliosphere (IH) have emerged. Major issues remain unsolved, for example the substantial heating in the corona that pushes temperatures much greater than those of the solar surface, and the resulting outward acceleration of the plasma. Much of the research published in the last decade has been devoted to devising and implementing theoretical mechanisms to explain these issues. Some of the models have been used routinely in operational settings to provide some degree of warning of space storms that might impact Earth. Though gains have been made, more about the Sun's processes must be understood and incorporated in SC and IH space weather models.

3.0 METHODS, ASSUMPTIONS AND PROCEDURES

3.1 Literature Review of Solar Corona and Inner Heliosphere Models

The history of SC and IH models is relatively brief yet complex in its effort to realistically simulate solar processes. Generally, coronal and heliospheric realms were modeled separately, primarily due to the thought that impetus for plasma expansion and magnetic structure takes place in the corona while the heliosphere and imbedded planets see their effect. In the following summary, we will briefly touch on the key points that stemmed from the review. More details are included in the respective sections of Appendix A.

In the Introduction, we first gave background to four major methods that have been invoked in modeling the solar corona. Because plasma is so sparse there, the coronal magnetic field can only be inferred from remote sensing of the photosphere. Modeling efforts essentially extend the magnetic field into the corona to estimate its structure. Most coronal modeling is steady-state, based on photospheric magnetic field observations at a fixed time – in this sense, they are diagnostic rather than prognostic.

The four categories of coronal models are potential field source surface (PFSS); force-free field, magnetohyrostatic, and magnetohydrodynamic (MHD). PFSS models assume no coronal electric current as it computes the three-dimensional magnetic field (**B**) on a grid from the

photosphere to a "source surface" typically set at 2-3 R_s. The observed radial magnetic field at the photosphere serves as boundary values for a solution of Laplace's equation of the potential field. This yields spherical harmonics coefficients of the magnetic field components which are evaluated between the photosphere and source surface to obtain the coronal magnetic field estimate. Force-free models allow electric currents, but neglect plasma dynamic pressure and kinetic energy density in favor of magnetic pressure in the lower corona. This leads to a current density that is dependent only on radial distance that permits a straightforward solution of a Helmholtz equation for **B**, but holds only for small regions and is not suitable for global application. Magnetohydrostatic models equate Lorentz force (curl of current density and magnetic field) with the sum of pressure gradient and density times the gravitational potential gradient. One must specify current density to achieve an analytic solution for **B**, which requires imposing its expansion-contraction and its internal shape, a trial-and-error process. The resulting magnetic field energy is unbounded, unsuited for practical use. MHD coronal models are comprehensive in that they represent plasma dynamics, thermodynamics, and electromagnetics physically. While not distinct from IH models, they require inner boundary magnetic field and plasma property values, the latter not currently measured. Equations for conservation of mass, momentum, electromagnetic induction and thermodynamic energy are solved usually in steady-state for **B**, plasma velocity (**V**), temperature (T) and density (ρ). MHD equations are closed by Maxwell's equations, Ohm's law, first law of thermodynamics, and the ideal gas law. Specifying **B** by extension from the photospheric observations and imposing a **V** field assuming global symmetry constitutes the standard initialization for the computational grid. Model integration continues until a physically consistent steady-state is attained. Because of the more physical basis and greater likelihood of realistic solutions, only MHD-type coronal models were considered in the review.

There are two major types of inner heliosphere models: simple kinematic and MHD. Kinematic models propagate solar wind parcels from a rotating corona configuration on a line to Earth at a speed derived from the corona outer boundary magnetic field. They account for parcel interaction in various ways to reduce or increase solar wind speed. A time series of solar wind speed and magnetic field polarity at 3-8 hour intervals is produced at the L1 Lagrangian point near Earth. Three-dimensional MHD IH models are of the same type as used in the corona, but without the equation terms representing coronal heating and plasma acceleration. Also, their computational domain extends from the edge of the corona to past the Earth and is correspondingly more coarse. They draw inner boundary values from the steady-state corona model solutions and rely upon specified states for initializing the rest of the grid. One type of MHD IH model is an extension of the corona model through the inner heliosphere. The other type separately models the inner heliosphere, considered regionally distinct from the corona by greater solar wind speeds. Both types were considered in this review.

We next listed the existing models as found from a Google search on the three topic names:
- Models of the Solar Corona
    - Magnetohydrodynamics Around a Sphere (MAS)
    - Space Weather Modeling Framework (SWMF) Solar Corona (SC)
- Models of the Inner Heliosphere
    - Enlil
    - Space Weather Modeling Framework (SWMF) Inner Heliosphere (IH)

- Combined Models of the Solar Corona and Inner Heliosphere
  - Hayashi
  - Coupled MAS and Enlil (CORHEL)
  - Coupled MAS and MAS-Heliosphere
  - National institute of Information and Communication Technology (NiCT), Japan
  - Solar-Interplanetary Adaptive Mesh Refinement Space-Time Conservation Element and Solution Element (SIP-AMR-CESE)
  - Coupled SWMF SC and IH

All of these models were identified in journal articles found through the Google search. The details of these models constitute about 20 pages of Appendix A and are not repeated in this report. We concentrated only on models that were actively published since the mid-1990s and that would be possible to acquire and execute on available high performance computing assets. These fell into the first two topics above. The hope was that the model descriptions in the article would indicate the most reputable models that could be used as a reference in this project. The following two paragraphs briefly summarize the most relevant findings from our review of stand-alone solar corona and inner heliosphere models.

The physical sophistication of the MAS model increased over its ~ 15 year life time. The original assumption of adiabatic plasma compression and expansion was replaced by a non-adiabatic formulation. It also included energy exchange terms in the thermodynamic energy equation to account for coronal heating. Though MAS evolved through various parameterizations for this effect, like other models, this reflected the continuing controversy over the most important heating mechanisms. In all cases, single-case experiments with and without the enhancements were inhibited by having only a qualitative reference inferred from remote sensor data. Often a formulation was justified if the resulting coronal state had a "better" agreement than an alternative. In constructing the SWMF, the developers concentrated on a modular design of the domain components (including SC and IH) that had common roots in a common adaptive mesh refinement (AMR) grid technique. A lot of focus was placed on "coupling" components of contiguous domains to improve SWMF utility. Only in the last few years have SC, and to a lesser degree IH, received more attention in investigating physical mechanisms for coronal heating. The fact that MAS and SWMF SC are both actively involved in research efforts to improve corona model performance, and were likely to be more accessible due to their domestic sources, improved their candidacy as a reference solar corona model for this project.

In contrast to the significant research activity in improving solar corona models, inner heliosphere models have received less formulation scrutiny in recent times. This is because they are largely free from the complexity of open and closed field lines and coronal heating. However, their performance in simulating plasma properties and the interplanetary magnetic field (IMF) at L1 has been shown to be very sensitive to the steady-state corona model solution from which they draw their inner boundary values. The plasma expansion and compression formulation, though considered less important for IH models, affects plasma temperature, density and speed simulations as evaluated against observations at L1. The Enlil model began as a vehicle for simulation of coronal mass ejections (CME) in their propagation through the inner heliosphere. When Enlil was modified to improve undisturbed large-scale solar wind and IMF,

more realism in heliospheric transient simulations occurred. However, in Enlil experiments in conjunction with the Wang-Sheeley-Arge (WSA) coronal model (PFSS-based) supplying the inner boundary, the author did not include results of his evaluation against observations at L1. WSA and Enlil have recently become the operational solar wind model of the NOAA Space Weather Prediction Center. Very little has been published on the SWMF IH component as a stand-alone model as distinct from the SC model. Like Enlil, its adiabatic plasma expansion-compression formulation removes a need for energy exchange processes in the thermodynamic energy equation. Its credibility is supported by its relationship with SC in using the same AMR computational technique. Its use in tandem with the frequently published SC component research lends to its desirability as an IH candidate for this project.

A conclusion of our literature survey was that characteristics of the plasma flow near the Sun are sufficiently different from solar wind in the inner heliosphere to recommend simulating the processes in separable domains. This requires that they be linked computationally to pass information properly from the Sun to the Earth and beyond. This means that the IH solutions are sensitive to the more complex coronal environment, thus the need for a sound SC model. Though uncertainty remains in coronal plasma heating and acceleration mechanisms, current corona and heliospheric models can be used as a reference standard for further research.

3.2 Acquisition and Experimentation with a Standard SC and IH Model

Based on our review and their apparent availability, we sought to obtain source code of the MAS model and SWMF SC component for the solar corona reference model, and Enlil model and the SWMF IH component for the inner heliosphere standard. Upon contacting the respective model sources, we were advised that the MAS and Enlil model codes could not be acquired due to proprietary and other reasons. We then directed our attention to the SWMF modeling system in order to get the code and documentation to act as the SC and IH reference models for this project.

Appendix B gives details of my experience with downloading the necessary software and documentation from the University of Michigan Center for Space Environment Modeling (CSEM). In Section C of the appendix we describe the download, transfer and introductory testing of the SWMF software suite on the "mana" computer of the Maui High Performance Computing Center (MHPCC). We were approved as a user under a MHPCC project established to support space weather modeling efforts. Section D details our work with the SWMF suite on "riptide" which by that time had replaced mana as the primary supercomputer platform at MHPCC. This work included our process of acclimating to the MHPCC computing environment. MHPCC consulting personnel were helpful in assisting me in this process. Our first step with the primary SWMF code directory was to implement the directions in a README file that we had downloaded with the documentation. It first directed us to create the model documentation set by running a "makefile", which was unsuccessful. We did eventually obtain a complete set of model documentation from the CSEM webmaster, including the "SWMF User Manual, Code Version 2.3" dated April 2013. However, in our subsequent experience with the manual, especially in conducting some of the examples and in plotting model results, we found that the manual was considerably out of date with respect to the software release that we downloaded.

We next attempted to follow the directions of the README file to conduct a standard test of the model on riptide. In the batch mode on four processors ("cores") we ran a provided makefile that was designed to configure SWMF for all of its components (listed on page 41 in Appendix A), compile it to create an executable, run nine tests of various combinations of contiguous components, and compare their outputs with reference outputs. Three of the tests resulted in an exact match with the reference, including "Test 2" which executed SC, IH, and the global magnetosphere component GM. We confirmed this successful test of the components most relevant to this project by running the makefile specifically for Test 2. By reading the standard output that listed the steps taken in the makefile to configure SWMF for these components, bring in the appropriate PARAM.in and LAYOUT.in files that direct the execution, and store the output files, we were able to write a shell script for riptide that attempted to duplicate all of the Test 2 processes using the basic commands documented in the SWMF User Manual. We ran the SC – IH portion script on riptide using 16 cores of a single node, which ran to completion, stored outputs, and saved a restart file so that IH could be coupled with GM in a subsequent restart job. We wrote and ran a second shell script to execute the IH – GM portion of Test 2 with all of the necessary commands to set up, run on 16 cores, and store outputs and a restart file from GM. Comparison of the GM component output with the supplied reference showed an exact match, confirming a successful porting of the necessary SWMF components to riptide and our understanding of their use.

Finally, we conducted two efforts to further our experience with SWMF relevant to the operation and outputs of SC and IH. First, we attempted to run two suggested examples from the SWMF User Manual that (1) executes SC in steady-state for a specified initial date and time and saves a restart file, and (2) runs a restart job that couples SC with IH periodically and executes IH in steady-state. This sequence of jobs was successful and all output files were stored. Second, we attempted to create plots of some of the output files from SC and IH using CSEM-provided IDL source codes. Using options on the PARAM.in directives for saving output, we were able to write files so that the provided "postIDL" program was able to create ASCII output files. I brought them and the CSEM IDL codes back to my Linux workstation that has an IDL license, and attempted to follow directions from an older manual provided by CSEM personnel to create postscript plots. I found that several routines called by the primary plotting codes were not included in the release, again showing inconsistencies between the SWMF software release and its documentation. At the time of this writing, we received additional software from CSEM intended to correct this shortfall, and we will again attempt to plot SC and IH outputs.

3.3 Further Study of the SWMF SC and IH

Section B of Appendix B describes our review of published recent research using the SWMF SC and IH components. As indicated earlier in this report, the bulk of the effort was directed to the solar corona in the researcher's attempts to explain coronal heating and plasma acceleration. Their modifications to SC focused on adding energy transfer function processes to the thermodynamic energy equation. The published papers reviewed all pointed to heating due to Alfvén wave (magnetic field perturbations) turbulence dissipation, which was parameterized in various forms. Tests of the SC formulations involved qualitative comparison of synthetic emission intensity images from the steady-state solutions with observed imagery. While some of

the ad hoc coronal heating terms yielded perceptively improved emission images, researchers acknowledged that complex formulations to improve model performance is probably not as beneficial as accurately representing the actual physical basis for the heating. One of the papers coupled their modified SC component with IH, and evaluated solar wind speed, temperature, and magnetic field magnitude – all were found to be generally less than observed. They attributed the shortfall to an incomplete Alfvén wave-induced heating formulation and a weak magnetogram in SC, but another contributor could be an overly simple plasma compression-expansion method used in IH. The latest publication of SC-based research argued that sufficient power exists in naturally-occurring Alvén waves that is more than enough to explain corona heating and solar wind acceleration. They sought to introduce physically-based terms in the SC momentum and thermodynamic equations to properly represent the effect of Alfvén wave turbulence dissipation. They used what they insisted were observationally-support assumptions in their formulations, including complete absorption of Alvén wave turbulence from the photosphere by the corona. Many additional assumptions were made to construct their parameterizations, such as a Kolmogorov-like dissipation mechanism for energy absorption. In the synthetic emission images from their steady-state outputs, they were able to show similarity with observed images in major features of the Sun including patterns of active regions and coronal holes.

In Section F of Appendix B, we attempted to summarize what the research papers, the SWMF User Manual, and CSEM personnel have conveyed about imposing initial and boundary values for SC and IH executions. The intention of this project was to follow such standard methods in constructing initial and boundary values for the prototype SC and IH components of the proposed solar dynamo model. Some of the common techniques used in recent SWMF SC-based research were: using Carrington rotation magnetograms of the photosphere radial magnetic field, extending the magnetic field into the lower corona using the PFSS model to supply initial **B** values out to the source surface, deriving radial solar wind speed on the source surface using an empirical expression based on the initial **B** field, setting a constant temperature on the inner boundary and an inner boundary density inversely proportional to the square of the source surface solar wind speed. One paper provided a bit more detail on initializing their model executions, which may be helpful in guiding the development of the initial and boundary value generator algorithm for this project. Another useful mention made in the papers was the use of the historical "isothermal Parker solar wind solution" to specify initial conditions for the plasma density and solar wind speed in the model components. Unfortunately, the SWMF User Manual was not as helpful in describing how initial and boundary values are prescribed for the model executions. The primary input to SC is directed in the PARAM.in file by the MAGNETOGRAM command. Its terse description in the manual suggests that the code can be instructed to ingest a file containing the spherical harmonics of the coronal magnetic field that is previously derived from a photospheric magnetogram by the PFSS model. From these spherical harmonics coefficients, the model can determine the three components of the magnetic field at each grid point from the photosphere to the source surface in accordance to the potential field solution. This suggests that the PFSS model is executed on the magnetogram externally to SWMF, and that the SC component simply evaluates the resulting initial **B** at the coordinates of each grid point. This approach might also be used in the proposed initial and boundary value generator algorithm, which would call the PFSS model and apply it to the magnetogram data. It could also contain routines that establish the temperature, density and solar wind speed on grid

points. Then the candidate's grid point coordinates would be read in, and all of the necessary initial and boundary values would be computed for the model component. Finally, we have begun consulting with CSEM personnel to get more details and help with the initial and boundary value specification processes in the SWMF SC. We hope to have answers to questions that will aid in the formulation of the proposed algorithm.

4.0 RESULTS AND DISCUSSION

4.1 Experimentation with the Space Weather Modeling Framework

After contacting the SWMF webmaster, enrolling in their program and downloading model software, we were provided with a set of User Manuals. We installed the SWMF Version 2.3 software on the Mana supercomputer at the Maui High Performance Computer Center (MHPCC) which is located at the DOD supercomputer resource center in Maui, Hawaii. Subsequently, we read through the manuals and set up several experiments involving the Solar Corona component and the IH component. We coupled the Solar Corona model and the Inner Heliosphere model in the restart experiment and ran the IH component also to study state (see Appendix B, sections D and E).

4.2 Example Results from the SWMF Model

The Space Weather Modeling Framework model components of Solar Corona (SC) and Inner Heliosphere (IH) produce two primary types of output that can be displayed graphically. First, the three-dimensional computational grid solution values at a given number of model iterations (*niteration*) for steady state solutions, or simulation time (*tsimulation*) for time dependent (or "time accurate") solutions, are rendered in the three graphical planes of the grid. Second, a time series file of the IH component valid at a "satellite" (in our case, Earth) about the Sun contains model output values at selected real time intervals. The following sections briefly describe each type of output, how they were processed and then displayed as graphical images. The simple contour, streamline and x-y plots shown are for a single experiment of a steady-state SC solution, coupled to the IH, then the subsequent steady-state IH solution.

4.2.1 Creating/Processing Computational Grid Output on 2-D Image Planes. The SWMF PARAM.in file that directs the execution of each model experiment contains a section within the commands for each component called "SAVEPLOT." In this section, the user must specify the number of outputs for plotting listed. Then for each plot desired, three parameters are listed: plotarea, plotvar, and plotform. Plotarea indicates the subset of the computational form that is to be plotted; for example, '3d' is a full 3-D volume. Plotvar indicates the variables to be represented in the output file for plotting; for example, 'MHD' would list the mass density, pressure, and three components of solar wind velocity, magnetic field, and current density. Plotform dictates the form of the output data; for example, 'idl_ascii' as we used in our processing outputs the data in ASCII form in the form that a processing program written in IDL can read. Next is the *niteration* or *tsimulation* interval at which the indicated data is written to a file. For certain choices of plot area, the desired grid spacing of the output may be indicated.

In the model experiments presented in this discussion, we used a plotarea that represents the three axes of the Cartesian computational grid. Plane "x=0" (referred to here as the "y-z" plane) represents the plane passing through Sun center with the perspective at looking at the Sun from Earth (y is left-to-right, or east-to-west in solar orientation, and z is bottom-to-top, or south-to-north). Plane "y=0" ("x-z" plane) passes through the Sun center with the perspective of looking at the Sun from a point 90° to the left (east side) of the Earth's orbit position. Thus it can be viewed as looking at the Sun-Earth plane with the Sun in the center of the image and Earth to (or beyond) the right edge. Plane "z=0" is essentially the ecliptic plane, or the plane described by the disc of the Earth orbiting the Sun.

In the experiment, we ran the SC component from a provided Mt. Wilson Observatory magnetogram of Carrington rotation 1935 (April 14-May 11, 1998). The designated date and time of the steady-state solution was 1 May 1998 at 0 UTC, which designates the Carrington longitude of the rotation at the central meridian (Earth-facing longitude) of the Sun. The computational grid was in Cartesian coordinates extending to ±24 solar radii (R_s) in x, y, and z directions centered on the Sun. SC ran for *niteration* = 200, and we designated a SAVEPLOT output interval of every 10 iterations. The model actually outputs a file for each computational processor ("core") of the computer, representing a designated portion of the computational grid – we used 32 processors of the Maui High Performance Computer Center platform called "riptide" for our experiment. These are the individual processor outputs that are suffixed *.idl. A script called pIDL was provided that combines the *.idl files for each output iteration and creates a full-grid file of the data suffixed by *.out. Also, pIDL can optionally consolidate the individual iteration interval files in sequence into a single file that could be animated. After running pIDL, I obtained files in the form x=0_mhd_1_n0000010.out through n000200, and the same for y=0_mhd_2* and z=0_mhd_3*. Because we planned to use the IDL license at our home computer, we brought the *n000200.out files for x=0, y=0, and z=0 from riptide to our Linux workstation "isr01."

We ran a separate "restart" experiment of the output from SC that was directed by an additional PARAM.in file. Specifying an IH component Sun-centered computational grid to ±240 R_s in x, y, and z axes, PARAM.in directed a two-way coupling between SC and IH (on the overlapping grid cells of the SC outer boundary and IH inner boundary) every 100 iterations. SC was directed to execute only at these coupling iterations, while IH was directed to run 200 iterations in steady-state. The SAVEPLOT section of this PARAM.in file was identical to that of the prior SC integration, creating x=0, y=0, and z=0 *.idl files on 32 processors from IH that pIDL combined to *n000200.out files in an analogous manner. These were also brought back to my Linux workstation for plotting.

4.3 Example Graphics from Computational Grid Output

Beginning with the ASCII files of the *niteration*=200 steady state solutions from SC and IH on their respective grid axes (e.g., x=0_mhd_1_n0000200.out for the y-z plane), the next step was to create graphical images from the data. Each file included the variables designated by the plotvar = 'MHD' designation, which were: x, y, rho, ux, uy, uz, bx, by, bz, Ew, p, jx, jy, jz. Here, the "x" and "y" values included are the left-to-right and bottom-to-top coordinates on the designated

computational plane (y-z, x-z, x-y). Additionally, rho is mass density (g cm^{-3}), ux, uy, uz are solar wind vector components (km s^{-1}), bx, by, bz are magnetic field components (G), Ew is the Alven wave energy density (erg cm^3), p is pressure (dyne cm^{-2}), and jx, jy, jz are current density (micro-Amperes m^{-2}). A single record on the data file includes the variable values for the x, y plane coordinate. However, the x, y coordinates are listed in the file in an arbitrary order. This is because the computational grid is the product of the "adaptive grid refinement" process in which the grid cells have different sizes depending on which "computational block" they reside. They consider this an unstructured grid.

SWMF included a file directory of IDL codes for creating plots from the output files in the SWMF code release that we used for the model experiments. Unfortunately, the directory was out of date and several of the routines required were not present. A University of Michigan Center for Space Environment Modeling (CSEM) staff person supplied us with a replacement directory of IDL codes. In addition, he provided us with an older version of a SWMF user manual (October 2011) that contained a section called "IDL Visualization." This section describes the function of two IDL "main programs" called getpict_main and plotfunc_main. The purpose of getpict_main is to read the designated input data file on the unstructured grid as described in the previous paragraph, and transform the data into a regular grid through spatial interpolation. However, the user must specify the x, y dimensions of the desired regular grid. This is difficult to do objectively because the unstructured grid contains a variety of grid spacings. For example, the unstructured grid for the SC data outputs had 4192 data records on each plane. To designate a square dimensions for the regular grid, we just took the nearest integer square root of the number of data records – in the case of SC, this resulted in designating a regular grid of dimensions 65 X 65. For the much coarser grid of IH, 2560 grid points were on each plane, and we used a regular grid of 51 X 51. In addition, the regular grid can be limited in range in the x, y dimensions in terms of distance in R$_s$. In the case of SC, we looked at the outermost x, y values of the unstructured grid and chose limits of ±23.0 R$_s$ for SC and ±230.0 R$_s$ for IH in both x and y directions. Then the getpict_main program was executed with a transformation = 'r' and two arrays were created: for example, for SC xreg dimensioned 65 X 65 X 2 (the latter dimension representing x and y), and wreg dimensioned by 65 X 65 X nw, where nw is the number of variables (=12 for 'MHD') as listed in the previous section. When looking at the wreg values for several of the variables, I noticed that for the scalar quantities (e.g., rho) the outer row and/or column of the array had negative, or unphysical, values. This was certainly due to extrapolation involved in the transformation to the regular grid. So I invoked a routine that removed the outer row and column from xreg and wreg in preparation for plotting.

(a) Contour Plots

First, contour plots of the scalar variables were created. The variables that we chose to contour were rho, solar wind speed |V| (magnitude of ux, uy, uz), magnetic field magnitude |B| (from bx, by, bz), p, and current density magnitude |j| (from jx, jy, jz). We created an IDL batch file called dn_plot_image.pro in which the user specifies the component (SC or IH), the input data filename (e.g., x=0_mhd_1_n0000200.out), and the choice of variable to contour. The code ran their "defaults" main program to initialize a number of parameters, then set the regular grid dimensions and range limits as mentioned above. It then ran getpict_main to produce xreg and wreg, and then removed their outer rows and columns. This resulted in xreg of dimensions of 63

X 63 X 2 and wreg of dimensions 63 X 63 X 12 for SC (49 X 49 for the first two dimensions in IH). The next step was to create graphics of the individual variables on the y-z, x-z, and x-y planes. In preparation for contouring, the code called a procedure that we wrote called "get_convalues" that set our choice of contour levels to plot, indicated which ones to label, and then multiply the variable values to be plotted to convert them to different units to bring them to a range more convenient to plot. For some of the plotted variables, this scaling was different for SC and IH. The code then called the IDL procedure 'contour' to create the graphic file – we used both postscript and jpeg image types (only the jpeg results are shown here).

With the choice of y-z, x-z, and x-y planes for five plotted scalar variables, a total of 15 graphics were created for both SC and IH. The following graphics figures represent a selection of them for illustration. We show the plots for a given variable and plane for both SC and IH for comparison of the spatial domains of each.

In Figure 1, mass density (rho) is displayed on the y-z plane. Again, the y-z plane cuts across the Sun left-right (east-west) and bottom-top (south-north) as viewed from Earth. In the figures, variation of density by latitude is somewhat apparent in the SC solution, and more evident in the IH graphic. This type of general radial decrease of density was also apparent in the x-z and x-y planes, with similar small variations with latitude and longitude respectively. Note the difference in the scale of the units shown in the respective plot titles

In Figure 2, we show the solar wind speed ($|V|$) on the x-z plane – that is, as viewed from 90° left around Earth's orbit of the Sun. Earth would be located at roughly x=215 R_s near the z=0
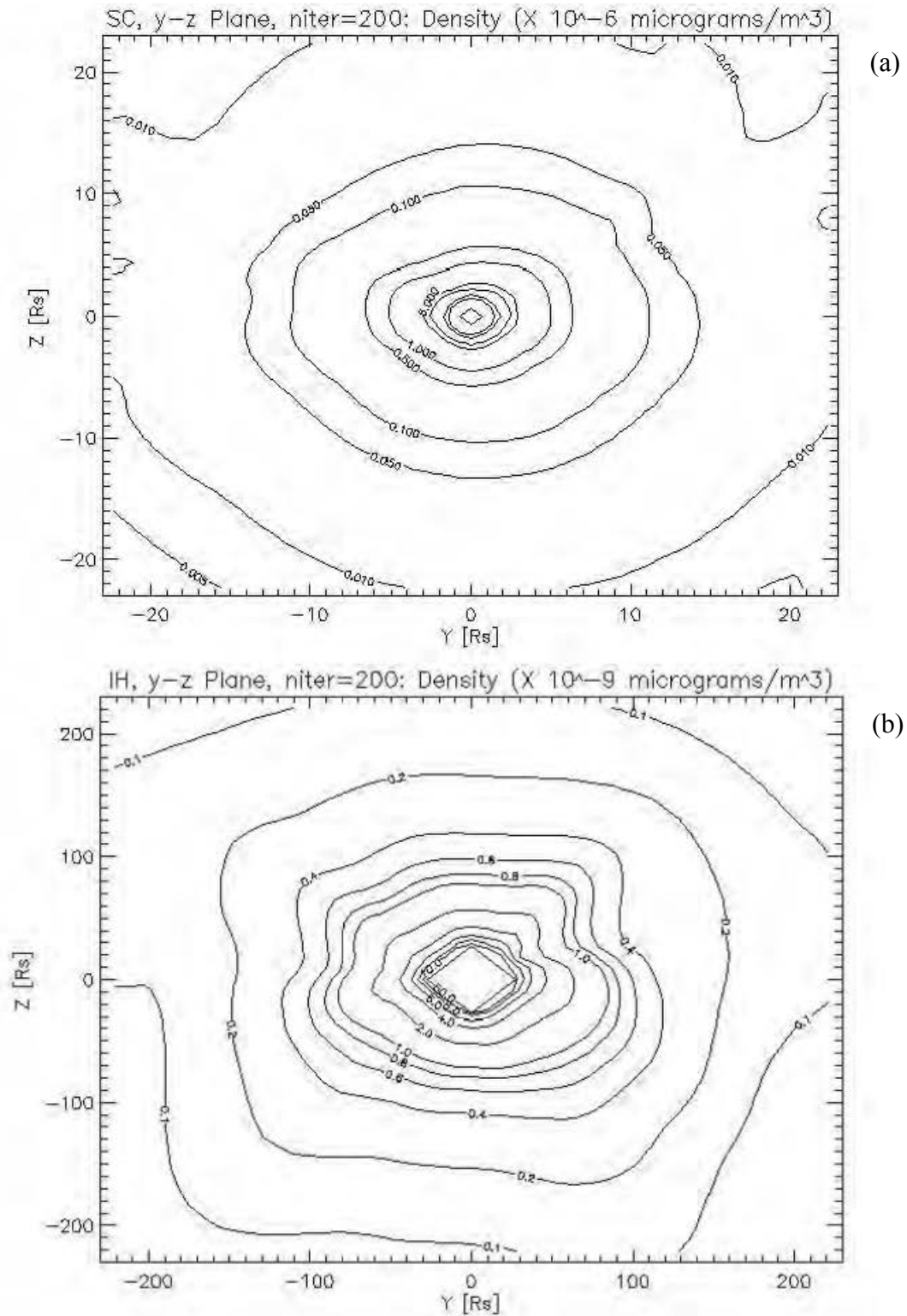
Figure 1. Mass Density (rho) on the y-z Plane for the *niteration*=200 Steady-State Solution for SC (a) and IH (b)

Figure 2. Solar Wind Speed (|V|) on the x-z Plane for the *niteration*=200 Steady-State Solution for SC (a) and IH (b)

line. The SC plot clearly shows that speed increases radially from the Sun, and that the increase is greater at higher latitudes and smaller near the solar equator. This is in keeping with the

expectation of more open magnetic field lines near the poles and more closed field lines at lower latitudes. The IH depiction shows even more pronounced variation of solar wind speed with latitude. At these greater distances from the Sun in the inner heliosphere, speed grows more rapidly with distance in the northeast and southwest, while the plasma motion is slower in the northwest and southeast sectors. This may also be effected by magnetic field line orientation – magnetic field streamlines will be shown below.

Magnetic field magnitude ($|B|$) for the x-z plane (for comparison with $|V|$ in Figure 2) is shown in Figure 3. $|B|$ on the x-y plane is depicted in Figure 4 to indicate its variation in low latitudes of the Sun. Note that this scalar magnitude rendering does not indicate field line orientation – we have to see the field lines shown as streamlines below. The magnetic field magnitude generally decreases with radial distance from the Sun. However, there are some significant differences in its spatial distribution between SC and IH. In comparing the results of the two components, we have to keep in mind that the entire domain of SC fits into the two innermost tick marks of the IH plot in both directions. So all we can say is that the magnetic field distribution shape is different between SC and IH. In both the x-z and x-y planes in Figures 3 and 4 respectively, alternating maxima and minima, the number of each pair we might call an "index", vary in size and quantity. In both planes IH shows more indices than SC. In Figure 3, the latitudinal variation apparent from the east side of the Sun, we see a magnetic field index = 2 in SC, while in IH an index = 5 is apparent. Figure 4, depicting the longitudinal variation near the ecliptic plane looking southward from above the northern pole, shows indices of 4 and 5 respectively for SC and IH. In the two IH plots Figures 3(b) and 4(b), there is a sign that $|B|$ has a local minimum (closed contours) near about 30 R_s in some of the maxima lobes around the Sun. Finally comparing x-z planes of $|V|$ and $|B|$ for SC in Figures 2(a) and 3(a) respectively, we see that speed increases faster as magnetic field strength decreases slower with distance northward and southward. Any type of correlation is not as clear in the higher index variations of $|B|$ in IH as seen in Figures 2(b) and 3(b).

Figure 5 displays the distribution of pressure (p) in the y-z plane for the SC and IH steady-state solutions. The pressure falls off radially with distance from the Sun at about the same rate in all latitudes. We saw generally this same tendency in the x-z and x-y planes as well. There seems to be no particular minima or maxima around the Sun as we saw with $|V|$ and $|B|$, and even to a lesser degree with density. Note the difference in the scale of the units shown in the respective plot titles.

Magnitude of the current density $|j|$ is shown in the x-z plane for SC and IH in Figure 6. Current density is proportional to the curl of the magnetic field vector. Therefore, the differences between current density and magnetic field should be more evident in the streamlines to be shown next. In Figure 6(a), we see an index = 8 around the Sun in the latitudinal variation, in contrast to the much simpler index = 2 for the x-z plane in $|B|$ as seen in Figure 3(a). In the form of the magnetohydrodynamic equations used in SWMF, magnetic field vector is the prognostic variable in the so-called induction equation. The current density is a diagnostic variable derived from the magnetic field vector solution. Because current density involves spatial gradients of the magnetic field, even a rendering of its magnitude introduces additional complexity to its spatial variation as compared to $|B|$. We see that the full variability of $|j|$ extends to the entire domain
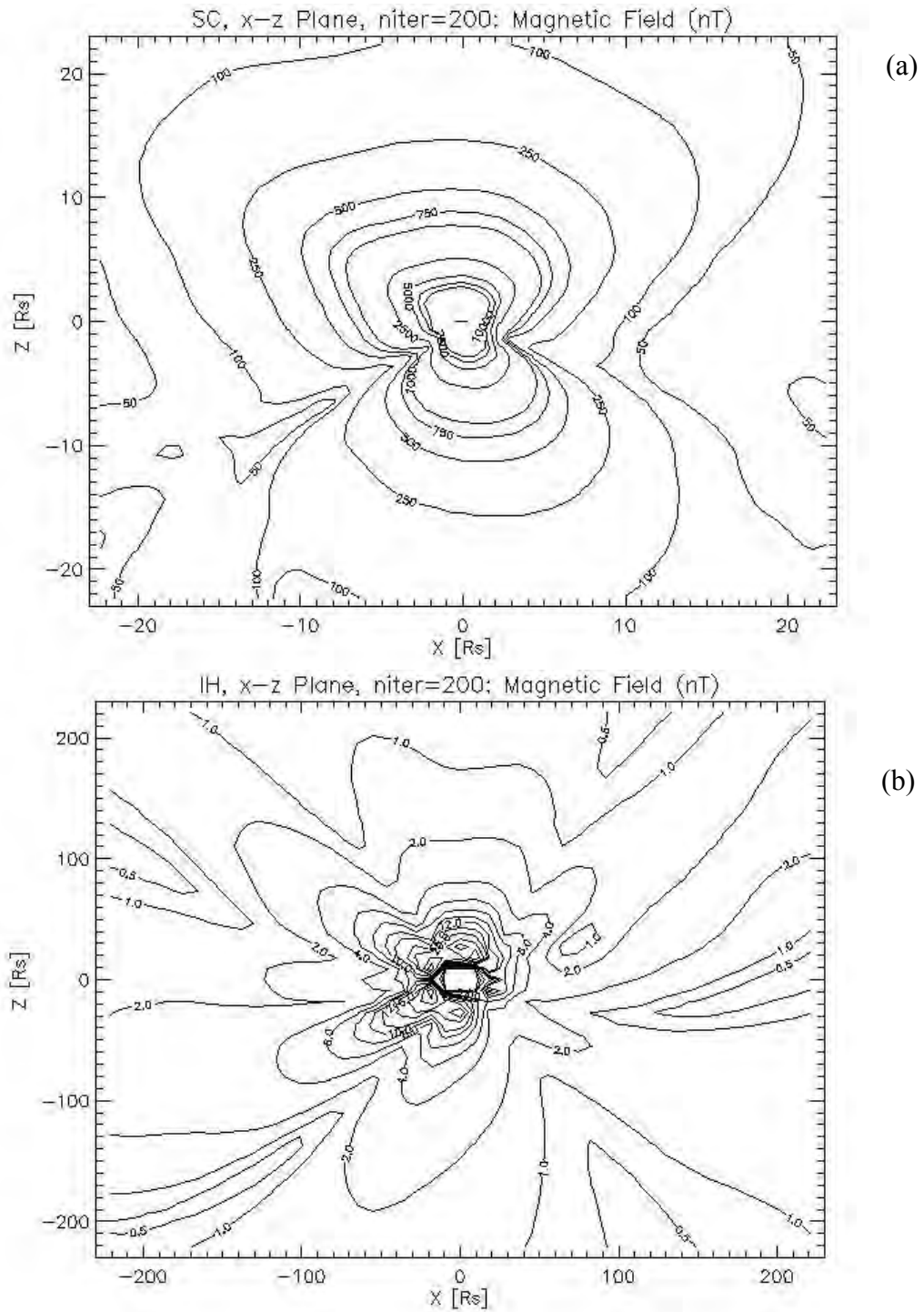
Figure 3. Magnetic Field Magnitude (|B|) on the x-z Plane for the *niteration*=200 Steady-State Solution for SC (a) and IH (b)

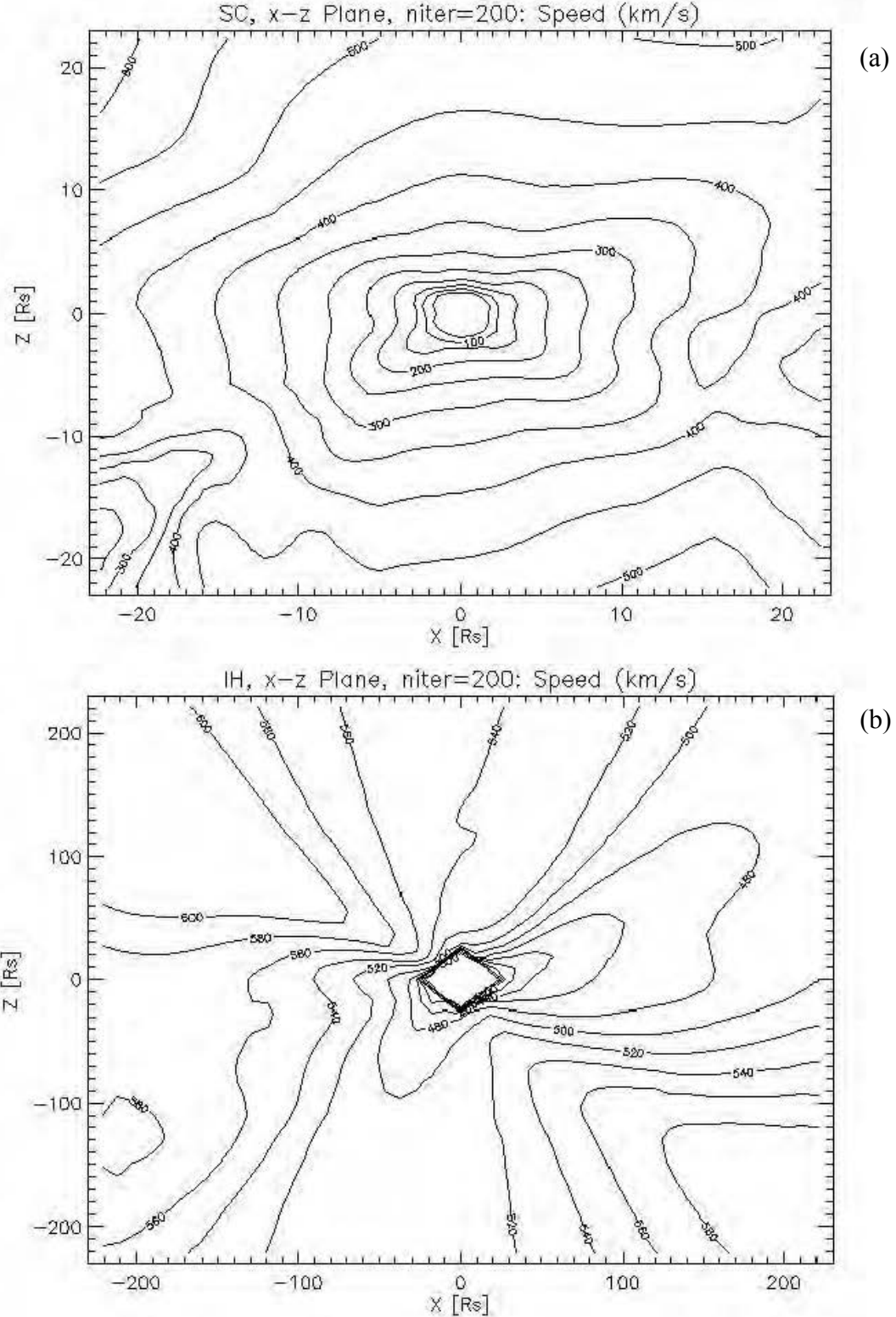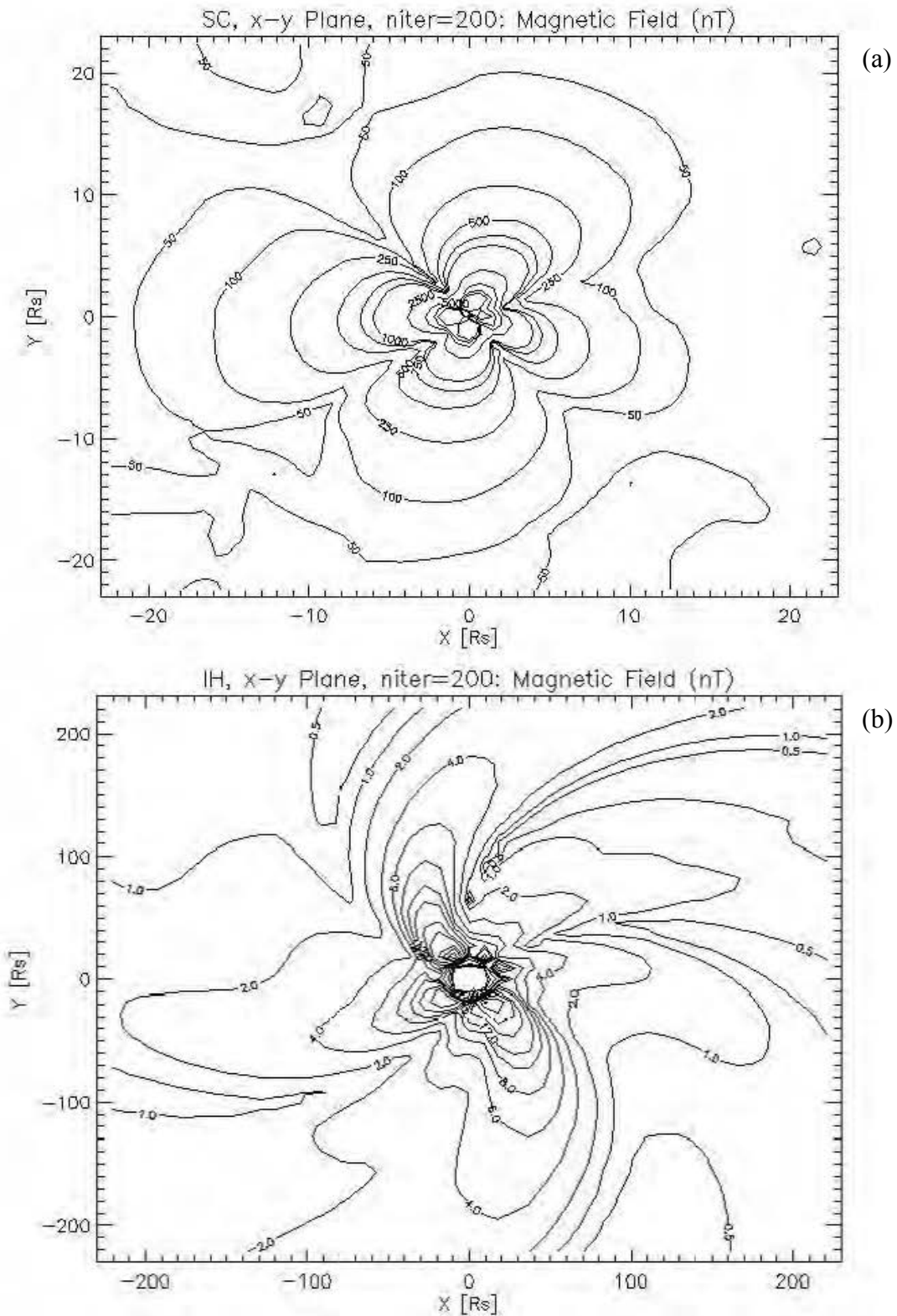**Figure 4. Magnetic Field Magnitude (|B|) on the x-y Plane for the *niteration*=200 Steady-State Solution for SC (a) and IH (b)**
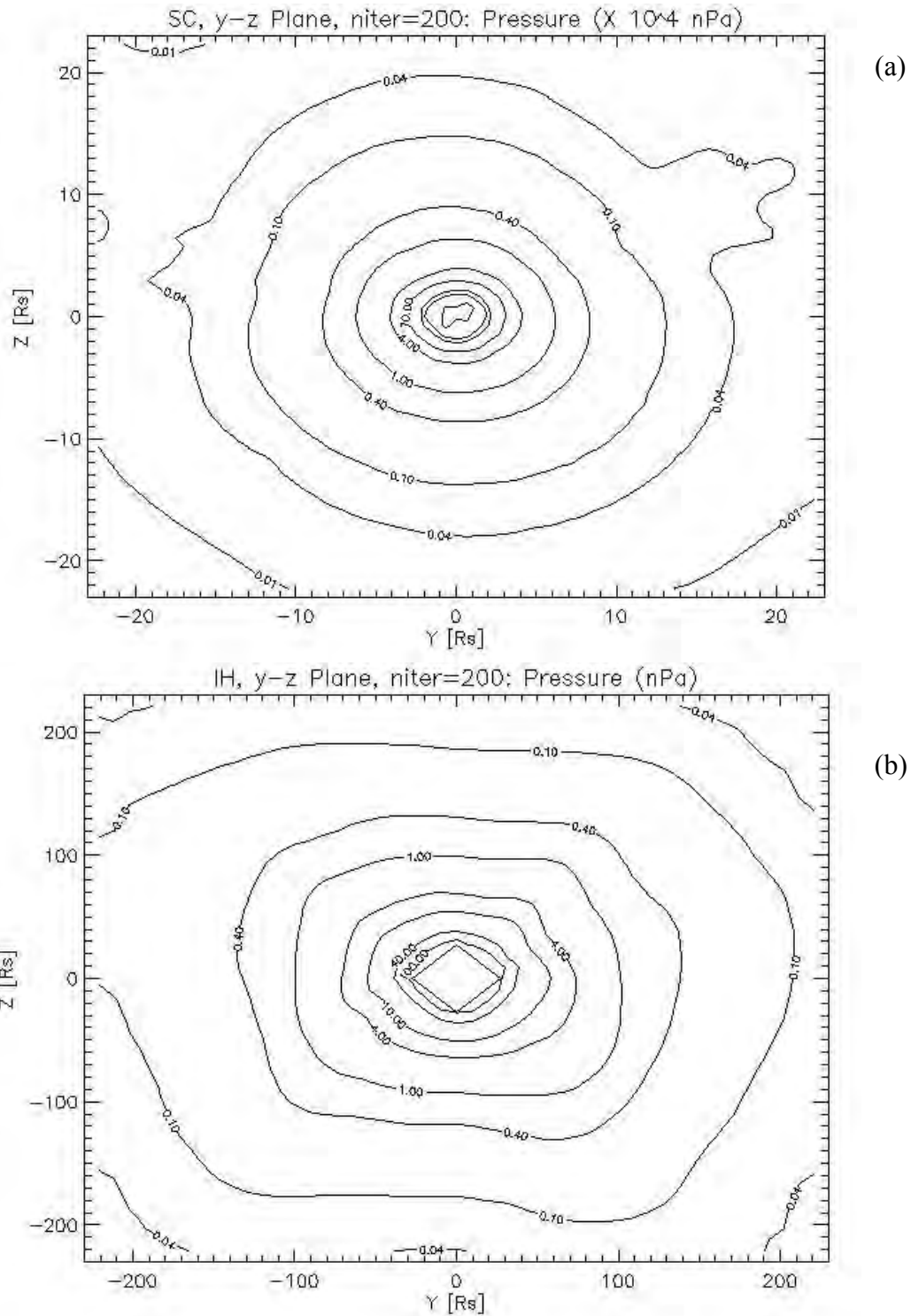
Figure 5. Pressure (p) on the y-z Plane for the *niteration*=200 Steady-State Solution for SC (a) and IH (b)

**Figure 6. Magnitude of Current Density |j| on the x-z Plane for the *niteration*=200
Steady-State Solution for SC (a) and IH (b)**

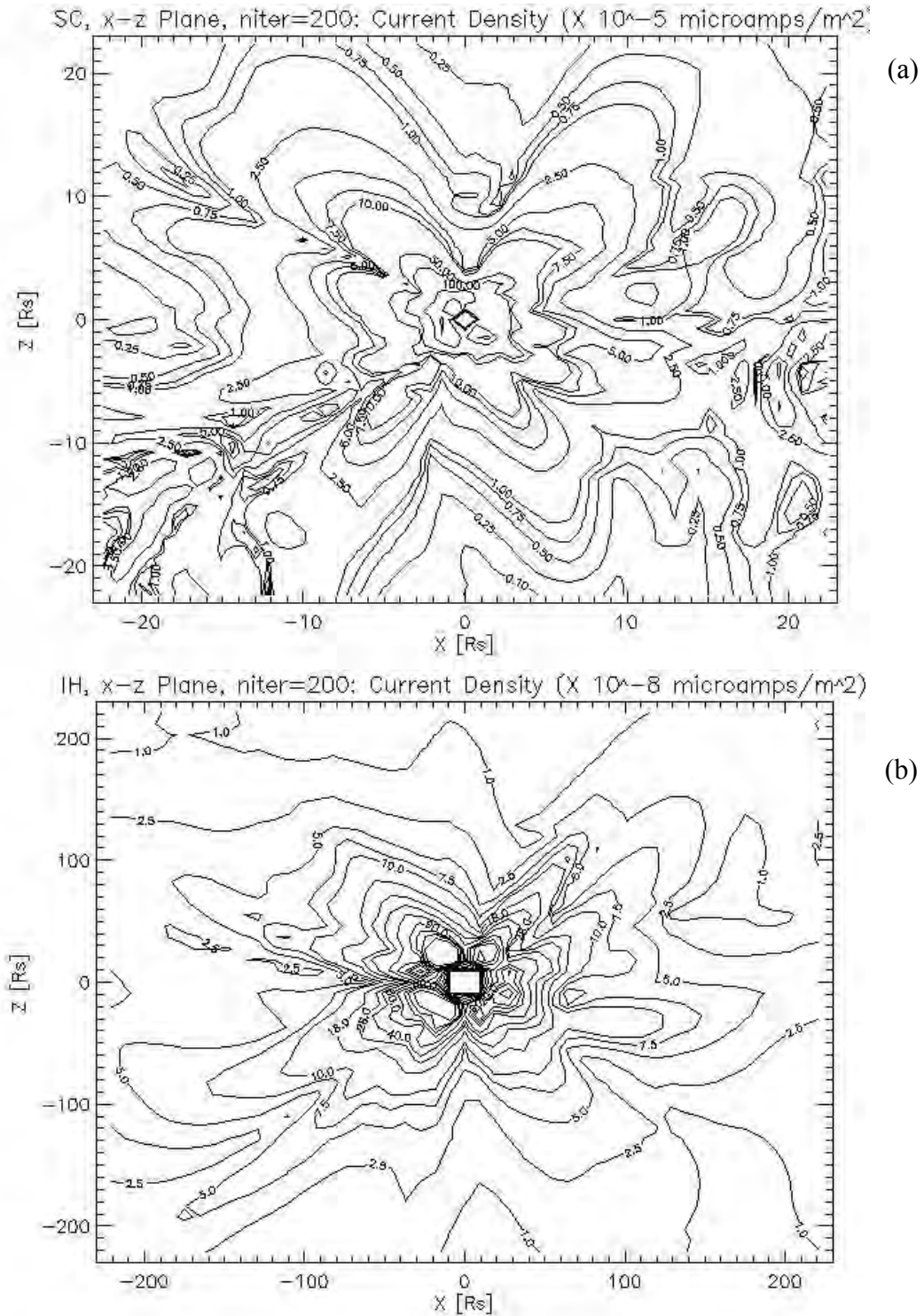of SC in Figure 6(a), with local minima and maxima occurring throughout. This reflects the
complexity of the magnetic field from which the current density is derived. Though the index of

the variability of the IH distribution of |j| is not as clear (approximately 7 or 8), it depicts local minima within about 30 R_s of the Sun as we saw in the |B| distribution of Figures 3(b) and 4(b).

(b) Two-dimensional Streamlines

Next, we used the IDL main program called "plotfunc_main" included in the SWMF code to produce graphics of two-dimensional streamlines on the respective three planes. For example, the uy and uz components of vector solar wind velocity can be streamlined on the y-z plane. In this case, we used a batch file that we called dn_plot_SWMF.pro to specify component (SC or IH) and filename (according to the plane to be plotted) and as we did in dn_plot_image.pro. It then also called the SWMF main program getpict_main to produce transformed regular grid arrays xreg and wreg as with the contour plotting. As mentioned above, the variable array wreg contains all of the variables to be considered for plotting: rho, ux, uy, uz, bx, by, bz, Ew, p, jx, jy, jz. In this case, we did not remove the outside row and column from the transformed grids because we were using the SWMF plotting routine. However, we stayed with the same x, y limits for the plotting that we had used for the contours.

To create the two-dimensional streamlines depicted in the following figures, we specified the pair of vector components from the variables available that were consistent with the plane to be shown. In addition, a "plotmode" setting was required, which is the type of scalar or vector plotting to be used. For the following plots, we used plotmode = stream to produce streamlines that show the local direction of the two-dimensional vector field. There is no indication of local vector magnitude in the plots as shown – just their direction. Finally, we imposed a white background and black streamlines so that the plots would be of the same style as the contour graphics.

Figure 7 shows the streamlines of vector solar wind velocity on the x-z plane from the ux and uz variables. The nearly directly radial orientation is apparent in all of the streamlines for both SC and IH – only a slight deviation is evident in the southern hemisphere of the SC domain near its outer boundary. These same patterns were present in the velocity streamlines on the y-z and x-y planes as well. This indicates that the steady-state configuration produced by both SC and IH depicts an outward expansion of the solar plasma in all directions. This is consistent with the understanding that, at a given point in the inner heliosphere, the incoming solar wind speed can be essentially represented by the radial component of plasma velocity from the Sun.

Streamlines of magnetic field vector on the x-z plane from the bx and bz variables are depicted in Figure 8. In the SC domain in Figure 8(a), we see the outward directed streamlines, indicating a positive polarity, in the northern hemisphere and inward, or negative polarity, streamlines in the southern hemisphere. A large closed loop occurs at low latitudes on the earthward side, and a smaller one on the opposite side. Splits or divergence in the streamlines are apparent near the outer boundary, indicating that at larger distances from the Sun the clear outward and inward orientation appears to lose its dominance. Figure 8(b) displays a very complex pattern of magnetic field streamlines. There are northward and southward directed streamlines in both the northern and southern halves of the plot. We know that the magnetic field is constantly changing in the inner heliosphere, and one instantaneous representation from a

model on a single plane cannot fully describe the full three-dimensional distribution of the magnetic field.

Given the complexity of the magnetic field streamlines, the current density streamlines should also show significant spatial variation. Figure 9 shows the y-z plane current density streamlines. The mixture of convergent and divergent current flows in Figure 9(a) demonstrates how much the SC magnetic field varies among the perpendicular x-z planes as they cross the y axes from -23 R_s to +23 R_s. In Figure 9(b) there seems to be a similar pattern in the streamlines in the southern and northern halves: incoming current flow within about y = ±100 R_s with eastward and westward current flow in the y < -100 R_s and y > +100 R_s sections of the plot. As with the magnetic field streamlines examples in Figure 8, a single slice through the computational grid in any of the orientations can only depict the local flow on that plane. But this type of graphic can at least give us some appreciation for the respective flow patterns for the solar wind, magnetic field, and electric current.

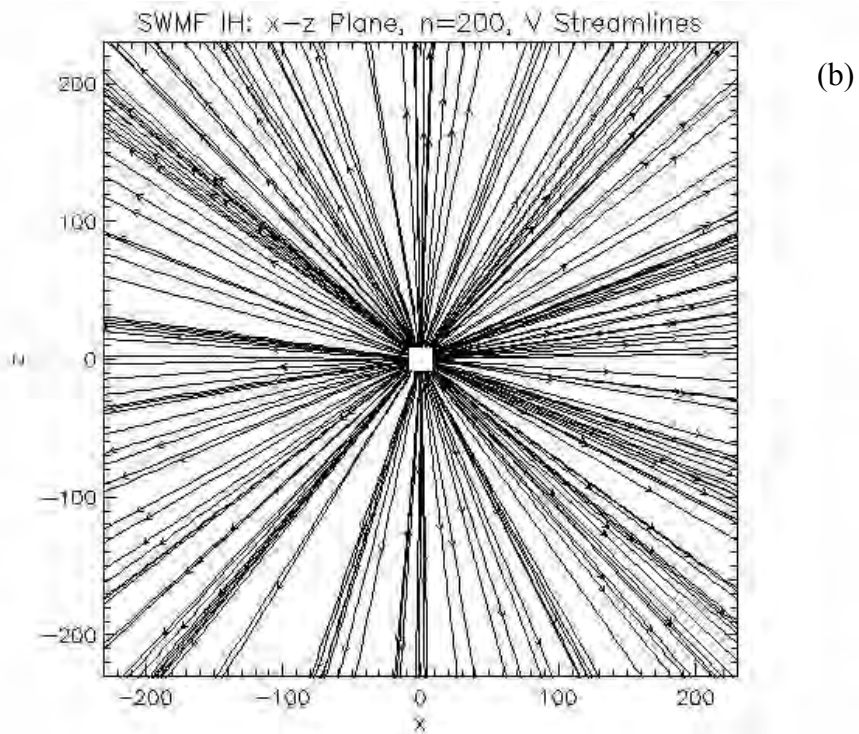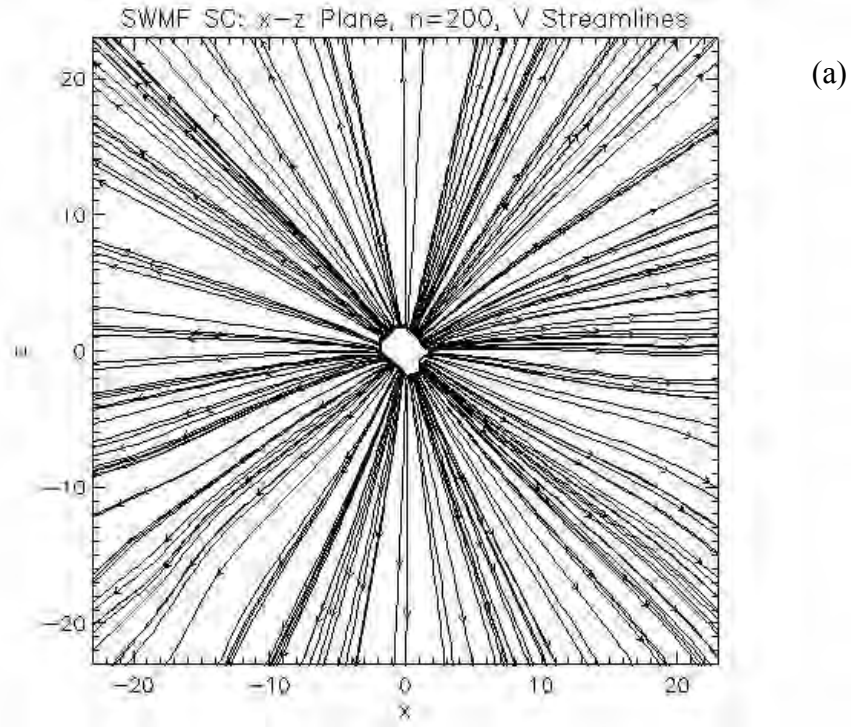**Figure 7. Streamlines of Solar Wind Velocity on the x-z Plane for the *niteration*=200 Steady-State Solution for SC (a) and IH (b)**
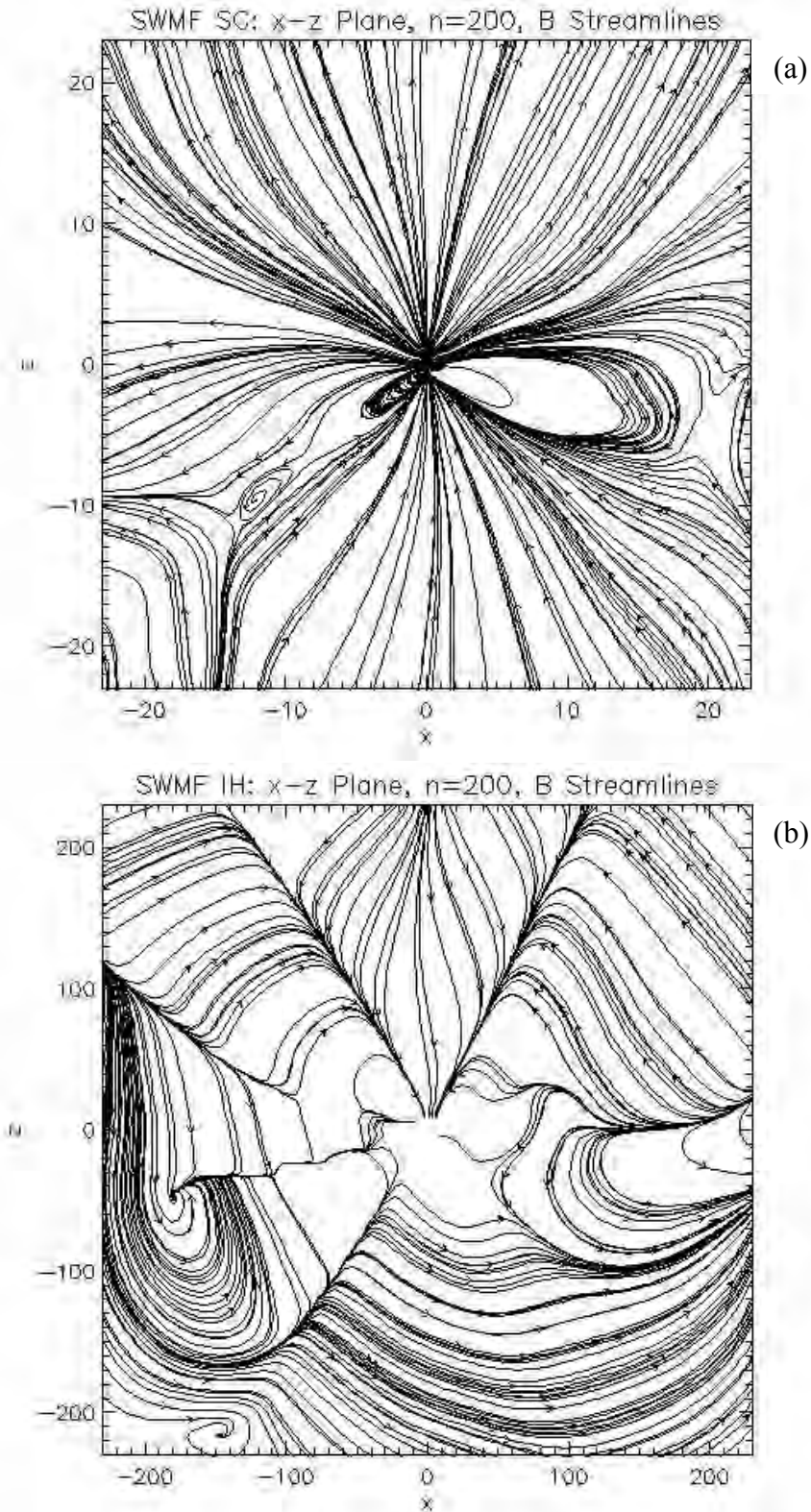
Figure 8. Streamlines of Magnetic Field on the x-z Plane for the *niteration*=200 Steady-State Solution for SC (a) and IH (b)
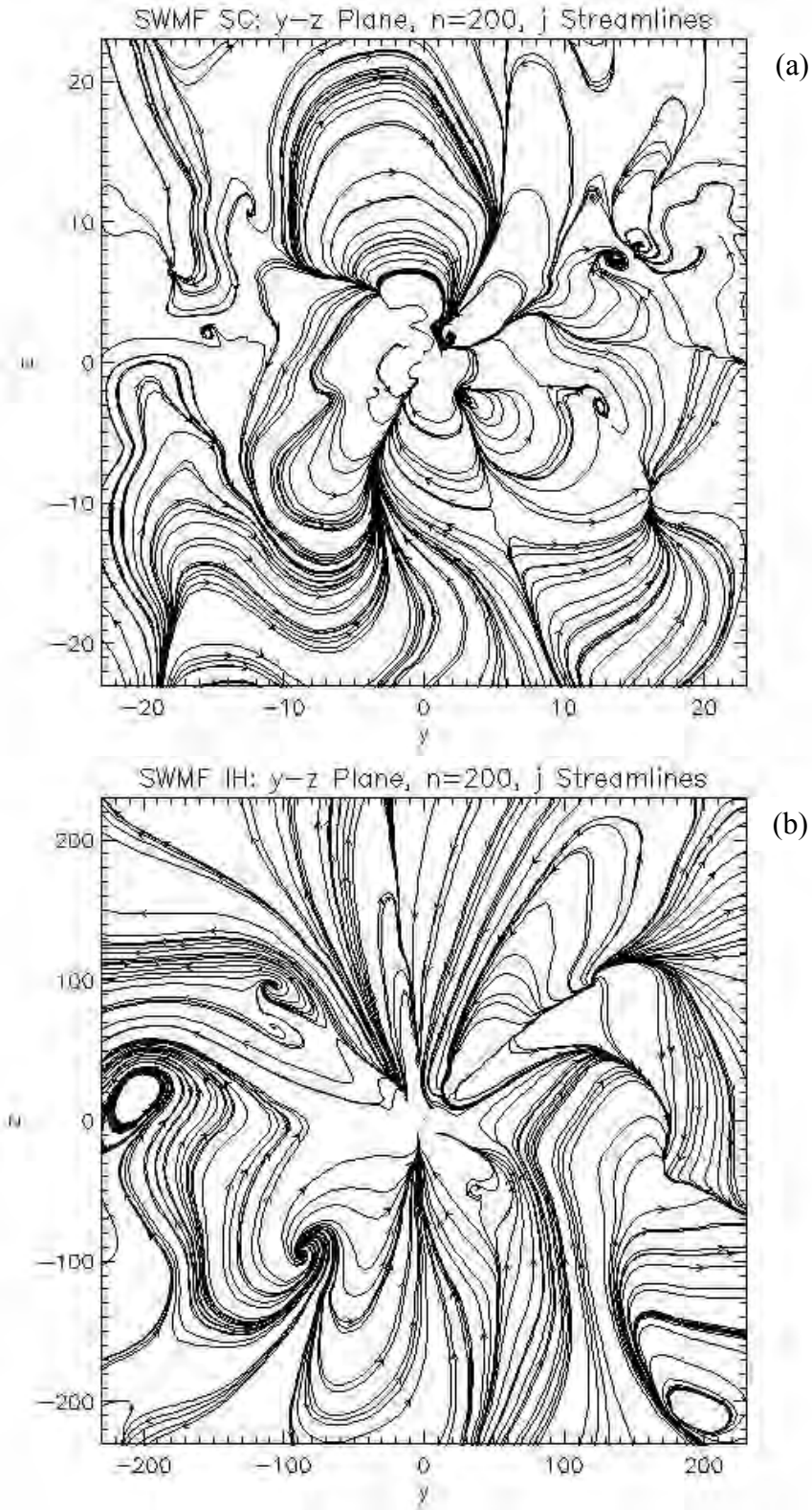
Figure 9. Streamlines of Current Density on the y-z Plane for the *niteration*=200 Steady-State Solution for SC (a) and IH (b)

4.4   Time Series of Steady-State Solution at Earth

A section of the PARAM.in file that directs execution of the SWMF IH model is called
"SATELLITE." This section is designed to create a time series of variable values from the model
solution at specific positions (x, y, z) in the computational domain as a function of date/time
defined by the trajectory of a "satellite" in the inner heliosphere. For each satellite specified, the
following parameters must be assigned: the set of variables to output (similar to the plotvar
parameter in SAVEPLOT – we used a set called MHD); the steady-state interval of *niteration* at
which variable values should be output (e.g., for every 100 iterations); the time interval in
seconds for which an output record is to be produced (I used 3600.0), and the filename of the
trajectory positions (I used IH/earth_traj.dat). The trajectory file was created by setting the
steady-state date/time for the experiment (1 May 1998 0 UTC in this case), the amount of time
before (here, -432000.0 seconds), after (432000.0 seconds) for ± 5 days, the time interval of the
positions to be provided (we used 1800.0 seconds), and then running an executable called
EARTH_TRAJ.exe. The trajectory position file is accessed during the execution of IH at each
specified steady-state interval to produce the set of variable values at the designated time
intervals from start time to end time (± 5 days). The data records in the output file using the set
MHD was: rho, ux, uy, uz, bx, by, bz, p, jx, jy, jz. Since IH is running in steady-state mode, its
solution at any value of *niteration* represents the experiment date/time. What changes from start
time to end time is the central merdian longitude of the rotating Sun, and the movement of the
Earth as it orbits the Sun. Those are the two factors that affect the IH steady-state solution
values at Earth.

We wrote an IDL procedure called "plot_satellite_traj.pro" that creates a line plot of the IH
niteration steady-state solution values of the output SATELLITE file in the Earth trajectory
positions. Plots of rho, |V|, |B|, p, and |j| for *niteration* = 200 were created as a function of time
for 0-5 days after the experiment date/time. For reference, we included corresponding values for
the first four of these variables derived from 1-hour interval observational data from the
Advanced Composition Explorer (ACE) positioned at the L1 Lagrangian point, about 1.5 M km
sunward from Earth. The SWMF User Manual states that the specified model output values are
extracted along the satellite trajectory. It is not clear from this if the values are interpolated to
the x, y, z position in the computational grid, or they are the grid volume through which the
satellite passes. Regardless, because the ACE measurements are in-situ data and the IH output at
the Earth trajectory is a product of grid volumes, it would not be possible to make a direct
comparison. However, we can see in the I-H x-y or x-z plane contour maps that include the
location of Earth (near x = 215 R_s, y ~ 0, z ~ 0), for example in Figure 2(b) for |V|, that solution
spatial gradients are relatively smooth. There should not be a significantly large difference in
model solution and measurement due to the spatial representativeness issue. That is, if we see
large differences, they would be the result primarily of model performance.

The following graphs display the IH model values and the ACE measurements as a function of
the Julian day of 1998, where the experiment date/time of 1 May 1998 corresponds to Julian day
121. In Figure 10, hourly values of IH steady-state solution for rho at the Earth trajectory and
hourly averages of ACE observations are shown as mass density. In the ACE data, proton
density is provided as number density in cm^{-3}. To make it compatible with mass density, we
multiplied the ACE proton density by a standard value for proton mass as 1.67262×10^{-18} μg and

converted from cm^{-3} to m^{-3}. The values shown in Figure 10 are in 10^{-9} µg m^{-3} as were shown in the mass density contour plot for IH in Figure 1(b). The gap in the ACE curve during Julian day 123 reflects missing 1-h average values for this period. We can see that the IH model density at the Earth trajectory location is considerably larger, at some times by an order of magnitude, than the ACE values converted to proton mass density. Though not shown here, the contour plot for IH mass density on the x-z plane show values of between 0.1 and 0.2 × 10^{-9} µg m^{-3} in the vicinity of Earth's position, which is consistent with values shown in Figure 10.

Figure 10. Hourly Mass Density for the *niteration* = 200 IH Steady-State Solution at Earth for Five Days After Experiment and the Observed Number Density from ACE

The IH steady-state solution of solar wind speed as the sum of the squares of ux, uy, and uz at the Earth trajectory is shown with ACE-observed solar wind speed from the x, y, and z components of proton velocity in Figure 11. Looking back at Figure 2(b), we see that the contoured values from the same solution are about 500 km s^{-1} in the vicinity of x = 215 R$_s$, z ~ 0. This agrees with the SWMF IH curve in Figure 11 that shows the speed slightly declining from just greater to slightly less than 500 km s^{-1} during the five days following the Earth through the solution. By contrast, ACE-observed solar wind speed during that period begins at less than 400 km s^{-1} but then experiences two major accelerations. The second steep increase to greater than

800 km s^{-1} could be an incoming solar wind event associated with a coronal mass ejection or a fast stream of a co-rotating interaction region.
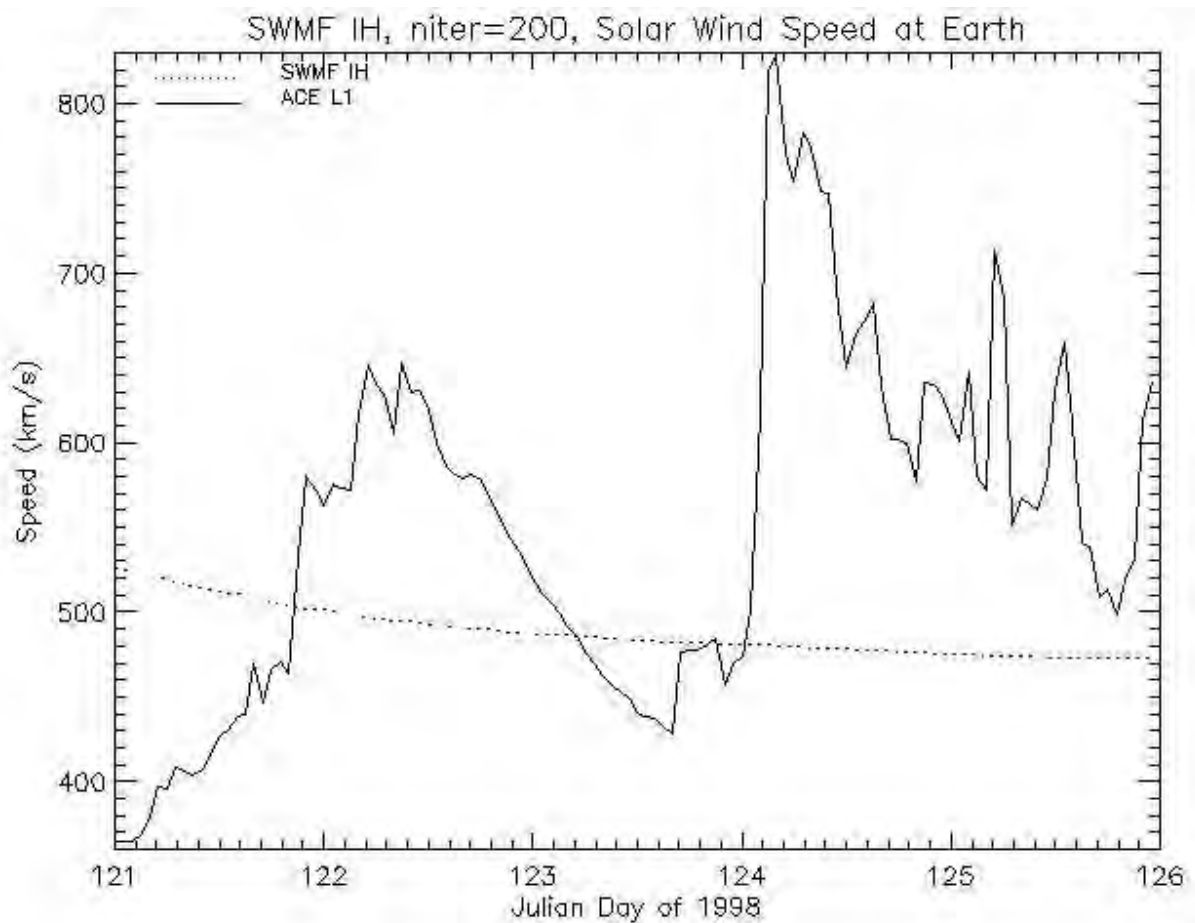
Figure 11. Hourly Solar Wind Speed for the *niteration* = 200 IH Steady-State Solution at Earth for Five Days After Experiment and the Observed Solar Wind Speed from ACE

Magnetic field magnitude steady-state IH solution from summed squares of bx, by, and bz at the Earth as it moves through the computational grid is shown in Figure 12 with comparison to the observed values from ACE at L1 derived from the x, y, and z components. We see that the model-produced magnetic field is much suppressed from the observed values. Its time series reveals none of the temporally irregular data from ACE. In fact, the magnetic field magnetism at ACE has a very similar pattern in sharp rises and slower falls as does the observed solar wind speed in Figure 11. The peaked increases near the beginning of Day 122 and 124 reinforce the earlier suggestion that these events may be associated with a transitory disturbance. By contrast, the IH solution contours of |B| in the x-z plane in Figure 3(b) shows a relative minimum in the region of Earth near x = 215 R$_s$ and the z = 0 plot axis for the solution at the experiment date/time. In Figure 12, the solution values stay small and only begin to rise on the third day. There does not appear any sign of a propagating disturbance in Figure 3(b) that may have arrived on Days 122 or 124. Perhaps without introducing a disturbance into SWMF SC and allowing it to propagate through IH, we see only the background fields as evident in the x-z plane.
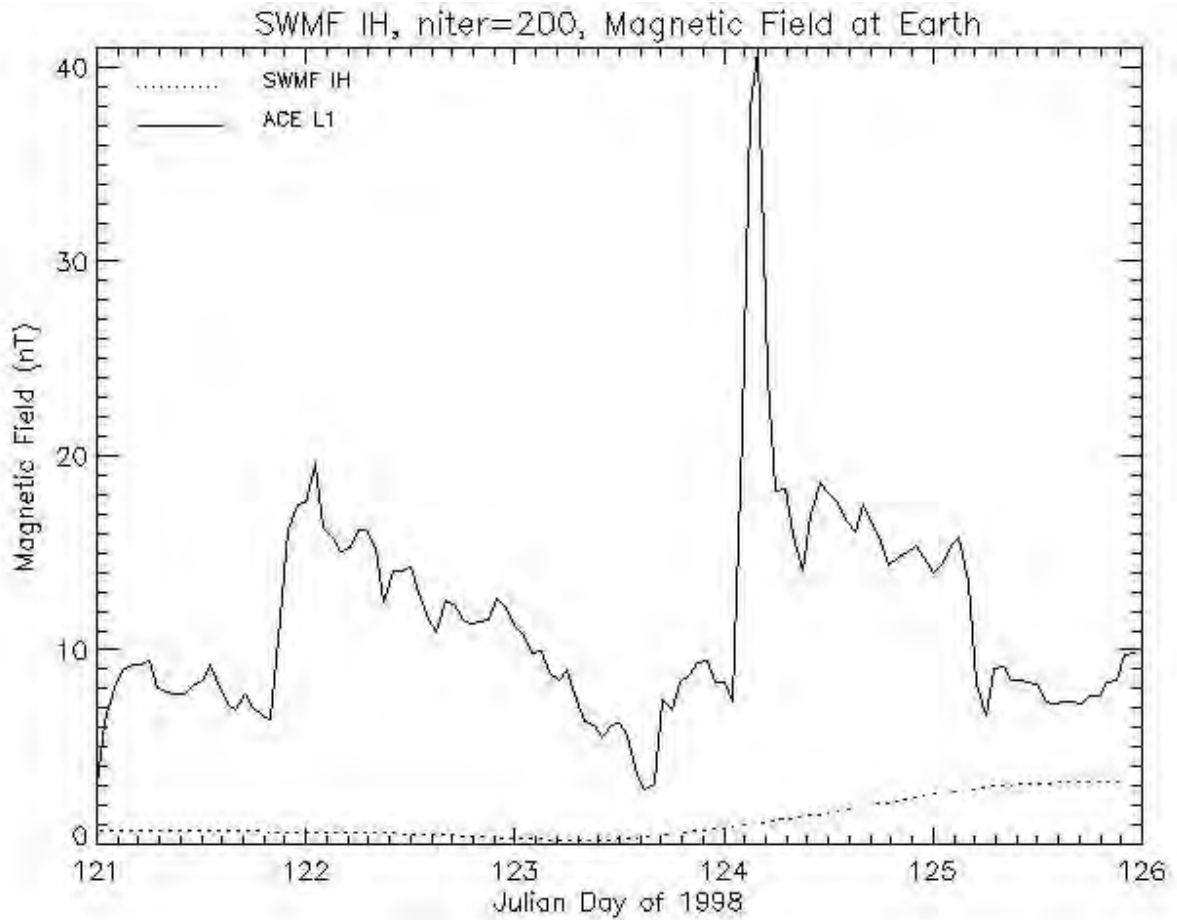
Figure 12. Hourly Magnetic Field Magnitude for the *niteration* = 200 IH Steady-State Solution at Earth for Five Days After Experiment and the Observed Magnetic Field from ACE

The next comparison we made was in the plasma pressure (p) between the model solution at Earth and a computed quantity derived from ACE number density and proton temperature. The latter estimate was made through the ideal gas law for particles, in the form $p = N_p K T_p$, where N_p is the observed proton density, K is the Boltzmann constant given by 1.38×10^{-23} J K^{-1}, and T_p is the reported proton temperature. Converting N_p units from cm^{-3} to m^{-3} and noting that the energy unit J = 1 Pa m^3, we express the product as nPa from the observed N_p, T_p, and the constant 1.38×10^{-8}. The hourly derived p from ACE observations are plotted along with the IH steady-state solution in Figure 13. Here, we can see a role of the larger model solution mass density shown in Figure 9 in shaping the model solution for p in Figure 13. We also see that ACE-observed number density and proton temperature combine to produce the same anomalous spikes in Day 122 and 124 that we saw in the solar wind speed and magnetic field line plots. Once again, we see a much smoother time series in the IH model output that does not reflect any of the transitory variation shown in the ACE data.
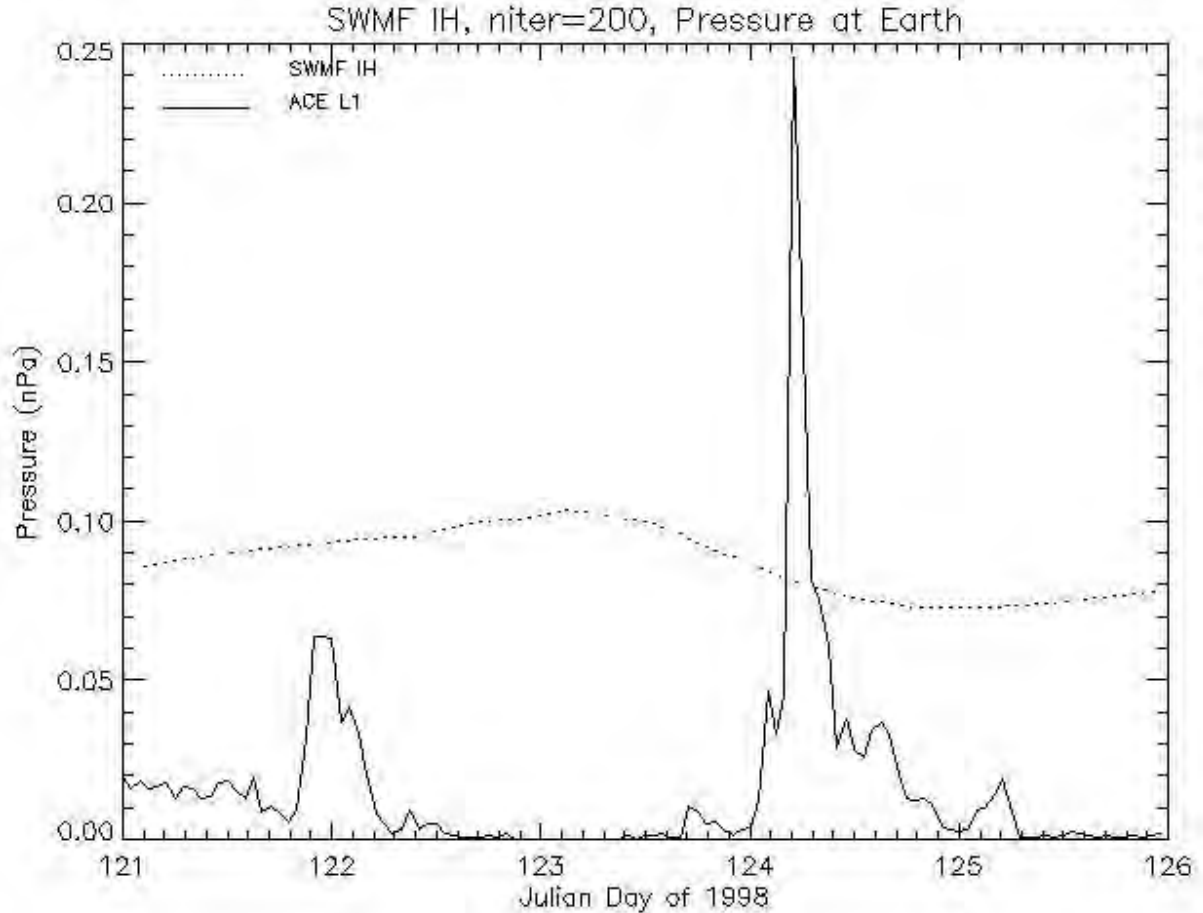
Figure 13. Hourly Pressure for the *niteration* = 200 IH Steady-State Solution at Earth for Five Days After Experiment and the Pressure Derived from ACE for the Same Period

Finally, for completeness the line plot of current density magnitude |j| is shown for the IH steady-state solution in Figure 14. In this case, the vector current density components were not included in the ACE data, so its magnitude is not shown. Because it is the curl of the magnetic field vector, we expect that its value near Earth will reflect the magnetism gradients in the region. The values at the experiment date/time begin at about 0.5×10^{-8} in the line plot, somewhat smaller compared to the x-z plane contours of Figure 6(b) of about 3.5×10^{-8} in the vicinity of Earth at $x = 215$ R_s and $z \sim 0$. Both model outputs were checked at the point and found correct – source of difference is uncertain. The line plot then increases and then decreases back to nearly the original level. Without a reference, it is not possible to assess performance.
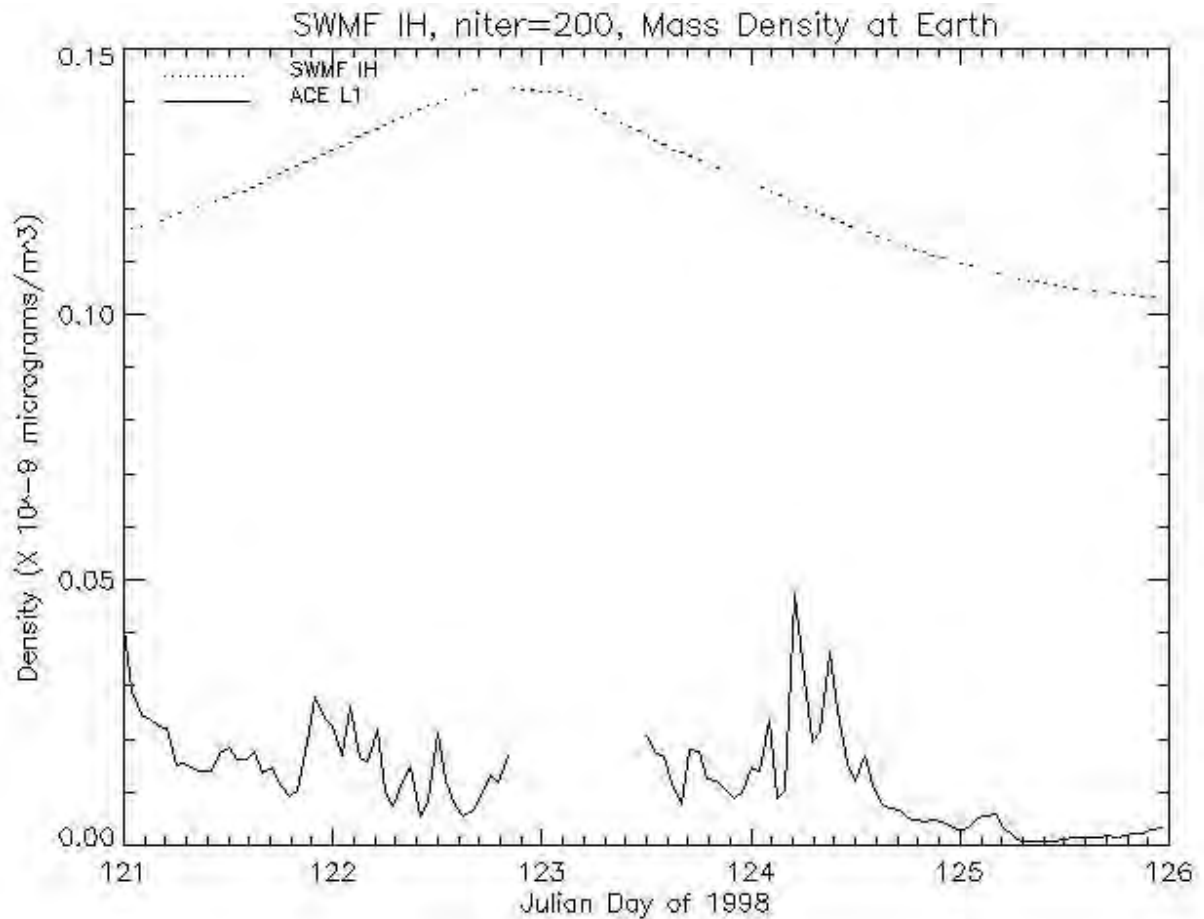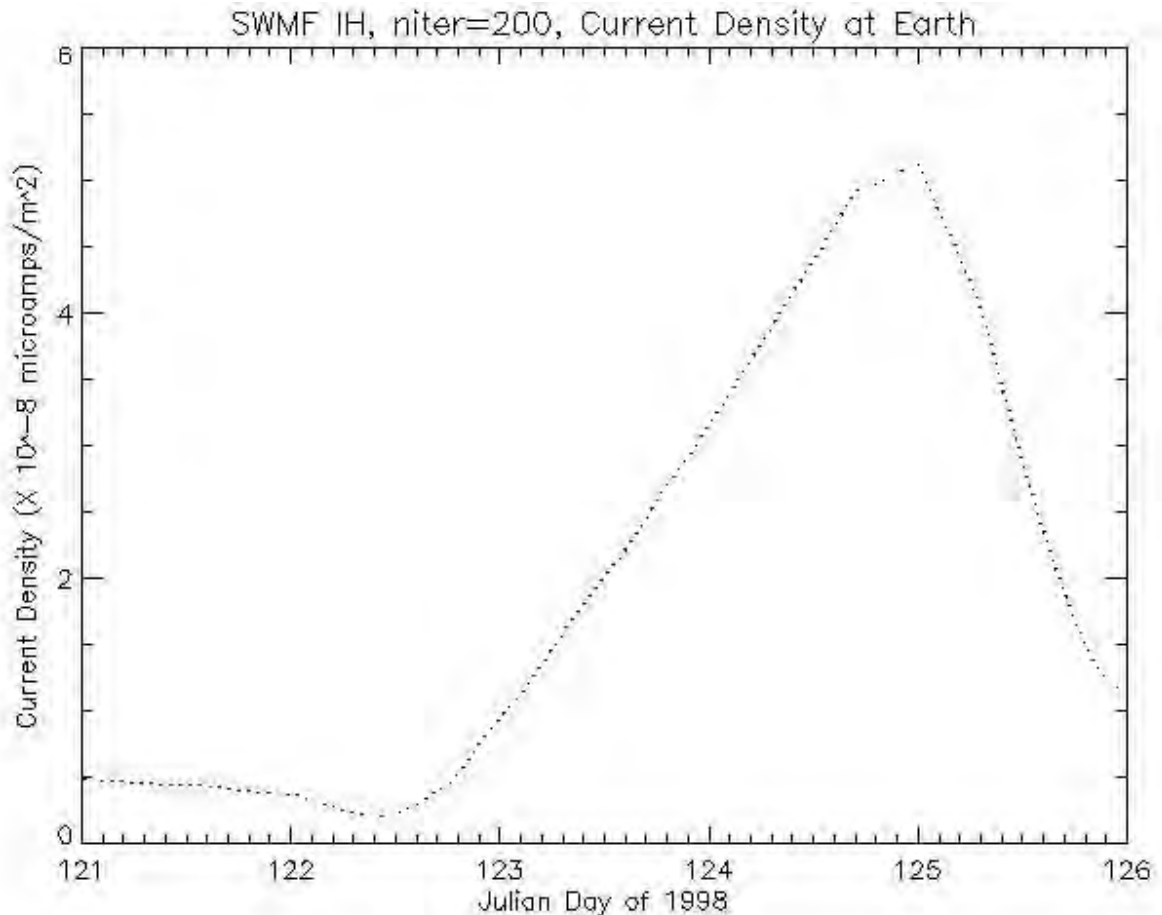
Figure 14. Hourly Current Density for the *niteration* = 200 IH Steady-State Solution at Earth for Five Days After Experiment

4.5 Summary and Value of Graphics

Samples of three types of graphical images that can be created from the SC and IH computational grid and near-Earth positions are discussed in this article. It is not intended to be a comprehensive discussion of the possible types of model output depictions that could be created. For example, y-z, x-z, and x-y plane two-dimensional grid files are just one type of output that can be derived from the SWMF SAVEPLOT capability. Given the files produced by the SC or IH components, the IDL visualization routines including "getpict_main" to retrieve variable set values on unstructured model grids and transform to a regular grid, and "plotfunc_main" to create a variety of two-dimensional plots like streamlines, vectors, and the like. We created simple labeled contour plots of the extracted scalar data planes to demonstrate "cuts" through the computational grid. Though quantitative reference data against to evaluate model performance on such planar cuts are not available, groups such as CSEM have used satellite images of similar spatial surfaces to see how well important features are simulated. In the same way, two-dimensional streamlines on those surfaces depict flow patterns that could be compared with imagery as it is available.

Line plots were also created, taken from the SATELLITE capability in IH to compute a position trajectory file that is used as input to the model. This might constitute satellite motion at a time sequence of positions through the computational grid, and extract the steady-state solution at those points. We were then able to create time series line plots of the output as a brief "tour" through the solution. By way of reference for model performance evaluation, we acquired the pertinent time period of ACE data taken at L1 (roughly 2 R_s) from Earth. We noted that this could not be considered a vigorous comparison due to model grid-volume values vs. in-situ observations. Nevertheless, the plots can show the degree to which the model solution represents important characteristics of the observed data. However, we must remember that it documents just a series of single points, so one must qualify the importance of the comparison in the context of the larger model solution. Generally, the temporal series of data is much smoother than the observations. Any space weather transients appearing at ACE would a priori be initiated by the model; otherwise we just see the model background data. Over enough simulations, it may be able to determine if important systematic errors are present in the results.

4.6 Effort to Reproduce SWMF Initial State Algorithm

As mentioned in Appendix B, section F, Understanding the Process for Setting Initial and Boundary Values in SC and IH, we attempted to reproduce the SWMF initial state algorithm from the Cohen, et al, 2007 article, given access to the SWMF model and to the code, but it was impossible to determine which sections of the code were relevant to the initial state algorithm.

5.0   CONCLUSIONS

Though a lot of background work has been accomplished in this project to better understand the Solar Corona and Inner Heliosphere models, much remains to be done to implement the principle techniques they employ to successfully initialize an independent model. Future research efforts would be to identify the most compatible initial state algorithm for the solar dynamo model, implement that, and evaluate the model output against the reference model output (for example, the SWMF and Cohen reference).

We foresee future endeavors to complete the work with the SWMF SC and IH begun to date. This includes completing an understanding of how initial and boundary values are introduced into SC and IH to initialize their executions. We plan to design and develop an algorithm that creates the initial and boundary values required to initiate the execution of a solar corona model. This algorithm will likely include standard methods for computing the vector magnetic field spherical harmonics in the corona from a magnetogram using the PFSS model, and assigning the initial solar wind velocity and plasma density and temperature state. These processes will be based on procedures commonly used to prepare initial and boundary values for the SWMF SC component. This may involve some experiments with the SWMF SC to confirm that the processes are being implemented correctly. The algorithm code would then ingest a file of grid point components from a candidate solar corona model (like the envisioned solar dynamo SC component), and compute the initial and boundary values as needed to initiate its subsequent integration to steady-state. The final step will be to generate the preliminary initial and boundary values for one or more solar magnetogram data sources. They will be provided for trial in the prototype solar dynamo model solar corona component.

APPENDIX A

Literature Review: Magnetohydrodynamic Models of the Solar Corona and Inner Heliosphere

A. Introduction

Magnetohydrodynamics (MHD) is the theory that governs the motions of charged fluids, like plasma, and the structure of their attendant magnetic field. The subject of this report is MHD as applied to the realm of the solar wind, the plasma emanating from the Sun, and its attendant magnetic field by models of the solar corona and inner heliosphere. In this introduction, the general problem of simulating plasma and magnetic field properties by three-dimensional (3-D) MHD models is presented. Material for this overview was drawn largely from two recent review articles. Mackay and Yeates (2012) have provided a summary of what is known about the magnetic fields of the Sun's photosphere and corona, that latter of which was a source for this report. Ofman (2010) has presented an article focusing on solar wind heating and acceleration effects that was also helpful. The remainder of this section of the report is intended to simply introduce the basic principles of modeling the solar corona and inner heliosphere in order to provide a context for the discussion of specific models that follows.

The solar corona is the outermost layer of the Sun's "atmosphere", exterior to the solar "surface" (photosphere) and innermost layer (chromosphere). It is made up of a heterogeneous distribution of plasma at very low density and very high temperature, and an ever varying and complex magnetic field extending out from the photosphere. The Sun's magnetic field may only be remotely sensed using current technologies at the photosphere – plasma densities are too low in the corona and beyond. Therefore, it is necessary to extend the magnetic field up from observations in the photosphere into the corona by means of physical models in order to estimate its structure beyond the solar surface. For the purposes of the current project, we will be concerned only with the large-scale global coronal magnetic field. Furthermore, this report will deal primarily with steady-state coronal models – that is, the configuration of the magnetic field in the corona associated with observations of the photospheric magnetic field at a single time. In this case, the coronal model is considered diagnostic rather than prognostic, in that it specifies a particular state of the magnetic field rather than simulating its time evolution. The latter would require a simultaneous time-dependent simulation of the photosphere's magnetic field by means of a magnetic flux transport model.

Four categories of coronal models are briefly described in the following paragraphs. They are potential field source surface models, force-free field models, magnetohydrostatic models, and full MHD models. The first three only explicitly diagnose the magnetic field, while the latter also specifies other plasma properties.

The Potential Field Source Surface (PFSS) model (Schatten et al., 1969; Altschuler and Newkirk, 1969) offers the most direct means of specifying the coronal magnetic field from the magnetic field distribution in the photosphere. The primary distinctive of this model is that it assumes the existence of no electric current in the corona. It computes the 3-D vector magnetic field $\mathbf{B}$ in spherical coordinates (r, θ, ϕ for radial, latitudinal, and longitudinal directions, respectively) from the photosphere to a "source surface" at a specified radial distance R_{ss} from the Sun's center. The inner boundary conditions are set by the photospheric measurements (the radial component B_r is derived from the line-of-sight observations, the latitudinal and

longitudinal components B_θ, $B_\phi = 0$) while the outer boundary conditions at R_{ss} are B_θ, $B_\phi = 0$. The source surface is set at or near two solar radii (R_s) to model the magnetic field in the lower corona and avoid the effect of the solar wind outflow that distorts the magnetic field from a current-free configuration at larger radii. PFSS solves Laplace's equation of the potential field, and the solution for the magnetic field components B_r, B_θ, B_ϕ are in spherical harmonics in which a finite number of harmonics are used to represent the field depending on the grid resolution of the photospheric B_r field. The single free parameter for the PFSS model is R_{ss} which is commonly set at 2.5 R_s but an optimal value can vary with solar magnetic activity.

The requirement that the magnetic field be strictly radial at the source surface imposes a severe limitation on the PFSS model. In reality, field lines bend equatorward within the domain of the model computation, intersecting the source surface non-perpendicularly. Schatten (1971) relaxed the current-free assumption by imposing an intermediate boundary $R_{cp} < R_{ss}$, and allowed electric currents to exist outside this boundary. However, the currents were limited to weak field regions between $B_r > 0$ and $B_r < 0$. They are referred to as current sheets and represent the non-potential regions of $r > R_{cp}$. The Schatten Current Sheet (SCS) model is commonly applied to the output of the PFFS model with the intermediate boundary $R_{cp} < R_{ss}$ having the computed **B** assuming no currents. The **B** on the R_{cp} surface is reoriented so that $B_r > 0$ at all points, and **B** is computed from the potential field solution in the region $r > R_{cp}$ subject to the reoriented **B** on the R_{cp} surface. Then restoring the original orientation creates currents where $B_r = 0$ in the $r > R_{cp}$ region. This results in a more realistic coronal magnetic field especially at larger radii. The Wang-Sheeley-Arge (WSA) model (Arge et al., 2004), which uses the PFSS and SCS models in tandem, has been widely employed to specify the magnetic field to user-selected multiples of R_s to act as an inner boundary for solar wind models (e.g., Owens et al., 2008).

Force-free models are a method of computing the coronal magnetic field while allowing for existence of electric currents and the attendant free magnetic energy. The essential assumption is that in the low corona, the magnetic pressure is much greater than the fluid pressure or the kinetic energy density of the plasma. Neglecting these latter two effects leads to a magnetic field with a zero Lorentz force, which is called a force-free field. In this case the current density is a product of **B** and a scalar function of radial distance that is constant along magnetic field lines and that describes their geometric shape. Assuming this function is constant everywhere leads to a linear vector Helmholtz equation in **B** that is straightforward to solve, the so-called linear force-free field problem. In practice, this assumption only holds for small regions, so it is not suitable for a global solution. In non-linear force-free fields, the scalar function is dependent on position in the corona. Three approaches to the problem of extrapolating non-linear force-free fields from photospheric measurements on a global scale have been tried, but their results are considered tentative: optimization method (Wiegelmann, 2007), force-free electrodynamics method (Contopoulos et al., 2011), and flux transport and magneto-frictional method (Mackay and van Ballegooijen, 2006; Yeates et al., 2007).

Magnetohydrostatic models represent the third category of coronal models that uniquely specifies the magnetic field. This type of model is based on a relationship equating the Lorentz force (the curl of the current density and the magnetic field) with the sum of the 3-D pressure gradient and density times the gradient of the gravitational potential. It is solved analytically given a specification of current density as a function of magnetic field that involves a field-aligned component and a component normal to gravity. The current density specification constrains the form of the pressure and density distribution in order to achieve an analytic

solution. They are not specified independently to satisfy any equation of state or energy equation – instead, they only facilitate the extrapolation of the magnetic field. A challenge of this method is the choice of two free parameters: one affecting the expansion or contraction of the magnetic field, and the other affecting its internal shape. Getting these parameters too large or too small leads to unrealistic solutions – they must be varied to best fit observations. Another limitation of this method is that the resultant magnetic energy is unbounded, meaning that it is unsuited for practical applications. Bogdan and Low (1986) and Zhao and Hoeksema (1994) have used the method to extrapolate the magnetic field to large radii assuming a shape parameter of zero in a manner analogous to the SCS approach. This has led to reasonably realistic shapes of the coronal structure and the observed interplanetary magnetic field (IMF).

Three-dimensional global MHD models offer the most comprehensive and physically complete means of specifying the magnetic field of the corona. Unlike the other three categories of coronal models described above, 3-D global MHD models must represent the processes of the plasma dynamics, thermodynamics and electromagnetics in a physically consistent manner. Because they include simulation of the plasma flow dynamics, there is no clear distinction between 3-D MHD models of the corona and the inner heliosphere. However, like the other categories, they currently depend on specification of the magnetic field in the photosphere for its extension into the corona. Additionally, 3-D MHD models require boundary conditions for the plasma properties (like density or temperature) that are not currently measured in the photosphere or the corona.

The 3-D MHD models of the global corona include time-dependent equations that are integrated to a steady-state solution (that may be non-unique) consistent with the imposed single time boundary conditions in the photosphere. The equations include the conservation of mass, conservation of momentum, electromagnetic induction, and the thermodynamic energy equation. The principal prognostic variables are the vector magnetic field, vector plasma velocity, plasma density, and plasma temperature. A polytropic expansion and compression of the plasma is assumed, where the polytropic index n of $pV^n = constant$ has a value of γ, the ratio of specific heats, when representing an ideal monatomic gas of $\gamma = 5/3$. The set of equations included in the models may vary in formulation depending on resistivity and viscosity that is assumed for the plasma. They are commonly closed by means of Maxwell's equations, Ohm's law for a plasma, first law of thermodynamics, and the ideal gas law. Groth et al. (2000), Riley et al. (2011), and Yang et al. (2012) presented examples of 3-D MHD model formulations suitable for corona magnetic field and plasma property specification.

The standard initialization process in 3-D MHD coronal models involves establishing a fixed lower boundary magnetic flux from observations, specifying an initial state potential magnetic field on the computational grid, and imposing an initial solar wind state assuming spherical symmetry. The model is then integrated ahead in time until a physically consistent steady state solution is reached. Because of a lack of in-situ observations in the corona, the veracity of their solutions has been evaluated through qualitative comparison with observed plasma emission intensity from satellite imagery as an indication of their relative plasma density distribution. Comparison studies conducted to date (e.g., Vásquez et al., 2008) have shown that the models tend to specify plasma density better at low latitudes than at high latitudes.

Using only the radial component of the observed magnetic field in the photosphere, Riley et al. (2006) compared the coronal magnetic field solutions from the PFSS and 3-D MHD models. They found good agreement between the solutions in general, with only small differences in magnetic field line structures around coronal holes (more open in the MHD

solution) and longer field lines and greater realism of the cusp structures in the MHD configuration. It was speculated that with the use of vector magnetograms from the photosphere, greater differences in the solutions would result. In spite of their similar manifestations of coronal properties, the 3-D MHD models are considered less constrained by simplifying assumptions and offer a greater potential for physically relevant solutions. In this review, we will limit our attention to just this class of coronal models.

The heliosphere is the cavity of space occupied by the magnetic field advected outward from the Sun by the solar wind. The inner heliopshere is usually construed as that portion of the heliosphere extending out through the several planets closest to the Sun – to Mars, for example. The magnetic field is weaker and the plasma more tenuous than in the corona, yet the solar wind and interplanetary magnetic field (IMF) have a profound effect in shaping the magnetic fields of those planets that possess one. The characteristics of the IMF also affect the levels of galactic cosmic rays that effect Earth. Additionally, the solar wind in the inner heliosphere can modify the propagation speed of coronal mass ejections (CME). Unlike the corona, in-situ measurements of solar wind and IMF properties have been made in the inner heliosphere. Most notably, in-situ sensors reside on satellites positioned at the L1 Langrangian point, and have made near-continuous observations for years. These measurements have been used to provide short-term warnings of incoming space hazards, but have also served as reference data against which models of the inner heliosphere have been evaluated.

Inner heliosphere models fall into two major classes. The simpler kinematic models simulate the trajectory of solar wind parcels from a rotating, steady state corona to the Earth along the Sun-Earth line. To varying degrees, they empirically account for stream-stream interactions as faster parcels catch up with slower parcels (compression) or fall behind faster ones (rarefaction). The more complex 3-D MHD models are of the same type as those executed for the corona. They generate a steady-state solution for the configuration of the IMF and plasma properties on three-dimensional grids extending earthward from the Sun. Most of these models also use the outer boundary of the steady-state corona model to supply their inner boundary values of the magnetic field and plasma properties. In the following paragraphs of this introduction, the basic properties of these two types of inner heliosphere models will be presented.

Kinematic solar wind models propagate the solar wind outward from Sun to Earth in a variety of ways. This requires a specification of the radial component of the magnetic field on the outer boundary of a corona model. The coronal model's outer boundary serves as the kinematic solar wind model's inner boundary. Most kinematic models use the coronal specification from the PFSS model coupled with the SCS model. They begin the process by constructing the field of radial solar wind speed on the outer boundary of the corona model from the radial magnetic field. This involves an empirical relationship between the radial velocity and two quantities computed from the radial magnetic field: a flux tube expansion factor and the distance to the nearest coronal hole boundary. This speed is used to move the solar wind "parcel" with its attendant IMF polarity (positive outward, negative inward) from the solar central meridian as it passes the ecliptic line (the point in the direct Earth path, called the subearth point) towards Earth. This movement is strictly one-dimensional. The types of interactions that affect the parcel's speed vary in complexity among the kinematic models. Some models (e.g., the WSA model, see Arge and Pizzo (2000)), for example, adjust the speed of faster moving parcels by taking into account the speed of slower parcels ahead of them at regular intervals between Sun and Earth. An averaging adjustment is made for IMF polarity. Another

kinematic model, the Hakamada-Akasofu-Fry (HAF) model (Fry et al., 2001) uses parameterized compression algorithms to account for the interaction between slow and fast solar wind streams. Speed is determined from the time rate of change of the position of plasma parcels. The HAF model predicts the magnetic field vector assuming magnetic flux conservation, and a scalar density from mass flux conservation.

All forecasts from one-dimensional kinematic models are represented by a time series of the predicted variables from day 0 to day N of the N-day forecast valid at the L1 Lagrangian point. This facilitates their comparison with the in-situ observations at that point in space. However, it must be remembered that the models simulate volume elements of the plasma and IMF while the in-situ observations are single point measurements. Also, the model grid cells have typical horizontal dimensions of 2-5° latitude and longitude, resulting in a passing of grid cells at 3-8 hour intervals as the Sun's central meridian rotates past the ecliptic line. The model cadence is much slower than the in-situ observational rate, requiring that the observations be temporally averaged for comparison with forecast outputs.

The 3-D MHD models of the inner heliosphere can be divided into two sub-classes. The first group comprises those that are the extension of a corona model through the inner heliosphere. In this case, the same model framework is used to solve the MHD equations to steady state as a spatial continuum. Examples of such models are the National institute of Information and Communication Technology (NiCT) model (Nakamizo et al., 2009) and the Solar-Interplanetary Adaptive Mesh Refinement Space-Time Conservation Element and Solution Element (SIP-AMR-CESE) model (Feng et al., 2010). The second group includes those that distinctly model the inner heliosphere, assuming some specification of inner boundary values at some radial distance from the Sun. A common understanding of the distinction between the domains of the corona and inner heliosphere are the regions where solar wind speeds are generally less (corona) or greater (inner heliosphere) than sound waves and Alfvén waves, which are waves propagating on magnetic field lines in a plasma. Inner boundary values for inner heliosphere models can be set empirically or derived directly from a separately executed steady-state coronal model. The latter may be any model coronal specification, using any of the four basic corona model types. Models such as Enlil model (Odstrcil, 2003) and Space Weather Modeling Framework – Inner Heliosphere model (Tóth et al., 2005) use 3-D MHD to distinctly model the inner heliosphere. In this review, we will consider both sub-classes of inner heliosphere models – those combined with modeling of the corona and those that stand alone in modeling the inner heliosphere.

B. List of Existing Models (found from a Google search in the indicated topics)

- Models of the Solar Corona
    - Magnetohydrodynamics Around a Sphere (MAS)
    - Space Weather Modeling Framework (SWMF) Solar Corona (SC)

- Models of the Inner Heliosphere
    - Enlil
    - Space Weather Modeling Framework (SWMF) Inner Heliosphere (IH)

- Combined Models of the Solar Corona and Inner Heliosphere
    - Hayashi

- Coupled MAS and Enlil (CORHEL)
- Coupled MAS and MAS-Heliosphere
- National institute of Information and Communication Technology (NiCT), Japan
- Solar-Interplanetary Adaptive Mesh Refinement Space-Time Conservation Element and Solution Element (SIP-AMR-CESE)
- Coupled SWMF SC and IH

C. Solar Corona Models

1. Magnetohydrodynamics Around a Sphere (MAS)

The MAS model of the solar corona (Mikić et al., 1999; Linker et al., 1999) of the late 1990s was a three-dimensional system of MHD equations that assumed adiabatic plasma compression and expansion. The adiabatic assumption, where no heat is exchanged between the local system and its surroundings, simplifies the thermodynamic energy equation by dictating that entropy remains constant. Accordingly, a polytropic index of $n = 1.05$, substantially less than the usual $\gamma=5/3$ (for an ideal monatomic gas), was used and justified by assuming that temperature changes in the corona are relatively small ($n = 1$ is isothermal). The model authors found that this simplifying assumption limited the model from producing solutions that matched well with plasma density distributions inferred from imagery. Furthermore, it prevented a realization of the temperature contrasts between coronal streamers (plasma trapped by closed magnetic field lines) and coronal holes (freely moving plasma in the presence of open field lines).

The model computational grid of this era was in spherical coordinates using a non-uniform mesh. The grid spacing was 0.013 R_s (about 90 km) near the chromosphere, becoming much coarser as it expanded out to 30 R_s. Latitudinally, the mesh was 1.6º near the equator and expanded gradually toward the poles. The uniform longitude grid spacing was 5.6º. Uniform electromagnetic resistivity and fluid viscosity was assumed, each set to allow for pre-specified resistive and viscous diffusion time, respectively.

Linker et al. (1999) specified the radial component of the magnetic field B_r in the photosphere from magnetograms based on ground-based optical telescope observations. The B_r grid fashioned from the observations was a composite of daily observations taken near the solar central meridian, representing a total time span of 29 days to ensure that the complete solar surface was recently sampled. Using this means of specifying the photospheric magnetic field ignores temporal evolution in the total measurement period – it means that there is as much as a 28-day disparity among the ages of the various portions of the grid. To specify density and pressure in the coronal base as required by the MHD formulation, a constant value of ion/electron number density was chosen and a constant temperature was assigned, and the ideal gas law was used to compute the associated pressure.

The next step was to initialize the computational grid. For the plasma prognostic variables density, pressure and velocity, a solar wind configuration of spherical symmetry was imposed that was consistent with the coronal base values. To initialize the vector magnetic field, a potential field source surface model is solved using the specified B_r in the photosphere and assuming $B_r = 0$ at the outer boundary. This latter boundary condition led to completely closed field lines in the initial state.

The model equations were then integrated forward in time until a steady-state solution was reached. It included regions of open field lines associated with coronal holes and closed field lines depicting coronal streamers. In reality, the solution reflects the temporal, spatial composite of the photospheric magnetic field used to impose the boundary values. In that sense, it cannot be considered a "snapshot" of the coronal state, but a blend of individual daily states over the 29 day time span. This may be reasonable for times of slowing changing conditions (near solar minimum), but would not realistically reflect the temporal evolution of the magnetic field and plasma in normal circumstances.

Mikić et al. (1999) compared the results of the coronal specification with eclipse images to evaluate the locations and sizes of the coronal streamers produced by the model. Using photospheric magnetic field data from solar rotations prior to three solar eclipses, predictions of the coronal configuration were made. The eclipses occurred near the solar minimum when coronal changes are slower, so the primary features of the coronal streamers were replicated by the model solution. Comparisons were also made with in-situ observations made by the Ulysses spacecraft, which was in polar orbit around the Sun. The latitudinal profile of the radial magnetic field and the position and shape of the heliospheric current sheet were better specified by their coronal model than by a potential field source surface solution.

A single state photospheric magnetic field restricts the coronal model that uses it to compute a steady state solution. As mentioned in the Introduction, coronal models are not time-dependent only because of this constraint. In theory, if a constantly evolving photosphere were specified to provide time-dependent boundary conditions to the coronal model, the corona configuration solved by the model would be allowed to evolve with time. Mikić et al. (1999) simulated coronal evolution in their model by relaxing the constraint that the tangential component (that is, the θ, ϕ components) of the electric field at the lower coronal boundary (the photosphere) be zero to maintain a fixed B_r there. A nonzero tangential electric field was imposed as a sum of a stream function (curl vector) and electric potential function (gradient vector) of θ and ϕ at $r = R_s$. However, since line-of-sight magnetograms contain no information on the tangential magnetic field component, the electric potential function could not be used. From Maxwell's equations, the Laplacian of the stream function is proportional to the time rate of change of B_r, so time interpolation between whole-sun magnetograms provided a smoothly temporally varying B_r field from which the stream function could be obtained. Mikić et al. (1999) used a sequence of whole-sun magnetogram maps from 14 Carrington rotations and interpolated them to 10 equal time intervals between maps (about 2.7 day intervals) to provide time-dependent boundary values over a 13 ½ month long period. They considered the resulting time evolution as "quasistatic" that was able to simulate the emergence of the corona from solar minimum with an increasing complexity.

Mikić et al. (1999) went on to formulate a non-adiabatic version of their model ($\gamma = 5/3$) to overcome the limitations of their adiabatic assumption. The energy exchange term in their thermodynamic energy equation was formulated to include parameterized coronal heating, heating from Alfvén waves, viscous and resistive dissipation, and radiative heat loss. Separate heat flux terms were assumed for the collisional regime ($r < 10\ R_s$) and collisionless regime ($r > 10\ R_s$). The parameterization of coronal heating was a negative exponential function of radial distance from an imposed latitudinal variation of the volumetric heating at $r = R_s$. The advanced version of the model included an equation for the evolution of wave pressure to simulate the acceleration of solar wind by Alfvén waves. The new lower boundary for the coronal model was set at the top of the transition region between the chromosphere and the corona. A specification

of coronal heating distribution at this level replaced a constant temperature assumption, and density was calculated locally through a balance of radiation loss, thermal conduction and heating within the chromosphere and transition region. An axisymmetric (longitude slice) 2-D model was constructed incorporating these upgrades. Improved agreement of the solar wind properties with measurements at L1 was realized through extensive simulations, and density differences between coronal holes and streamers were more realistic.

Lionello et al. (2001) extended the 2-D version of the model downward to smaller radii by setting its lower boundary in the chromosphere, so that the upper chromosphere and entire transition region was included in the model domain. Temperature (T = 20,000 K) and density at the lower boundary was specified as a fixed value typical of the chromosphere rather than computed. Because the model was two-dimensional in radial and latitudinal directions, smaller grid intervals in the radial (56 km) and latitudinal (0.4º) were used. They state that imposed resistivity and viscosity have to be set larger than those from the real solar environment. This implies that greater diffusive damping of the magnetic field and plasma is required to generate a realistic solution. A steady state solution that adequately describes the large-scale properties of the corona, but not its small-scale behavior, was reached. The authors showed that there was greater latitudinal variation in coronal temperature and density with the chromosphere version of the model than with an adiabatic energy equation version. This is true of the plasma property differences between regions of open and closed magnetic field lines as well. When the model base was moved outward to the transition region at a greater temperature (T = 500,000 K), they found that the shortest magnetic field closed loops had much warmer temperatures than in the chromospheric version. However, the temperature and density of the plasma in the upper portions of the coronal streamer were comparable. By setting the lower boundary outside the chromosphere, the outward enthalpy flux was curtailed and an additional term was added in the energy equation to account for this effect.

Eight years later the same three authors (Lionello et al., 2009) presented a 3-D version of their diabatic MHD corona model with energy exchange formulations in the thermodynamic energy equation. They termed this version the thermodynamic MHD corona model and applied it to the time period of a single Carrington rotation. The same form for energy exchange due to heat flux and radiation loss in the earlier 2-D version (Mikić et al., 1999) were used, but heating due to Alfvén wave dissipation and viscous and resistive dissipation were not included. Because the actual mechanisms that cause coronal heating are not known, the authors experimented with three alternative formulations for the large-scale heating term in the energy exchange. The resulting steady state solution was very sensitive to the formulation used, particularly in the plasma density and temperature distribution. A magnetogram of the photospheric magnetic field was constructed from line-of-sight optical telescope images from a complete Carrington rotation. A non-uniform grid with a minimum radial grid interval of about 300 km, average latitude spacing of 1.8º, and minimum longitude spacing of 1º was used for the computations. A resistivity associated with a resistive diffusion time considerably less than observed was employed to damp sub-grid magnetic structures. The same strategy was implemented in specifying viscosity to minimize unresolved plasma features. A fixed coronal base temperature and number density value characteristic of the chromosphere were specified. Adjustment of the thermal conduction of heat from the corona to the transition region and the radiative heat loss by the transition region was made to ensure that their product is constant to maintain realism of the corona near the base. This modification broadened the transition region significantly, but left the coronal solution essentially unchanged.

The first of the three alternative coronal heating rate formulations was a negative exponential function of radial distance. The second method imposes a heating in each grid cell intersected by a closed field line emanating from the model lower boundary that is a function of the half-length of the field line loop and the local magnetic field magnitude. For open field lines, the heating rate from the first formulation was applied. The third coronal heating method involves the sum of the first method (negative exponential), a quiet Sun contribution that is a function of the local magnetic field vector components, and a third term due to active region heating. The magnetic field vector was initialized on the computational grid using a PFSS extrapolation from the photosphere magnetogram. The plasma temperature, density and velocity were specified based on a previously computed 1-D solar wind solution. The model was integrated to a steady state solution in sequence for each of the coronal heating formulations – after reaching steady state with one formulation, the model was continued with the next formulation until it again reached steady state, and so on.

The authors applied a method of developing synthetic emission images from the model output at specific wavelengths. The images created from the three steady state solutions, corresponding to each of the three coronal heating methods, were compared with extreme ultraviolet (EUV) and x-ray images from satellite-based telescopes. The comparisons showed that the first coronal heating formulation, the simple decaying exponential, produces too little emission over most of the solar disk. Whole disk synthetic images from the coronal heating methods 2 and 3 showed a realistic representation of the major features apparent at the time, including a large polar coronal hole extension, quiet sun regions, and an active region. Emission intensities were compared quantitatively along cross section cuts lying along the solar equator and intersecting a major active region. In both cases, heating model 3 appeared to better match the observed emission than heating model 2.

The first appearance of the model's current name, Magnetohydrodynamics Around a Sphere (MAS), that I could find was by Riley et al. (2011). The model they used to achieve a steady state solution for the corona during a single Carrington rotation period is the "thermodynamic MHD corona model" described by Lionello et al. (2009). In their paper, they describe its use in conjunction with what they term their heliospheric MHD model. The latter is essentially the same general MHD equations but assuming adiabatic plasma compression and expansion (i.e., zero energy exchange in the thermodynamic energy equation). Their work with the coupled corona and heliosphere models will be discussed in more detail in Section E.

2. Space Weather Modeling Framework (SWMF) Solar Corona (SC)

The current Space Weather Modeling Framework (SWMF) Sun-to-Earth modeling system evolved from a space plasma simulation program called BATS-R-US developed at the University of Michigan for space applications. Powell et al. (1999) presented a general compressible magnetohydrodynamics model intended to simulate astrophysical plasma flow. The MHD equations were cast in spectral form, and solved with an approximate Riemann solver using a so-called solution-adaptive scheme. After discussing a number of possible solution techniques, Gombosi et al. (2001) proposed a solution method for the MHD equations governing an ideal, non-relativistic, compressible plasma. They referred to the method as a block-based adaptive mesh refinement (AMR) technique, in which the governing equations were integrated forward in time to obtain grid volume average values in rectangular Cartesian grid cells. The computational cells were organized in blocks of equal sized cells, but the various blocks

occupied differing volumes of physical space. The adaptive computational grid was originally designed to resolve phenomena on varying spatial scales, including plasma disturbances like coronal mass ejections. The local grid spacing could adapt both up and down scale to the size of the motions within the blocks, directed by physics-based refinement criteria.

Groth et al. (2000) reported on the same model, explaining that the assumption of an ideal plasma includes neglecting effects of resistivity and viscosity, ignoring kinematic effects such as wave pressure due to Alfvén waves, and not distinguishing between the separate roles of electrons and ions in the plasma. An empirical energy exchange term, which they called the volumetric heating function, was included in the thermodynamic energy equation to allow diabatic (non-polytropic) plasma compression and expansion assuming $\gamma = 5/3$. It was formulated in an attempt to represent heat flux, thermal conduction and radiative losses in the corona. The coronal heating formulation involved several adjustable parameters, which were tuned to replicate the plasma properties of the solar wind at 1 AU. The heating function was parameterized to produce outflows from open field lines at high solar latitudes and prevent outflow and maintain closed field lines at low latitudes. Thus, the solar wind speed was primarily latitudinally dependent. Boundary values of the magnetic field at the inner boundary r = R_s were set from a specified formula rather than drawn from magnetic field measurements. Spatial extent of the Cartesian computational grid was from -32 R_s (behind the Sun) to 224 R_s in the Sun-Earth (x) direction, and $\pm$ 192 R_s in the longitudinal (y) and solar rotational axis (z) directions, where the x-y plane was in the solar equatorial plane. No distinction was made between a computational domain for the corona and the inner heliosphere. In fact, the same model framework was used to simulate the coronal mass ejection and its impact on the terrestrial magnetosphere. The model equations were integrated to a steady state, and coronal holes were produced at high latitudes while closed field lines and a coronal streamer with a current sheet was formed near the equator. The authors acknowledged the consequent oversimplification of the coronal magnetic field with this formulation, but saw it as a step toward more advanced models of the future. They used the steady state solution of the corona and heliosphere as "initial conditions" to model the propagation of a coronal mass ejection from the Sun to Earth's magnetosphere.

Roussev et al. (2003) continued the development of the Powell-Gombosi model using the Block Adaptive-Tree Solar-wind Roe-type Upwind Scheme (BATS-R-US) code. They proposed an energy exchange mechanism for coronal heating involving heat transfer between the plasma and large-scale MHD turbulence. They adopted a polytropic index for the thermodynamic energy equation that was a linear function of plasma temperature in conjunction with treating waves and turbulence as significant energy sources for coronal expansion. This empirical technique was a "bridge" between a nearly isothermal assumption to a full energy equation formulation based on energy exchange between turbulence and plasma heating. Using this functional form, they derived the temperature as a function of radial distance from the differential form of the equation of state and hydrostatic equation. This resulted in a range of γ from 1.154 at R_s to 1.491 at 1 AU. These values were held constant during the model integration. Lower boundary conditions were specified using a temperature and pressure variation in latitude and longitude that was a linear function of the radial magnetic field. The parameters for the function were chosen to ensure good agreement between modeled solar wind properties and measurements at L1. Density was consequently derived through the equation of state. The lower boundary radial magnetic field was imposed from global magetograms and the coronal magnetic field was initialized using the PFSS model.

The concept of distinct but coupled 3-D MHD models among separate spatial domains between the Sun and the Earth was first presented by Tóth et al. (2005) as the Space Weather Modeling Framework (SWMF). The basic MHD model formulation, tailored for each of the spatial domains, was descended from that of the model presented by Tombosi et al. (2001) and Groth et al. (2000). They stated that the interactions between a domain to be modeled and a contiguous domain may be handled in three ways: using available measurements at the boundary to represent the effects, employing statistical or phenomenological models to specify information on the boundary, or to run the relevant model in the contiguous domain as well and use its output. It was the last of these methods that was promoted in their paper, in the hope that the full suite of Sun-to-Earth domain models can be executed in an efficient manner to produce timely simulations.

Originally, the addition of models for the Earth's magnetosphere, ionosphere and upper atmosphere to the Powell-Gombosi model led to an inflexible "monolithic" model of the plasma and magnetic fields of the Sun-Earth system. It prevented the ability to run only the models from selected domains, and to execute different domains concurrently on massively parallel computer architectures. A modeling "framework" allows for the joining together of disparate models using standardized interfaces. This makes the system modular, permitting a user to select combinations of models (or to substitute measurements at the model combination boundary) that are physically reasonable to execute a desired simulation without having to make changes to the model's codes.

In the SWMF developed by the Center for Space Environment Modeling at the University of Michigan and its collaborators, the individual model modules are self-contained yet allow connection to each other for contiguous domains. Each model has its own model equations, computational algorithm, grid structure and time-differencing scheme. The contiguous domains may overlap or interface on a common boundary. The framework even allows for the incorporation of domain models external to the SWMF with a limited amount of code modification required. Tóth et al. (2005) briefly described models for each of the following Sun-to-Earth domains/phenomena and the results of their preliminary tests: solar corona (SC), eruptive event generator (EE), inner heliosphere (IH), solar energetic particles (SP), global magnetosphere (GM), inner magnetosphere (IM), radiation belt (RB), ionosphere electrodynamics (IE), and upper atmosphere (UA).

The physical domain of the SWMF SC model extended from about $1\,R_s$ to $24\,R_s$. The standard version of the model used the formulation of Groth et al. (2000) for the coronal energy exchange term (their "volumetric heating function") in the thermodynamic energy equation. Alternative formulations were available, such as through the use of a variable adiabatic index or through energy transfer between the plasma and large-scale turbulence following Roussev et al (2003). The model equations could be solved in an inertial reference frame or a rotating frame of reference (that included the inertial forces). The model's lower boundary was set just above the photosphere (i.e., in the lower chromosphere). Magnetic field lower boundary values could be imposed from photospheric magnetograms or specified by a simple dipole formula. No mention is made of initialization of the magnetic field or plasma state in the SC model. The model allowed for single whole-Sun values or the method of Groth et al. (2000) to declare the boundary values of temperature and density in accord with the latitudinally-dependent energy exchange formulation. The SC model solution provided magnetic field and plasma properties for the IH model, which was allowed to overlap the SC model domain. This allowed for a smoother

transition of the data between the models, avoiding reflections or numerical artifacts resulting from the differing grids and time steps.

The SWMF EE model could be embedded within the SC model only – that is, the SC model had to be executed to implement the EE model. Its domain was entirely contained within the defined eruptive event, typically a coronal mass ejection. Its initial representation could be in the form of a boundary condition for the SC model, or a perturbation of the SC initial conditions (in the time-dependent SC version). Its only interaction was with the SC model.

Downs et al. (2010) used techniques of lower corona energy exchange similar to those of Lionello (2009) to reset the lower boundary of the SWMF SC model in the chromosphere so that the entire transition region was included in the model domain. At these levels in the Sun's atmosphere they included the effects of coronal heating, heat conduction and radiative cooling in their thermodynamic energy equation. Two empirical coronal heating formulations were employed in separate experiments – one was a function of the photosphere magnetic field magnitude that represents solar energy input to the corona, the other the simple negative exponential of radial distance from the center of the Sun that was the first alternative coronal heating scheme of Lionello et al. (2009). Boundary values were supplied from photospheric magnetograms and extrapolated onto the coronal grid using the PFSS model. Then based on whether the initial magnetic field state had open or closed field lines, either a negative exponential heating with a smaller rate constant was applied, or it was implemented along with the chosen coronal heating formulation used in that experiment. No heating due to Alfvén wave dissipation was taken into account. The lower boundary was set separately in two experiments. In the primary formulation, the lower boundary was specified by a constant temperature (20,000 K) and density characteristic of the chromosphere, and a method for broadening the transition region was included so that it could be fully resolved by the model. In the alternative formulation, called the radiative energy balance, the base temperature was set to that of the high transition region (500,000 K) and a heat balance was assumed from this level down to the top of the chromosphere. The base density was then derived by integrating the MHD energy equation at constant pressure from the top of the chromosphere to the base temperature level.

Synthetic emission intensity images were generated from model output and compared with observation imagery at specific wavelengths. Results showed that both lower boundary formulations, when run with the coronal heating dependent on magnetic field magnitude, were able to represent the major features of the quiet Sun regions. The radiative energy balance condition led to smoother emission structure and slightly higher temperatures than the chromospheric lower boundary case. But the former had a computational efficiency advantage over the latter in that it did not include computations for the transition region. The magnetic field magnitude-dependent coronal heating produced more realistic coronal emission structure than the simple exponential decay formulation, especially near coronal holes and active regions. But the latter did represent the major emission features of the quiet Sun regions. In an experiment in which the coronal heating formulation transitioned from exponential decay to magnetic field-weighted in areas of strong magnetic field strength, the hybrid heating model was able to represent the greater variation in the coronal emissions in the same way as the full magnetic field-dependent coronal heating model. This led the authors to suggest that coronal heating formulations might not benefit from greater empirical complexity as they might from a more sound physical basis.

In that spirit, Sokolov et al. (2013) proposed a coronal heating parameterization based on Alvén wave turbulence dissipation. In fact, in their version of the SWMF SC model, they

considered magnetic field perturbations to be the main source of heating from the top of the chromosphere through the transition region and into the low corona. In their paper, Sokolov et al. (2013) also suggested that this energy source is sufficient to explain the increase in solar wind speed between regions of closed and open field lines. The authors associated the magnetic field magnitude-dependent coronal heating function of Downs et al. (2010) with the dissipation in the Alvén wave turbulence – that is, the ad hoc formulation is accounting for the physical wave dissipation mechanism. They developed a parameterization of the coronal heating due to Alfvén wave turbulence dissipation to replace the empirical functions. The basic premise for their parameterization is that wave dissipation rate is affected by the intensity of oppositely propagating waves. They theorize that regions of open field lines, like coronal holes, have a lower intensity of incoming Alfvén waves than close field line regions, and thus have a reduced turbulence dissipation rate and thus less heating. Another basis hypothesis is that the energy of the propagating waves emerging from the photosphere (referred to as the Poynting flux) is directly proportional to the magnetic field magnitude at the photosphere. They assume that all of the energy of the waves moving from the photosphere to the low corona is absorbed there. The turbulent energy dissipation is also dependent on the wave frequency, and the energy dissipates as a result of the cascade from long- to short-wavelengths. Wave turbulence is considered isotropic in closed field regions (equal wave energy density for incoming and outgoing waves), governed by a Kolmogorov spectrum. Total volumetric heating due to the turbulent energy dissipation was determined to be a function of the Alvén wave intensity, which is the integral of the wave energy density over all frequencies.

D. Inner Heliosphere Models

1. Enlil

Stand-alone inner heliosphere models are free of the concerns about open or closed field lines and coronal heating functions. With an inner boundary at some distance (usually > 20 R_s) from the Sun, they generally depend upon solar corona models for their inner boundary conditions. The primary objective of existing 3-D MHD models of the inner heliosphere is to simulate the steady-state conditions of the solar wind and the IMF given a specification of the magnetic field at the photosphere. As the Sun and simulated inner heliosphere rotates, a point downstream (like at L1) experiences the solar wind and IMF conditions that cross the Sun-Earth line. Because of the role of open and closed field lines in dictating solar wind properties, the inner heliosphere model's performance is directly affected by the veracity of the configuration of the corona's magnetic field lines as generated by the solar corona model. In fact, Norquist (2013) found that the specification of the photospheric magnetic field used as inner boundary values for the corona model can lead to as large of differences in the solar wind speed at L1 as can the inner heliosphere model used to generate the simulation.

The Enlil 3-D MHD model of the inner heliosphere (Odstrcil and Pizzo, 1999) was originally used to host the simulation of a coronal mass ejection to study its effect on the IMF. It assumed ideal MHD conditions (as explained above in Section C.2 in the discussion of Groth et al. (2000)) in which the prognostic variable in the (adiabatic) thermodynamic energy equation was the "thermal energy density" = pressure/(γ - 1) with γ = 5/3 for an ideal monatomic gas. Without an energy exchange term, in addition to assumption of inviscid, unresistive plasma flow, the equations were considerably simpler than their coronal model counterparts. With prognostic

equations for the plasma pressure and density (equal to the proton mass times the number density), the plasma temperature was diagnosed from the ideal gas law. Their version of the model also included two mass continuity equations for injected particles to track mass and magnetic field polarity associated with the CME. Because the IMF in interplanetary space is considered "frozen in" the solar wind plasma, the IMF polarity is passively advected by the plasma flow.

The model equations were solved on a spherical grid in radial position, colatitude, and longitude. The boundaries of the computational grid were at defined radial distances (inner and outer), fixed meridional angles (north and south), and fixed azimuthal angles (east and west). Inner and outer boundaries were at 0.14 and 1.04 AU respectively, the meridional boundaries were at 30º and 150º colatitude, and the azimuthal boundaries were from the east to west limbs (0º to 180º). The computations were carried out using an explicit time-differencing scheme with a space-differencing on a regular spherical grid of radial spacing 1.075 R_s and 1º in colatitude and longitude. Free flow boundary conditions were imposed on the outer and meridional boundaries, and the azimuthal boundaries were periodic and assymetric. The computational grid rotated with the Sun, so that the steady-state solution sweeps by a fixed point in the inner heliosphere (for example, L1) at a rate of approximately one grid point each 1.8 hours. The radial solar wind speed on the inner boundary was specified by a function of latitude in a coordinate system tilted at a fixed angle with respect to the solar rotational axis, such that speeds were slower near the tilted coordinate system equator and faster at higher latitudes. The nonradial plasma flow was set to zero on the inner boundary. They were held constant in time while the model integrated forward in time to steady state beginning with arbitrary solar wind values imposed as initial values on the computational grid. The plasma density on the inner boundary was set to be proportional to the inverse square of the imposed radial speed, so that the radial momentum flux was essentially unvarying on the inner boundary. The inner boundary temperature was specified as proportional to the inverse of the imposed density, so that the imposed pressure was constant on the inner boundary. A simple monopolar IMF was imposed initially throughout the computational domain, with initial values of the radial component of the magnetic field constant and positive on the inner boundary. The inner boundary azimuthal magnetic field component was a function of the sine of colatitude and the inverse of the radial solar wind speed to account for solar rotation, while the meridional component on the inner boundary was set to zero.

The resulting steady-state solution produced regions of plasma compression and rarefaction in the inner heliosphere where fast streams interacted with slow streams after sufficient rotational time. The IMF lines were wound backward from the direction of rotation to a degree dependent on the solar wind speed – less extended in slower flow and more extended in faster flow. The arrival of a fast stream at a specified heliospheric point (e.g., L1) results in a decrease in density due to the imposed inverse square relationship with solar wind speed, but an increase in magnetic field magnitude as the IMF field lines are stretched outward toward the point in the fast flow. When slow flow occurred at the point, a slight rise in density and a dip in magnetic field strength resulted in the plasma rarefaction region.

Odstrcil (2003) used the same 3-D MHD model of ideal plasma flow as a basis for solar wind and IMF steady-state simulations in the inner heliosphere. In addition to again considering interaction of a simulated CME with the background ("ambient") heliospheric state, he also attempted to introduce more realism in the undisturbed, large-scale solar wind and IMF simulation. In this paper, Odstrcil emphasizes the "global 3-D interactions" between the

simulated CME launched from the low-latitude streamer belt and the solar wind in the inner heliosphere. He displays a case from his earlier paper in which a CME propagating within the streamer belt becomes trapped between the slow streamer plasma flow and the fast streams behind it coming from a coronal hole. However, the southern portion of the CME extended into a fast stream south of the solar equator and was distended outward, giving it a radial width much greater than in the northern hemisphere. While this situation was hypothetical and no attempt was made of verify its realism, it did demonstrate the modifications that the ambient solar wind environment can make on a heliospheric transient in the simulation.

Odstrcil (2003) makes the case that global 3-D MHD numerical models would be capable of producing realistic time-dependent predictions of solar wind properties near the Earth if the needed time-dependent conditions near the Sun were available. However, truly prognostic models of the corona required to provide such conditions were still steady-state in formulation, anchored to a synoptic magnetogram describing a snapshot of the magnetic field of the photosphere. It would require a time-dependent photospheric magnetic field flux transport model coupled with a time-dependent coronal model to generate the temporal sequence of inner boundary conditions required by a time-dependent inner heliopshere model.

In this paper, Odstrcil (2003) executes the WSA coronal model daily from daily-updated magnetograms, producing the steady-state radial magnetic field on the Enlil inner boundary at 21.5 R_s. From this he derived the radial solar wind speed using a simple empirical relationship with the radial magnetic field expansion factor between the photosphere and the source surface at 2.5 R_s. The azimuthal component of the magnetic field was a function of the radial magnetic field, sine of colatitude, rotational speed of the Sun and the derived radial solar wind speed. The meridional magnetic field component and the azimuthal and meridional solar wind speed components were assumed to be zero. He used the same assumptions for density and temperature on the inner boundary he did in his earlier study (Odstrcil, 1999). He then ran Enlil to steady state for each day and analyzed the numerical outputs at L1 against observations. The author does not divulge information on what he considers his steady state solution. Lastly, a solar corona model was coupled with the Enlil inner heliosphere model to perform simulations of CMEs and investigate their density distribution.

2. Space Weather Modeling Framework (SWMF) Inner Heliosphere (IH)

As mentioned above in Section C.2, the SWMF modeling suite includes separate models for distinct physical domains between the Sun and Earth. Tóth et al. (2005) included a section of their article on the SWMF that describes the IH model. The following is a summary of their description.

The spatial domain of the IH model overlapped with that of the SC model. It extended from 20 R_s out to 1 AU and beyond. As with the Enlil inner heliosphere model, it assumed ideal MHD in its formulation, obviating a need for energy exchange processes in its assumption of adiabatic conditions for the monatomic ideal gas. Its model equations followed from Tombosi et al. (2001) and Groth et al. (2000) without the volumetric heating term in the thermodynamic energy equation. The computational grid construct was flexible, not requiring that it conform to that of the SC whose steady state solution from a magnetogram would be its normal source of inner boundary values. There was no apparent description of how the computational domain is initialized. It uses the same block adaptive mesh refinement scheme as in the other BATS-R-US

codes. The plasma density, velocity, and pressure along with the magnetic field are explicitly solved in steady state, and the temperature is diagnosed from the equation of state.

E. Combined Corona and Inner Heliosphere Models

1. Hayashi

The magnetohydrodyamic models of K. Hayashi exemplify the attempts to fashion a single solar wind formulation that spans both the sub- and super-Alfvénic regimes in the corona and free interplanetary space respectively. In Hayashi (2005) he lays the groundwork for this type of MHD plasma model that is fairly typical of the coronal models of that time. The model formulation is closest to that of Groth et al. (2000), except that in the thermodynamic energy equation, the prognostic variable is "energy density" that incorporates the kinetic energy, gas pressure and magnetic pressure of the plasma. Unlike Groth et al. (2000), he makes no attempt to represent a coronal energy exchange process, and keeps the equations polytropic in using $\gamma=1.05$ to simulate the trans-Alfvénic solar wind. Thus, the uniformity of a single model results in compromises in order to capture the entirety of the corona and inner heliosphere. The contribution made in Hayashi (2005) involves the lower boundary condition treatment for the corona. The author makes the case that a simple assignment of temperature and density that is fixed in time may result in unrealistic coronal structure. Instead, he offers the use of Ulysses satellite data to constrain the lower boundary conditions using four different cases based on regimes of the radial plasma flow velocity at the lower boundary. The assumption of a fixed radial magnetic field component at the photosphere was made, and the three cases were made for plasma fluxes less than the observed average (fixed temperature and density), no plasma flux (in closed magnetic field regions), and a limited mass flux greater than the observed average (in coronal hole regions). The resulting 2-D model was run to steady state for these cases. The author claimed to find good agreement with the Ulysses measurements, and that reasonable variation of the radial plasma flux between closed field line streamers and open field line coronal holes were obtained. The author acknowledges that the use of a polytropic assumption of $\gamma = 1.05$ results in an unrealistic slow solar wind due to a lack of sufficient coronal heating and consequent plasma acceleration.

Hayashi (2006) presents a summary of his earlier work, but simulated in three dimensions. As before, he fixed the radial component of the magnetic field on the inner boundary in time, leaving two constraints on the radial mass flux: limiting mass flux simulating closed field regions, and varying or fixing density, temperature or pressure on the inner boundary as chosen for the simulation in question. The boundary values of the photospheric magnetic field were set according to a full Carrington rotation magnetogram, while the initial values of the magnetic field were set according to a solution of a potential field source surface model and of the radial plasma velocity according to the standard Parker spiral solution. During the resulting steady-state solution of the model, the mass flux was restricted in the streamer region and was outward in the open field line regions. Once steady-state is achieved, the presence of some plasma flow in the closed regions stretched the closed field lines, and some field lines were extended to allow plasma flow in the inner heliosphere. Using a particular constraint on the inner boundary to fix the temperature and allow the density to vary in time, the steady-state solution was able to reproduce the basic features of the observed spatial density variation. The author concedes that, in the case of only super-Alfvénic plasma flow in the inner heliosphere,

reasonable solutions at distances out to 6-7 AU can be obtained from fixed (photospheric) inner boundary conditions. This concedes the point that specific inner boundary conditions are not required to obtain realistic solar wind simulations downwind.

In Hayashi (2012) the author gives up on the idea of continuing with a unified coronal and inner heliospheric model, and concentrates just on the latter using time-varying radial magnetic field and plasma velocity specifications on an "inner boundary" of 50 R_s. While he was lead author on a few intervening studies, this one summarizes the work on time-dependent (as opposed to steady-state) solar wind from observation-based values. It is included in this section to show the evolution from a single combined corona and inner heliosphere model to separate domain formulations. The paper concentrates on developing boundary conditions external to the corona for the time-varying radial component of magnetic field that maintains the required divergence-free conditions. They developed an algorithm for generating the observation-based boundary conditions that met three requirements: that the boundary radial magnetic field will be the same as observations that sequentially will be available to generate long-term simulations; the divergence-free conditions will be met at all times; the generation of the boundary conditions by the algorithm will be computationally inexpensive. The data were derived from magnetograms making up nine Carrington rotations along with corresponding line-of-site interplanetary scintillation (IPS) measurements from ground-based telescopes to make tomographic reconstructions of solar wind speed maps. The author conceded that such a source of solar wind data obviates the need for solar coronal model that has as yet indeterminate formulations for coronal heating and consequent solar wind accelerations.

The spherical coordinate grid extended from 50 R_s to 1250 R_s with 3 R_s radial grid spacing, and was 2.8125º in latitude and longitude encompassing an entire sphere. The MHD equations used were those of Hayashi (2006), and they use $\gamma = 1.46$ as derived from observed data in the heliosphere. An inertial frame was invoked rather than a rotating reference frame since the inner boundary is distant from the Sun, but boundary values on the 50 R_s sphere were assumed to be moving longitudinally at the solar rotation rate at that distance. Plasma velocity, density and pressure on the inner boundary are determined from the IPS data, and radial magnetic field is determined from the PFFS model applied to the magnetogram data to the 2.5 R_s source surface, then extrapolated outward to 50 R_s. This was done once for each Carrington rotation on the full sphere of the inner boundary using the supplied data. Then the required inner boundary values of plasma radial velocity, pressure, temperature and density along with radial magnetic field in each grid volume was linearly interpolated in time between Carrington rotations to supply the time-dependent values. This choice of full Carrington rotation interpolation intervals was arbitrary – any time interval could have been chosen, but that would require re-specification of the boundary values at those smaller time intervals. While the plasma quantity interpolates were not a problem, those of radial magnetic field always had to be non-divergent. To handle this, they assume the magnetic field in a thin shell near 50 R_s is potential, and solve Laplace's equation for the magnetic potential at each Carrington rotation time. Then at each grid point they add a single model time step's increment of the Carrington rotation magnetic potential difference to the magnetic field vector at each time step. Then the latitudinal and longitudinal magnetic field components are adjusted in accordance with Faraday's law on the boundary to maintain non-divergence – thus, they are assumed to meet this criterion.

Nine steady-state solutions were generated from the Carrington rotation maps, and one time-dependent solution was computed from the middle of the first Carrington rotation to the middle of the ninth. The plasma properties and magnetic field values simulated by the model

executions were compared with in-situ measurements at L1. The time series of the model simulations (steady-state for each CR vs. time-dependent over all CR) were similar, much more so that either replicated the measured data. The time-dependent simulations were smoother, with smaller maxima and larger minima than for the steady-state solutions that the author attributes to their time-interpolation to connect them in a steady stream of input data. As a result, correlations and skill scores were slightly better for the time-dependent solutions. Running the time-dependent version of the models allowed for several advantages: being able to solve for much greater heliospheric distances (allowing for the time it takes to reach them), integrating the model continually for periods of input data availability and frequencies of update, and not having to restart the model for each input and arrive at steady-state before producing a usable solution.

2. Coupled MAS and Enlil (CORHEL)

After Lionello et al. (2001) published their work on the coronal modeling and Odstrcil (2003) did the same for his model of the inner heliosphere, the two joined forces in a publication led by Odstrcil (Odstrcil et al., 2004). In their abstract, they touted the notion of "coupling" corona and heliosphere models by stating that it was an efficient way to treat the different physical realms. Yet they state in their text that "a complete picture requires a comprehensive model of all of the processes considered together." For convenience, however, they link together the two models by assuming that the corona model can pass information to the heliosphere model in the super-sonic, super-Alfvénic zone that they claim extends inward to about 18 R_s. The coronal heating processes that may cause plasma acceleration do not operate in the heliosphere, and in the latter realm the plasma particles expand adiabatically.

At that time, the corona model of Lionello et al. (2001) was still using a polytropic formulation in two dimensions (radial and latitude). Ostrcil et al. (2004) used the Enlil model described above to simulate heliospheric processes. Again, it assumed ideal MHD conditions in which the prognostic variable in the (adiabatic) thermodynamic energy equation was the "thermal energy density" = pressure/(γ - 1) with γ = 5/3 for an ideal monatomic gas. This avoids energy exchange processes important in the corona that must be represented in order to realistically simulate plasma acceleration close to the Sun. The corona model produced a steady-state solution of the 2-D distribution of plasma density, temperature, flow velocity vector and magnetic field vector on the corona-heliosphere interface. In this paper, he refers to an earlier publication (Ostrcil et al., 2002) in which he states that the coupling procedure is explained. Briefly, in that paper it states that the corona model solves the MHD equations on a 2-D grid of between 5,110 km (near photosphere) and 413,000 km (at outer boundary of 20 R_s) radial grid spacing and between 0.24º and 2.4º latitudinal spacing increasing from equator to pole. The computational grid of the heliosphere model began at 20 R_s and had constant grid spacing of 413,000 km and 0.5º respectively. An interpolation in time and space was deemed necessary to pass the needed values between the models. The corona model was executed to five days whereupon it reached a steady state. The resulting solution was extrapolated outward to initialize the heliosphere model, while its solution on the outer boundary was used as inner boundary values for heliosphere model. The latter model was then integrated ahead in time another five days to reach its steady-state solution. Normally, when both models are operating in steady-state and only background ("ambient") conditions were present, no concerns about temporal interpolations would be involved. However, they found that when heliospheric transients like a CME was introduced into the coronal model, temporal intervals of no frequent

than 1 h are necessary to pass information from the corona to the heliosphere model to preserve the transient's integrity as it passes through the interface.

They experimented with setting the interface boundary at 25 and 50 R_s, thinking that the coronal model solution in this realm should be very much like its heliosphere counterpart. What they found is that the 50 R_s interface is an excessive outward extension of the warmer plasma of the corona, given that the corona model they used was nearly isothermal. Another thing they noticed was that the plasma density at 1 AU was too large by a factor of about three – they attributed this to the near-isothermal assumption of γ=1.05 in the corona model. They acknowledge that by increasing this parameter they require the solution of energy exchange processes in the corona leading to greater complication (looking ahead to later work). Coronal heating must be allowed in some form, and they suggested that heating due to Alfvén wave dissipation and consequent plasma acceleration may be necessary. They also varied γ in the heliosphere model, varying it from 1.5 to 5/3. In just that relatively little difference, the 5/3 factor allowed greater adiabatic expansion of the plasma near 1 AU and thus unrealistically cool plasma compared with observations. Accordingly, plasma speeds were too small as well.

A similar study was conducted by Luhmann et al. (2004) in which they also coupled a magnetospheric model and a thermospheric model. They emphasize the physical interchanges between the physical modules, yet recognizing their distinctive computational domains. This is similar to what evolved into the modular Space Weather Modeling Framework mentioned earlier. In their study they inserted a simulated coronal mass ejection into the corona module (which was the MAS model) and allowed it to propagate outward through each interface between contiguous modules. Because of the focus in this review of just corona and heliosphere models, we limit comments here on just their aspects of those topics from their paper.

Though this study does not reference Lionello et al. (2001), its description of the 2-D corona model seems to be the same one. It is polytropic with γ = 1.05 with no allowances for coronal heating mechanisms. Its computation grid extended to 30 R_s having increasing grid spacing poleward and outward, which was initialized using a potential field based on photospheric magnetograms. A constant density was assumed on the inner photospheric boundary and a Parker-style solar wind outflow specified the plasma velocity initial conditions. They comment that though the corona model can reasonably simulate the closed and open field line distributions when a photospheric magnetogram are used for inner boundary conditions, with consequent gradients in the solar wind, its plasma speeds are considerably smaller than observed. They suggest that the simple coronal models without sufficient coronal heating processes cannot produce realistic outward acceleration of the plasma. This required that the radial solar wind output from the coronal model was increased as it was passed to the heliosphere model to result in more realistic solar wind speeds in comparison to L1 observations. They utilized the "quasi-static" sequence of inner boundary conditions derived from Carrington rotation photospheric maps as per Mikić et al. (1999) as described above. This type of time-dependence avoided reaching a steady-state in each module before passing generated conditions to the next module. In this way, the continually evolving outer boundary conditions from the corona model (MAS) was directly passed to the heliosphere model (Enlil) allowing for time step and grid cell differences. The solar rotation was accommodated by advancing the corona model output longitudinally to meet each successive heliosphere model time step. This direct transfer allowed the CME properties to pass from corona to heliosphere model without distortion.

The synthetic simulation of the CME initiated in the helmet streamer along the Sun-Earth line but depressed with a southward magnetic cloud orientation. The CME flux rope and part of

the helmet streamer was ejected into the outer corona. It drove into the slower wind ahead of it and reached a propagating speed of more than 500 km/s at the outer corona model boundary. In their simulation the heliosphere model established a steady-state solar wind solution before the introduction of the CME into its outer boundary. In the CME propagation in the heliospheric model, a region of high temperature and density formed ahead of the flux rope representing the sheath behind the shock ahead.

3. Coupled MAS and MAS-Heliosphere

Riley et al. (2011) present results from a combination of the advanced corona model of Lionello et al. (2009) with a model appropriate to the inner heliosphere (Riley et al., 2001). The major differences between the two is the incorporation of thermodynamic energy equation in the former (as described above) to attempt to include the coronal heating mechanisms and resulting plasma acceleration in the corona – the sub-Alfvénic domain. As we saw above, the super-Alfvénic realm in the inner heliosphere does not involve the hotter, denser plasma closer in the corona, so that it can be simply simulated by more nearly isothermal exchanges. In addition to the direct transfer from the corona to the heliosphere model, the study also experimented with an empirical input to the latter. In this case, the input on the inner boundary of the heliosphere model appeared to be a hybrid that is primarily driven by solar wind that was considered slower near the open and closed field lines and faster within clearly open field lines from coronal holes. They used the corona model-generated magnetic field along with plasma temperature and density consistent with momentum conservation and thermal-magnetic balance on the inner boundary of the heliosphere model set at 30 Rs.

Results from the pair of models were shown for two periods: the Whole Sun Month (WSM) of 10 August – 8 September 1996 and the Whole Heliosphere Interval (WHI) of 20 March – 16 April 2008. They first discussed some general characteristics related to the heliospheric conditions for the respective Carrington rotations of those periods as produced by the model combinations. These included helmet streamers, the heliospheric current sheet, and corotating interaction regions. They also compared results from the models with observations – first comparing simulated synthetic emissions against extreme ultraviolet imaging telescope images, and second against in-situ measurements. The former comparisons highlighted the corona model simulation outcomes, and major features like large coronal holes and a large active region were reproduced although not perfectly. These represented the distribution of open and closed field lines with the corresponding cooler, sparser plasma and warmer, denser plasma respectively. Smaller coronal holes and active regions were not simulated, and the rays of emission in the polar regions were not represented. In the WHI case, the simulation was unable to reproduce three distinct active regions near the equatorial region – the authors acknowledge that their corona model may not have simulated adequate structure in the corona that would have implications for solar wind characteristics. For in-situ comparisons, they compared the simulated plasma speed and IMF polarity to the STEREO A and B satellite sensors for two Carrington rotation periods respectively for just the WHI period. The model seemed to represent the two major high speed streams in the rotation fairly well. However, the model did not match the observed times of the negative and positive polarities, producing only one positive period in the rotation whereas there were two distinct positive periods observed. The authors ascribed the observed deficiencies of the model outputs on their sensitivity on differing photospheric magnetograms, a set of unknown model parameters, and assumed constant solar conditions

during each Carrington rotation. They hoped the planned high resolution temporal and spatial measurements of the Solar Dynamics Observatory (SDO) instruments would lead to more definite constraints for models.

In Riley et al. (2012) the authors focused on the inner heliopsheric model, acknowledging that there were significant uncertainties in the corona model in regards to producing realistic solar wind speeds. As above, they recognized that the simple polytropic assumption did not allow for sufficient coronal heating that was likely the acceleration mechanism for the plasma. Yet they could produce magnetic field structures that did appear realistic. On the other hand, the so-called energy exchange formulations included in the thermodynamic energy equation produced solar wind motions that were considered inferior to ad hoc specifications for the inner boundary of a heliospheric model. They laid the blame primarily to a lack knowing how to set the free parameters in the energy exchange formulations, which are frankly still unproven.

The authors promote the sequence of data and model steps referred to as the corona-heliosphere (CORHEL) package. The sequence began with a choice of a photospheric magnetogram to provide inner boundary conditions for a corona model. But it also required the choice of the more simply polytropic corona model or specification of physical parameters in the so-called thermodynamic model. In the CORHEL package described, they also offered the combination of the potential field source surface model and its extension the Schatten current sheet model – they are collectively packaged in the Wang-Sheeley-Arge corona model. While they included the Enlil model in the CORHEL package, they pointed out that it is limited to ± 60° latitude and thus more limited than MAS-Heliosphere.

They next discussed some results from the increased resolution of the heliospheric model in comparison to the older lower resolution model. Their higher resolution results showed more detail in the magnetic field structure at the inner boundary of the heliospheric model. The heliospheric current sheet was more finely resolved as well. The solar wind solution at the inner boundary also depicted more spatial variability in the more highly resolved model. They next compared the thermodynamic version of the coronal model in synthetic emissions with observed EUV imagery – their results were similar to those of Riley et al. (2011). Comparisons with in-situ measurements at STEREO A and B and at the ACE satellite at L1 revealed much different results depending on the Carrington rotation magnetogram used to initialize the coronal model. One magnetogram produced fairly good time series of solar wind speeds at the measurement locations, and a good change in IMF polarity. The other one was quite poor and failed to represent the high speed streams observed, along with a temporal mismatch of the polarity change. No one source of photospheric magnetograms consistently produced improved model results. The Carrington rotation magnetogram that performed more poorly initialized the more highly resolved version of the heliospheric model. While the solar wind results were somewhat improved in that they better matched with the observed high speed streams, the magnetic field radial field and IMF polarity at the sensor locations were not generally better than the lower resolution results. In both cases, the model results underestimated the magnetic field strength near 1 AU compared to observations. They acknowledged that there are still deficiencies in corona and heliospheric models that limit their ability to reproduce solar emissions and in-situ products observed by sensor systems.

4. National institute of Information and Communication Technology (NiCT), Japan

Nakamizo et al. (2009) described an MHD corona and inner heliospheric combination model. Reflecting the lack of knowledge about definitive solar coronal heating processes, they imposed an exponentially decaying function as source terms in both the thermodynamic energy and momentum equations. This was an attempt to accelerate radial flow of plasma in the solar wind from within the sub-Alfvénic regime of the corona. The source functions were constrained by the shape and orientation of the coronal magnetic field. The authors claimed that the simulations by the model reproduced many of the major characteristics of the physics of the magnetic field and solar wind in the corona, including realistic temperature distributions, streamers and coronal holes and attendant closed and open field lines respectively. They also maintained that representative solar wind streams and magnetic field sectors were produced.

Nakamizo et al. (2009) review the utility of the PFSS model to establish the magnetic flux distribution on a source surface in the corona. They described the concept of a magnetic expansion factor and its inverse relationship with solar wind flow outward from the Sun. Empirical relationships have been established and used to provide initial conditions on spherical surfaces in the corona for solar wind model integrations. They then reviewed the role of MHD models in simulating plasma density, temperature and motion in the corona and inner heliosphere. Though they conceded that the polytropic MHD models have produced reasonable features of the corona, they emphasized a need for a physical treatment of the mechanisms for plasma acceleration. High temperatures at the coronal base causes favorable thermal convection effects to create significant plasma outflows as the pressure gradient force exceeds gravitation. Yet there is a general agreement that an additional impulsive force must be exerted to account for the solar winds evidenced in the inner heliopshere. These effects are usually attributed to as yet unknown momentum or energy mechanisms in the corona. One such possible accelerating force is the possible of corona heating by means of the Alfvén wave dissipation. One type of related parameterizations to approximate this effect was the Wentzel-Kramers-Brillouin (WKB) formulation. Upon imposing this approximation, modelers were able to reproduce more accurately high- and low-speed plasma motion regions and associated plasma distributions. In this paper, the authors advocated for the addition of parametric source functions in the thermodynamic energy and/or the momentum equations. One of the most popular formulation is a volumetric heating function included as a term in the energy equation in the form of exponential decay as a function of radial distance. Another term added is thermal conduction, which releases heat down the thermal gradient to avoid overheating of closed magnetic field line regions. They argued that the upper chromosphere should be included in the domain of the corona model to properly account for the inner boundary values due to radiative losses, thermal conduction, and heating in this transition region. The overall model domain has had to be extended to the portion of space occupied by satellite sensors for output validation. In doing so, some of the models invoked the polytropic assumption more readily at greater distances from the Sun.

The goal of this work was to demonstrate an MHD model that could predict solar wind conditions near the Earth based on the photospheric magnetic field. In addition to model formulations similar to others described above, they describe of the use of photospheric magnetograms to provide inner boundary values, and the terms introduced into the momentum and thermodynamic energy equations to produce the desired plasma acceleration effects and realistic solar wind speeds at L1. Here we focus on a brief description of these two methods.

Boundary conditions were specified for the magnetic field and plasma velocity components on the inner and outer boundaries of the model domain. In addition, boundary

values were fixed for the scalar quantities of mass density and total energy density at the inner boundary. Only the boundary values of the radial component of the magnetic field were specified from observations, a selected photospheric magnetogram for a selected Carrington rotation. The values required to initiate model integration on the computational grid were set as follows: mass density and pressure were a function of radial dependent only according to hydrostatic balance, the magnetic field vector was a potential field through a conjugate residual method applied to the photospheric magnetogram, and the plasma velocity vector was set to zero everywhere. The model was then integrated to a steady-state solution, which they estimated to require over 17 days of simulated time.

The authors explain that thermodynamic processes in MHD equations can be prescribed in two ways as has been discussed above. The MHD equation system is usually closed by means of introducing the equation of state, in the form $p = \alpha\rho^n$ associated with the plasma where α is a constant of fluid elements, where n is the polytropic index. In the adiabatic assumption (in which no addition of heat is gained or lost locally), n is the ratio γ of the specific heats of constant pressure and volume of the particles (in this case, the plasma). This is the same as assuming ideal MHD equations as mentioned earlier, in which no source terms are introduced to the standard conservation equations. This amounts to representing thermodynamical processes approximately by prescribing values of γ in domains of interest, since no external sources are imposed. As an alternative, and what is described in this article, a set ratio of constant heat γ is set throughout the model realm from the photosphere to near-Earth (here as 5/3 to represent monatomic particles), and momentum and energy source terms can be introduced into the relevant equations to represent diabatic plasma processes.

The energy source term consisted of a set of volumetric heating functions made up of two contributions. First, a simple exponential of the radial distance involved a specified heating intensity and decay length. Second, a thermal conduction term of the so-called Spritzer type was a function of the local gradient of temperature and the magnetic field magnitude. The heating intensity in the exponential decay term was inversely related to the magnetic expansion factor based on the understanding of the expansion factor's inverse relationship with plasma speed. Their momentum source term was also written as a decaying function of radial distance, which also has an intensity and decay length. As with the heating function, the momentum term intensity is also inversely proportional to the expansion factor. Both intensity term proportionality constants and the constant decaying lengths were specified.

In their single Carrington rotation experiment, the authors found that the steady-state solution represented many of the actual features of the corona and the inner heliosphere. Their coronal simulation reproduced the major size and shapes of the observed coronal holes and associated solar wind streams. The solar wind speed and IMF polarity values produced by the model agreed fairly well with in-situ measurements at L1, though differences were noted. They concluded that the model as formulated would serve well as an operational solar wind and IMF model to represent both the corona and inner heliospheric conditions.

5. Solar-Interplanetary Adaptive Mesh Refinement Space-Time Conservation Element and Solution Element (SIP-AMR-CESE)

Feng et al. (2010) presented the SIP-AMR-CESE MHD model in an attempt to realistically simulate the solar wind evolution. Their formulation left two parameters to be specified in the conservation of momentum and thermodynamic energy equations respectively.

These were the so-called momentum source term and the volumetric heating function. In the light of the debate of the important processes involving coronal heating and plasma acceleration, they acknowledged that no definite modeling formulation of the energy transfer process in the heliosphere existed. They then followed Nakamizo et al. (2009) in prescribing empirical parameterizations for the volumetric heating function and momentum source terms. Both were a radial distance decay formulation, where the coefficents depended on the magnetic field expansion factor (the rate of decrease of radial magnetic field with distance from the photosphere) and the angular separation distance between an open magnetic field location and a coronal hole boundary. They attempted to tie these two parameterizations to the magnetic field topology in the current coronal configuration. They determined expansion factor and angular separation on a 2.5 R_s source surface by means of a PFSS model. The expansion factor was a function of the photospheric and source surface radial magnetic field ratios between the two surfaces. The angular separation was the minimum distance between open field lines and the nearest coronal hole boundary also in this realm. Outside the source surface, they used the source surface values.

In addition to their computational grid and numerical schemes, they also mentioned the boundary values and their initial values imposed in their experiments. On the inner boundary at the photosphere, they borrow a method of Hayashi (2005, 2006) to prescribe values based on a fixed radial magnetic field along with three cases of plasma outflow: less than the observed average (fixed temperature and density), no plasma flux (in closed magnetic field regions), and a limited mass flux greater than the observed average (in coronal hole regions). Again, observations from the Ulysses mission served as the constraints. The initial inner boundary magnetic field values were supplied by a Carrington rotation magnetogram based on line-of-sight magnetic field magnitude observations by telescope. This was used to compute a potential magnetic field as initial conditions on the computational grid. Parker's standard solar wind flow (Parker, 1963) was prescribed at the computation grid points as initial values for the plasma density, pressure and velocity. The inner boundary temperature and number density were fixed at selected constant values. At the upper boundary, they used the method of projected characteristics explained by Wu et al. (2006) to dictate the boundary condition. The model was executed until a steady-state solution was achieved.

Feng et al. (2012) used the same model and the same boundary conditions as their Feng et al. (2010) article. They added a lot more detail about their model computational formulation. In this more recent article, they used magnetograms from four separate Carrington rotations to provide initial values for the magnetic field in the computational grid through the potential field model. These four Carrington rotations represented four different phases of Solar Cycles 23 and 24. In their conclusions, they conceded that most of the actual features of the corona and heliosphere were largely dictated by the selected photospheric magnetic fields. But they found that there were a number of simulation deficiencies in their results as well. They admitted that their imposed source terms in the thermodynamic energy and momentum equations did not bring about realism in the coronal heating and the acceleration of the solar wind in the corona. They speculated that accounting for different properties of the ions and electrons in the plasma may improve the simulated solar wind properties. But they acknowledged that only a physically representative formulation for the actual coronal heating and plasma acceleration mechanism can truly bring about the real solar wind properties. Though they mentioned the uncertainties caused by line-of-sight magnetograms or inner boundary values in the magnetic field, their model was able to simulate properly the locations of the coronal holes as compared with observed imagery.

But the model predicted magnetic field strength at 1 AU tended to be significantly too small, as with other model products. They felt that the use of a potential field approximation to begin the simulation may be contributing to this deficit, in that it can't represent the increased magnetic field strength associated with solar active regions.

6. Coupled SWMF SC and IH

Because the Space Weather Modeling Framework (SWMF) was devised to couple space weather model components, a significant amount of time will not be committed to this formulation here. However, a couple of more recent articles that represent the SWMF effort did propose alternative methods of attempt to address the thorny issue of plasma acceleration in the corona. First, van der Holst et al. (2010) introduced separate ion and electron properties in their model, allowing for collisions among them and the thermal heat conduction of the electrons. They proposed the heating of the ions through the turbulence dissipation of the Alfvén waves in open magnetic field line areas. The Alfvén wave energy density was determined at the inner boundary through the use a potential field source surface formulation. Inner boundary temperature and density were obtained from differential emission measurements. Their formulation still was left with several tunable parameters that were difficult to determine definitively. Second, Evans et al. (2012) attempted another method of deriving plasma acceleration from Alfvén wave energy. In their formulation, the Alfvén wave pressure gradient imposed an acceleration of the plasma, while the wave dissipation heated it. In addition to the wave dissipation imposed by van der Holst et al. (2010), they added another dissipation mechanism that they called surface Alfvén wave damping. Their model results showed the temperature distributions most like those observed when both Alvénic turbulence dissipation and surface Alfvén wave damping were considered. In addition, such a model produced a background plasma flow that more effectively resulted in CME-driven shocks.

F. Summary and Recommendations

The history of modeling the behavior of the solar plasma properties and the attendant magnetic field in the solar corona and the inner heliosphere has been a relatively new endeavor. Beginning in the early 1970s, it was enhanced by the satellite missions that provided measurements and imagery that provided new insights of the effluent that travels outward from the Sun continually. As we realized the important role of these ambient conditions in phenomena characterized as space weather events, it was increasingly realized that accurate simulations of the solar wind and interplanetary magnetic field conditions was essential. Magnetohydrodynamics was a natural discipline to apply to this realm, and a sequence of such models were formulated to account for these properties. Ultimately, it was realized that the characteristics of the sub-Alfvén wave speed plasma flow near the Sun was fundamentally different from the super-Alvénic flows farther out in the inner heliosphere. This led to devising companion models to represent these separable domains, which of course required the need to link them computationally. The inner corona models have proven to be a more difficult challenge, in that the problem of understanding the fundamental physics causing the significant plasma outflow acceleration and the associated plasma heating was elusive. The problem yet remains, and solar physicists have continually posed new model formulations to address it. At this time, the most popular mechanism that explains the heating and acceleration is the energy

dissipation of the Alfvén waves themselves. Yet no fully suitable physical formulation has been devised for their contribution, and partially based on this shortfall and the deficiencies of proper measurements to provide boundary and initial values, both solar wind and magnetic field simulations depart from observations near the Earth.

At this point, the best that can be gained from existing corona and heliosphere models is the vast experience invested in their development, execution and evaluation. In spite of their shortcomings, these models provide the basic building blocks for future improvement in the simulation of corona and heliospheric conditions. It is recommended that current corona and heliospheric models, that have matured through substantial use in demonstrating realistic properties of the solar plasma and magnetic field in the realm between the Sun and the Earth, be drawn upon as a starting point for further research. As more is known about the solar environment, they may incorporate more fully the physical mechanisms that bring about more realistic simulations that evidence our greater knowledge of the solar-terrestrial environment.

G. References

Altschuler, M. D., and G. Newkirk, Jr. (1969), Magnetic fields and the structure of the solar corona. I: Methods of calculating coronal fields, *Solar Phys.*, **9**, 131-149, doi:10.1007/BF00145734.

Arge, C. N., and V. J. Pizzo (2000), Improvement in the prediction of solar wind conditions using near-real time solar magnetic field updates, *J. Geophys. Res.*, **105**, A5, 10,465-10,480, doi:10.1029/1999JA900262.

Arge, C. N., J. G. Luhmann, D. Odstrcil, C. J. Schrijver and Y. Li (2004), Stream structure and coronal sources of the solar wind during the May 12th, 1997 CME, *J. Atmos. Sol. Terr. Phys.*, **66**, 1295-1309, doi:10.1016/j.jastp.2004.03.018.

Bogdan, T. J., and B. C. Low (1986), The three-dimensional structure of magnetostatic atmospheres. II. Modeling the large-scale corona, *Astrophys. J.*, **306**, 271-283, doi:10.1086/164341.

Contopoulos, I., C. Kalapotharakos, and M. K. Georgoulis (2011), Nonlinear force-free reconstruction of the global solar magnetic field: Methodology, *Solar Phys.*, **269**, 351-365, doi:10.1007/s11207-011-9713-x.

Downs, C., I. I. Roussev, B. van der Holst, N. Lugaz, I. V. Sokolov, and T. I. Gombosi (2010), Toward a realistic thermodynamic magnetohydrodynamic model of the global solar corona, *Astrophys. J.*, **712**, 1219-1231, doi:10.1088/0004-637X/712/2/1219.

Evans, R. M., M. Opher, R. Oran, B. van der Holst, I. V. Sokolov, R. Frazin, T. I. Gombosi, and A. Vásquez (2012), Coronal heating by surface Alfvén wave damping: Implementation in a global magnetohydrodynamics model of the solar wind, *Astrophys. J.*, **756**, 155-167, doi:10.1088/0004-637X/756/2/155.

Feng, X., L. Yang, C. Xiang, S.T. Wu, Y. Zhou, and D. Zhong (2010), Three-dimensional solar wind modeling from the Sun to Earth by a SIP-CESE MHD model with a six-component grid, *Astrophys. J.,* **723**, 300-319, doi:10.1088/0004-637X/723/1/300.

Fry, C. D., W. Sun, C. S. Deehr, M. Dryer, Z. Smith, S.-I. Akasofu, M. Tokumaru, and M. Kojima (2001), Improvements to the HAF solar wind model for space weather predictions, *J. Geophys. Res.*, **106**, A10, 20,985-21,001, doi:10.1029/2000JA000220.

Gombosi, T. I., G. Tóth, D. L. De Zeeuw, K. G. Powell, and Q. F. Stout (2001), Adaptive mesh refinement MHD for global simulations, *Proceedings of ISSS-6*, J. Büchner, C. T. Dum, and M. Scholer, eds., Copernicus Gesellschaft, 1-8.

Groth, C. P. T., D. L. De Zeeuw, T. I. Gombosi, and T. I. Gombosi (2000), Global three-dimensional MHD simulation of a space weather event: CME formation, interplanetary propagation, and interaction with the magnetosphere, J. Geophys. Res., 105, A11, 25053-25078, doi:10.1029/2000JA900093.

Hayashi, K. (2005), Magnetohydrodynamic simulations of the solar corona and solar wind using a boundary treatment to limit solar wind mass flux, *Astrophys. J. Supp.*, **161**, 480-494, doi:10.1086/491791.

Hayashi, K. (2006), Three-dimensional time-dependent MHD simulation model of the solar corona and solar wind, In *Solar Influence on the Heliosphere and Earth's Environment: Recent Progress and Prospects*, N. Gopalswamy and A. Bhattacharyya, eds., Proceedings of the International Living with a Star Workshop 2006, Goa, India, February 19-24, 2006.

Hayashi, K. (2012), An MHD simulation model of time-dependent co-rotating solar wind, *J. Geophys. Res.*, **117**, A08105, doi:10.1029/2011JA017490.

Linker, J. A., Z. Mikić, D. A. Biesecker, R. J. Forsyth, S. E. Gibson, A. J. Lazarus, A. Lecinski, P. Riley, A. Szabo, and B. J. Thompson (1999), Magnetohydrodynamic modeling of the solar corona during Whole Sun Month, *J. Geophys. Res.*, **104**, A5, 9809–9830, doi:10.1029/1998JA900159.

Lionello, R., J. A. Linker, and Z. Mikić (2001), Including the transition region in models of the large-scale solar corona, *Astrophys. J.*, **546**, 542-551, doi:10.1086/318254.

Lionello, R., J. A. Linker, and Z. Mikić (2009), Multispectral emission of the sun during the First Whole Sun month: Magnetohydrodynamic simulations, *Astrophys. J.*, **690**, 902-912, doi:10.1088/0004-637X/690/1/902.

Luhmann, J. G., S. C. Soloman, J. A. Linker, J. G. Lyon, Z. Mikic, D. Odstrcil, W. Wang, and M. Wiltberger (2004), Coupled model simulation of a Sun-to-Earth space weather event, *J. Atmos. Sol. Terr. Phys.*, **66,** 1243-1256, doi:10.1016/j.jastp.2004.04.005.

Mackay, D. H., and A. A. van Ballegooijen (2006), Models of the large-scale corona. I. Formation, evolution, and liftoff of magnetic flux ropes, *Astrophys. J.*, **641**, 577-589, doi:10.1086/500425.

Mackay, D. H., and A. R. Yeates (2012), The Sun's global photospheric and coronal magnetic fields: observations and models, *Living Rev. Solar Phys.*, **9**, http://www.livingreviews.org/lrsp-2012-6.

Mikić, Z., J. A. Linker, D. D. Schnack, R. Lionello, and A. Tarditi (1999), Magnetohydrodynamic modeling of the global solar corona, *Phys. Plasma*, **6**, 2217-2224, doi: 10.1063/1.873474.

Norquist, D. C. (2013), Forecast performance assessment of a kinematic and a magnetohydrodynamic solar wind model, *Space Weather*, **11**, 17-33, doi:10.1029/2012SW000853.

Nakamizo, A., T. Tanaka, Y. Kubo, S. Kamei, H. Shimazu, and H. Shinagawa (2009), Development of the 3-D MHD model of the solar corona-solar wind combining system, *J. Geophys. Res.*, **114**, A07109, doi:10.1029/2008JA013844.

Odstrcil, D., and V. J. Pizzo (1999), Distortion of the interplanetary magnetic field by three-dimensional propagation of coronal mass ejections in a structured solar wind, *J. Geophys. Res.*, **104**, 28,225-28,239, doi:10.1029/1999JA900319.

Odstrcil, D. (2003), Modeling 3-D solar wind structures, *Adv. Space Res.*, **32**, 497-506, doi:10.1016/S0273-1177(03)00332-6.

Odstrcil, D., V. Pizzo, J. A. Linker, P. Riley, R. Lionello, and Z. Mikic (2004), Initial coupling of coronal and heliospheric numerical magnetohydrodynamic codes, *J. Atmos. Sol. Terr. Phys.*, **66**, 1311-1320, doi:10.1016/j.jastp.2004.04.007.

Ofman, L. (2010), Wave modeling of the solar wind, *Living Rev. Solar Phys.*, **7**, http://www.livingreviews.org/lrsp-2010-4.

Owens, M. J., H. E. Spence, S. McGregor, W. J. Hughes, J. M. Quinn, C. N. Arge, P. Riley, J. Linker, and D. Odstrcil (2008), Metrics for solar wind prediction models: Comparison of empirical, hybrid, and physics-based schemes with 8 years of L1 observations, *Space Weather*, **6**, S08001, doi: 10.1029/2007SW000380.

Parker, E. N. (1963), *Interplanetary Dynamical Processes*, Interscience Publishers, Berkeley, CA, 272 pp.

Powell, K. G., P. L. Roe, T. J. Linde, T. I. Gombosi, and D. L. De Zeeuw (1999), A solution-adaptive upwind scheme for ideal magnetohydrodynamics, *J. Comput. Phys.*, **154**, 284-309, doi:10.1006/jcph.1999.6299.

Riley, P., R. Lionello, J. A. Linker, Z. Mikić, J. Luhmann, and J. Wijaya (2011), Global MHD modeling of the solar corona and inner heliosphere for the Whole Heliosphere Interval, *Solar Phys.*, **274**, 361-377, doi:10.1007/s11207-010-9698-x.

Roussev, I. I., T. I. Gombosi, I. V. Sokolov, M. Velli, W. Manchester, D. L. De Zeeuw, P. Liewer, G. Tóth, and J. Luhmann (2003), A three-dimensional model of the solar wind incorporating solar magnetogram observations, *Astrophys. J.*, **595**, L57-L61, doi:10.1086/378878.

Schatten, K. H., J. M. Wilcox, and N. F. Ness (1969), A model of interplanetary and coronal magnetic fields, *Solar Phys.*, **6**, 442-455, doi:10.1007/BF00146478.

Schatten, K. H. (1971), Current sheet magnetic model for the solar corona, *Cosmic Electrodyn.*, **2**, 232-245.

Sokolov, I. V., B. van der Holst, R. Oran, C. Downs, I. I. Roussev, M. Jin, W. B. Manchester, R. M. Evans, and T. I. Gombosi (2013), Magnetohydrodynamic waves and coronal heating: unifying empirical and MHD turbulence models, *Astrophys. J.*, **764**, 23-35, doi:10.1088/0004-637X/764/1/23.

Tóth, G., and co-authors (2005), Space Weather Modeling Framework: A new tool for the space science community, *J. Geophys. Res.*, **110**, A12226, doi:10.1029/2005JA011126.

van Der Holst, B., W. B. Manchester, R. A. Frazin, A. M. Vasquez, G. Toth, and T. I. Gombosi (2010), A data-driven, two-temperature solar wind model with Alfvén waves, *Astrophys. J.*, **725**, 1373-1383, doi:10.1088/0004-637X/725/1/1373.

Vásquez, A. M., R. A. Frazin, K. Hayashi, I. V. Sokolov, O. Cohen, W. B. Manchester, and F. Kamalabadi (2008), Validation of two MHD models of the solar corona with rotational tomography, *Astrophys. J.*, **682**, 1328-1337, doi: 10.1086/589682.

Wiegelmann, T. (2007), Computing nonlinear force-free coronal magnetic fields in spherical geometry, *Solar Phys.*, **240**, 227-239, doi: 10.1007/s11207-006-0266-3.

Wu, S. T., A. H. Wang, Y. Liu, and J. T. Hoeksema (2006), Data-driven magnetohydrodynamic model for active region evolution, *Astrophys. J.*, **652**, 800-811, doi:10.1086/507864.

Yang, L. P., X. S. Feng, C. Q. Xiang, Y. Liu, X. Zhao, and S. T. Wu (2012), Time-dependent MHD modeling of the global solar corona for year 2007: Driven by daily-updated magnetic field synoptic data, *J. Geophys. Res.*, **117**, A08110, doi:10.1029/2011JA017494.

Yeates, A. R., D. H. Mackay, and A. A. van Ballegooijen (2007), Modeling the global solar corona: Filament chirality observations and surface simulations, *Solar Phys.*, **245**, 87-107, doi:10.1007/s11207-007-9013-7.

Zhao, X., and J. T. Hoeksema (1994), A coronal magnetic field model with horizontal volume and sheet currents, *Solar Phys.*, **151**, 91-105, doi:10.1007/BF00654084.

APPENDIX B

Details of the Space Weather Modeling Framework
Solar Corona and Inner Heliosphere Models

A. Introduction

The Space Weather Modeling Framework (SWMF) is a system of magnetohydrodynamic models that simulate the behavior of the solar wind, interplanetary magnetic field (IMF), and their effects on near-Earth space environment. According to an introduction article on the SWMF by Tóth et al. (2005), the system comprises the physical domains that include the solar corona, inner heliosphere, the Earth's magnetosphere, radiation belt, ionosphere and thermosphere. The collection of models is designed to accomplish "physics-based space weather simulations" and "space physics applications." Each physical domain's model is seen as a component of the overall system, which could either be used as is or replace with an alternative formulation. The components are executed from a control module. They provide a "toolkit" to permit coupling between the components representing contiguous domains. Such coupled components may be run in sequence among them, or may be run simultaneously. The components are designed to be executed efficiently on multi-processor computers. SWMF as a system is available to the public for experimentation by the scientific community. Tóth et al. (2005) presents a brief explanation of the SWMF components, whereas their basis are in earlier reports and experiences with them have been published since this time.

Tóth et al. (2005) explain that the solar corona model produces information that can be used as input for the inner heliosphere model. These are the two components that we discuss in this report. Tóth et al. (2005) promoted the concept of modular components that could be linked together rather than a single model that comprised all of the individual domains that the authors felt were inflexible. By addressing different model formulations in each component, they could recognize and more efficiently handle what they felt were fundamental physics in the separate domains. In fact, that same modular approach was championed by the Center for Integrated Space Weather Modeling (CISM), whose scientists produced a number of articles that reflected that philosophy. It appears that the SWMF effort did not intersect with CISM during its existence, thus this modular approach was embraced by two independent space weather research groups.

The solar corona (SC) model in the SWMF has its roots in models developed by Groth et al. (2000) focusing on the physical aspects and Gombosi et al. (2001) that concentrated on the computational formulation. The SWMF SC component originally extended between 1 and 24 R_s radially. It follows the computational structure of the Block Adaptive-Tree Solar-wind Roe-type Upwind Scheme (BATS-R-US) devised by Powell et al. (1999) and Gombosi et al. (2001). Briefly, the governing equations are integrated forward in time to obtain grid volume average values in rectangular Cartesian grid cells. It organizes computational cells in blocks of equal sized volumes occupying separate volumes of physical space. The adaptive computational grid was originally designed to resolve phenomena on varying spatial scales, including plasma disturbances like coronal mass ejections. The local grid spacing adapts both up and down scale to the size of the motions within the blocks, directed by physics-based refinement criteria.

Groth et al. (2000) originated the algorithms included as source terms in the SC thermodynamic energy equation with an intent to account for net coronal heating and the

consequent outward plasma acceleration. An empirical energy exchange term they called a volumetric heating function allowed diabatic plasma compression and expansion assuming a ratio of specific heats $\gamma = 5/3$. The goal was to include heat flux, thermal conduction and radiative loss processes in the corona. This was done by including a formulation that simulated local energy deposition and losses. The imposed heat source was latitudinally dependent and decreased with radial distance. They used a number of parameters that were designed to optimize the performance of the solar wind speeds near 1 AU.

According to Tóth et al. (2005), the SC component of that time allowed for specifying inner boundary values at 1 R_s in temperature and mass density to vary with latitude and longitude. The radial component of the magnetic field could be specified from a photospheric magnetogram or from a simple dipole. They determine the solar wind radial speed boundary condition at the outer boundary of SC to be super-Alfvénic speed to prohibit return flow. An exception can be during the passage of a heliospheric transient, when it may become sub-Alfvénic.

The SC component supplies the plasma variables as an inner boundary condition (initial and continuing) to the Inner Heliosphere (IH) component. The SC-IH component coupling allows the plasma and magnetic field parameters to be passed between the two modules through an overlapping grid. This overlap can prevent reflections or numerical artifacts occurring on the IH grid, especially during slower flow from unaligned grids and time steps among the components. The domain of the IH component may extend from about 20 R_s out to beyond 1 AU. The physical formulation of the IH component is simpler than the SC, assuming polytropic plasma compression and expansion.

B. More Recent Research with the SC and IH

Downs et al. (2010) experimented with the effects of coronal heating, heat conduction and radiative cooling in the thermodynamic energy equation of the SC. In one experiment, a prescribed function of the photospheric magnetic field magnitude was used to allocate solar heating into any location of the corona. Its total contribution depended on the integration of the unsigned magnetic flux at 1 R_s, which was the photospheric magnetogram serving as the inner boundary values. In another, a heating function in the form of a negative exponential of radial distance was imposed. Photospheric magnetograms provided inner boundary values of the radial magnetic field. They were extended onto the SC computational grid as initial values using the potential field source surface (PFSS) model. From the initial magnetic field lines, more limited exponential heating was applied to computational elements in regions of open field lines. A stronger heating source from both the function of the photosphere's magnetic field and the full exponential heating was put in effect into the grid points in areas of the closed lines. While they didn't physically attribute these imposed heating sources to Alfvén wave turbulence dissipation, they acknowledged that this phenomenon may be a major real source of the coronal heating. But their focus is on the low corona where they assumed the Alfvén wave pressure was much less than the thermal pressure. They imposed different boundary value formulations in two ways. The primary method fixed the lower boundary at a set uniform temperature and density characteristic of the chromosphere. It allowed broadening of the transition region between the chromosphere and the corona so that the model resolved it fully. In the alternate method called a radiative energy balance, a base temperature was set to a greater value of the high transition region and assumed a heat balance from this level to the top of the chromosphere. They

integrated the rearranged thermodynamic energy equation over temperature from chromosphere to high transition region levels at constant pressure to determine boundary value density in terms of heat conduction, coronal heating and radiative cooling. The resulting base density varied spatially along the boundary.

Synthetic emission intensity images were developed from the resulting model steady state solutions and were compared with observed imagery at distinct wavelengths. Both versions of the lower boundary value methods were able to reproduce the major features of the quiet Sun corona. The simpler chromospheric lower boundary case was more efficient computationally, because it did not include model computations for the transition region. But the radiative energy balance produced a smoother emission structure and somewhat higher temperatures. The photospheric magnetic field-based heating source formulation did result in more realistic coronal emission imagery, especially near coronal holes and active regions, than the exponential decay method. But the latter was able to produce a reasonable emission representation away from these features. The authors came to the conclusion that greater complexity in formulating coronal heating terms may not be as beneficial as representing their actual physical basis.

van der Holst et al. (2010) also addressed the association between heating in the corona and acceleration of the plasma, resulting in realistic solar wind speeds in the inner heliosphere. They developed a solar corona component model for the SWMF that solved separately for the electron and proton temperatures in accounting for different collision processes. They applied heat conduction to the electrons, and heating of the protons due to Alfvén wave turbulence dissipation. This required two thermodynamic energy equations for the two types of particles of the plasma, so that proton and electron pressure and temperature were represented, but a single velocity represented both and they were assumed to have equal number densities. The collisional heat transfer between the protons and electrons was only maintained close to the Sun, within 5 R_s. They used a collisional form of heat conduction for the electrons also in this domain, that was smoothly diminished to zero between 5 and 10 R_s.

They attributed proton heating and acceleration to the presence of Alfvén waves. They introduced an additional equation for the tendency of Alfvén wave energy density in which the Alfvén wave pressure was half the wave energy density and the Alfvén speed is dependent on the magnetic field vector and the scalar mass density. Alfvén waves can be directed outward or inward. They used the Kolmogorov dissipation of the Alfvén waves to heat the protons, which was a function of the Alfvén wave energy density, scalar magnetic field magnitude and the mass density. In their formulation, they only included Alfvén waves propagating away from the Sun without reflection, even though Kolmogorov dissipation depends on returning waves. They explained this by stating that Kolmogorov overestimates coronal heating, so since the partition of heating between protons and electrons was still uncertain, no electron heating was included in the model.

In the boundary values, they fixed the mass density and the electron temperature obtained from extreme ultraviolet imagery using a method known as differential emission measure tomography. They used the PFSS model to set the initial magnetic field radial component in the corona, and the tangential components were set to their photospheric values at all radial distances. The proton temperatures were extrapolated outward as initial values based on pressure balance in the corona. The Alfvén wave energy density was set to zero on the inner boundary at locations of closed field lines. In regions of open field lines the specified Alfvén wave energy density was from an empirical solar wind speed estimated at 1 AU based on the magnetic expansion factor and the distance to the nearest coronal hole boundary in the PFSS solution.

They explained that in their model, the Alfvén waves propagate away from the Sun. Given the establishment of the Alfvén wave energy density at the inner boundaries as described above, the waves only propagated from the open field line areas according to the PFSS model. This means that the open field line areas would remain open in the model solution, and the closed field line regions should remained closed.

The authors mentioned that earlier versions of the SWMF solar corona (SC) component used a spatially varying adiabatic index γ to account for coronal heating and plasma acceleration. A later version derived a γ in the SC and set a uniform γ that was reduced in the inner heliosphere (IH) component. The version of SC and IH referenced in van der Holst et al. (2010) could be selected in the SWMF and used the fixed value of $\gamma = 5/3$. The computational grid consisted of a cube from -24 R_s to 24 R_s in all three Cartesian coordinates from about 16,000 km grid cells near the Sun increasing to 525,000 km at the outer boundary. Using their adaptive mesh refinement solution method, they typically used about 2.5 million grid cells. They provided initial values on the computational grid using the Parker hydrodynamic and isothermal solar wind for plasma velocity and the PFSS solution as mentioned from a selected Carrington rotation magnetogram.

The IH component used in this experiment extended from -250 R_s to 250 R_s in all three Cartesian coordinates, with an inner boundary of 16 R_s. It used the SC model output in the overlapping grid cells as the IH inner boundary conditions. Its grid cells extended from 343,000 km in the innermost grids to 2.73 million km at the outermost grids, utilizing a total of about 11.2 million grid cells.

They conducted their experiment using the GONG magnetograms comprising the Carrington rotation 2077 corresponding to late 2008, a time very near solar minimum. As with other experiments, the major features of the corona such as the plasma velocity and temperature distribution were reproduced well. However, the solar wind speed and temperature in comparison to in-situ observations at L1 were too small, as was the magnetic field magnitude. This was especially true of periods of observed fast wind speeds. The authors felt that including the inflowing Alfvén waves might improve the plasma heating and acceleration in the corona. They blamed the insufficient magnetic field simulations on weakness in the strength of the photospheric magnetograms forming the inner boundary, especially near the poles.

Evans et al. (2012) made yet another attempt to simulate realistic corona heating and plasma acceleration in the context of the SWMF corona component. Like van der Holst et al. (2010), they associated Alfvén wave pressure with acceleration and Alfvén wave dissipation heating the plasma. However, in addition to the dissipation, they introduced what they referred to as surface Alfvén wave damping in areas where transverse gradients of the Alfvén speed are great. They state that those conditions can occur in regions when dissipation is weak, such as in lower latitudes and near boundaries of open and closed field lines. In this case, they claim that the damping can result in significant plasma heating as can dissipation.

They constructed the wave dissipation and wave damping mechanisms in the form of what they called Alfvén wave energy dissipation rates. They did not explicitly model the dissipative process, but assumed that all of the wave dissipation led to plasma heating. The formulation they proposed for the wave energy dissipation rate due to the surface Alfvén wave damping process was implemented as a term in the coronal model. It took the form of a ratio of the wave group velocity magnitude and a length scale, the latter of which was a ratio of the mass density and its gradient in the plane perpendicular to the wave polarization divided by the wave frequency and controlled by a damping strength parameter. The wave energy dissipation rate

from surface Alfvén wave damping was computed in each grid cell and it assumed that all waves were dissipated at each model time step. Heating was contributed to the model as a term in the thermodynamic equation. In the case of wave energy dissipation rate due to Kolmogorov wave dissipation, it was assumed to be proportional to the wave energy density times the magnetic field magnitude divided by the mass density. It also was controlled by a dissipation strength parameter. The term contributed heating through wave dissipation in the thermodynamic equation. The latter formulation was used also by van der Holst et al. (2010).

Including the additional damping factor in the SWMF SC thermodynamic equation and the corresponding pressure wave acceleration contributions of the wave pressure in the momentum equation, Evans et al. (2012) repeated the experiment of van der Holst et al. (2010) of Carrington rotation 2077. The initial and boundary values were applied in the same manner. As in the case of van der Holst et al. (2010), they did not consider Sun-directed waves. They conducted three experiments, in which a Kolmogorov-like Alfvén wave dissipation and a surface Alfvén wave damping mechanism were employed separately in two of them, and in one they were employed together. In all three experiments, the damping mechanism parameters were set to obtain a maximum fast solar wind speed of 750 km s^{-1} at 0.1 AU. Since their focus is on the coronal heating, they limited the computational domain to $\pm$ 24 R_s in all three Cartesian dimensions. The smallest computational grid size was about 16,400 km on a side at the inner boundary, and they applied grid cells four times that size to the heliospheric current sheet area. The computational grid encompassed approximately 2.4 million grid cells in all.

They examined the results of the heating rate distribution in the corona, as well as the steady state temperature at 0.1 AU. The surface Alfvén wave damping heating dominated in mid-latitudes where they deemed the density gradients along open magnetic field lines was greatest. They were also significant along open and closed field line boundaries and similarly along the heliospheric current sheet. The Kolomgorov wave dissipation produced the greatest heating in the polar latitudes where the magnetic field and the wave energy density was largest. They felt the experiment combining both effects produced the most realistic coronal temperature distribution.

Sokolov et al. (2013) incorporated Alfvén wave turbulence and its dissipation in the SWMF solar corona model. They credited the dissipated wave turbulence to be the only necessary source of heating and consequent plasma acceleration in the corona. They began their paper by arguing that recent observations have shown that the power of the magnetic field perturbations seen in the chromosphere is more than enough to account for corona heating and solar wind acceleration. Up to this point, modelers had introduced source terms in the thermodynamic energy and momentum equations to represent this energy in heating and accelerating the corona plasma. However, they claimed that these source terms did not stem from a physical basis, but were construed to gain better agreement with coronal imagery and in-situ measurements at 1 AU. They contrast these model formulations, which have demonstrated some success, with what they refer to as a turbulence-driven model that can actually simulate these waves. Presumably, if done so faithfully, they can plentifully produce the same or greater levels of plasma heating and accelerating energy in the lower corona and do so through the actual physical dissipation mechanism.

The authors stated that existing turbulence-driven models are unable to produce coronal heating that properly accounts for solar wind properties, especially in high speed streams associated with coronal holes. They also claimed that these models should simulate the magnitude and frequency spectrum of turbulence and the dissipation-sustaining temperature at 1

AU. To attempt these goals, this study attempted to demonstrate a parameterization of lower corona heating resulting from the dissipation of Alfvén wave turbulence. Usually, parameterization is employed when the phenomenon of interest is much smaller in spatial scale than can be resolved by the model computational grid. In their case, they formulated a parameterization based on a relationship between the total power available for coronal heating and the unsigned magnetic flux integrated over the photosphere. Assuming that Alfvén wave turbulence dissipation is the major heating source, their heating function relied on requiring an inner boundary condition on the wave energy flux (Poynting flux) entering the corona from the photosphere and a formulation of an absorption of the waves in the corona that creates the desired energy deposition distribution.

To impose the boundary condition at the photosphere, they assumed that the Poynting flux at the photosphere is proportional to the magnetic field vector magnitude. They assumed that all of the Alfvén wave turbulence moving out from the photosphere is absorbed in the coronal plasma. Given these two assumptions, the propagation of the wave energy flux along the flux tube will move outward from the solar interior where it and the magnetic field magnitude are stronger to the photosphere where they are weaker. At any point on the propagation, their ratio will be constant. The authors stated that these assumptions are in agreement with other investigators. They suggested that other modelers and EUV, X-ray and in-situ solar wind observations support the premise that the ratio of the Poynting flux and the magnetic field magnitude at the photosphere is a constant. The authors stated that the Poynting flux is not measured, but that the oscillating velocity is observed at 1.1 R_s. This makes it difficult for the observations to be converted to the boundary conditions at 1 R_s. Furthermore, it is likely that some of the wave energy is already absorbed at 1.1 R_s by the coronal plasma.

For an Alfvén wave turbulence absorption parameterization of the coronal heating, they arrived at an absorption coefficient which is the ratio of the Alvén speed and a specified absorption length. Like Evans et al. (2012), they suggested that this ratio can be included in an equation for the intensity of Alfvén waves, which can propagate in the same and opposite direction of the magnetic field vector. They stated that the absorption coefficient is wave frequency dependent, with the highest frequency waves more likely to dissipate. Also, wave-wave interaction can increase wave frequency. Therefore, as the large-scale perturbations decrease to smaller scales and higher frequencies, the wave energy is absorbed.

They chose a Kolmogorov-like Alfvén wave dissipation mechanism for the absorption coefficient, with an absorption length inversely proportional to the square root of the magnetic field magnitude, with an empirical proportionality constant. This with the choice of the Poynting flux boundary condition they claimed would allow the model to reproduce the appropriate level of coronal heating in the regions of closed field lines.

In open magnetic field line areas, they assumed that the Poynting flux is similar to that in closed field regions, but instead see a reduced wave energy dissipation rate in causing the smaller coronal heating. What is happening is that very little of the wave energy flux is being absorbed within coronal holes out to at least 2.5 R_s. This contrasts with closed fields, where virtually all of the wave turbulence is absorbed. They claimed that this is due to the much greater Alfvén wave energy of outward propagating waves than for incoming waves in open field lines. They saw this as an imbalance of wave turbulence in coronal holes, so that in the oppositely propagating waves, the wave-wave interaction is minimal. This called for a different heating rate expression for open fields of minimal wave energy density, such that a floor imposed by a reflection coefficient was included. The coefficient was set to a small ratio of the reflected wave

amplitude to the outgoing wave amplitude. They assigned a reflection coefficient as a function of the magnetic field expansion factor even though there is no known relationship between Alfvén wave turbulence absorption and the solar wind speed which was originally governed by expansion factor. They tried to fit the solar wind properties at 1 AU through the proper function of the expansion factor.

As in van der Holst et al. (2010), their model formulation had different thermodynamic energy equations for the prediction of ion and electron temperatures. However, the derived coronal heating functions were only included in the ion equation. A separate equation for the time tendency of the wave energy density for the oppositely propagating waves accounted for the wave dissipation, which was the right-hand-side. This term was the coronal heating source term in the proton thermodynamic energy equation. They took the forms assumed for closed and open field line regions, accordingly.

To solve the equations for the experiment presented, they used a Carrington rotation magnetogram to provide inner boundary values of the magnetic field. They assumed a constant Poynting flux value to represent the intensity of the outgoing Alfvén waves emitted from the photosphere. To declare the inner boundary values for density and temperature, they set them to constant values appropriate to the top of the chromosphere. They set a maximum temperature for the transition region between chromosphere and corona by increasing the electron heat conduction to extend the transition region.

They next described the role of adaptive mesh refinement in the Block Adaptive Tree Solar Wind Roe-type Upwind Scheme (BATS-R-US) model solver code for the solution of the ideal MHD equations. The advantage of this approach is to be able to vary the numerical resolution significantly in the computational domain. It permits the incorporation of fine grid scale magnetic data into the model. This has allowed modeling of the global solar corona and the inner heliosphere on the large scale, as well as active region fine structure and interplanetary transients on the smaller spatial distances. The BATS-R-US MHD code is a main module within the SWMF codes. The SWMF physical domain components can be linked together to inter-operate from the Sun's surface to the Earth's upper atmosphere. The SWMF integrations have been run on massively parallel computer systems in faster than real time.

The experiment they conducted was on Carrington rotation 2107 of early 2011 during which a solar flare, a fast CME, and a solar energetic particle event was generated. The whole Sun magnetogram was generated from observations made by the Heliospheric Magnetic Imager on the Solar Dynamics Observatory. They computed a 3-D magnetic potential field from the magnetogram as initial values using a model called Finite Difference Iterative Potential-field Solver (FDIPS) out to the full computational domain with an outer boundary at 24 R_s in all three dimensions in a spherical grid, involving 21 M cells. The smallest cells near the Sun had a size of 700 km, and the largest near the outer boundary 560,000 km. They ran the model to a steady state and produced fast solar winds at high latitudes to about 750 km s^{-1} and slower speeds at low latitudes to about 300 km s^{-1}. They compared synthetic images of the model emissions at three wavelengths with imagery from the SDO AIA imager. They were able to show some similarity between the patterns of active regions and coronal holes of the simulated and observed images.

C. The Space Weather Modeling Framework Model Access

The University of Michigan Center for Space Environment Modeling (CSEM) has a web site for SWMF at http://csem.engin.umich.edu/tools/swmf/index.php. The "Home" tab takes you

to the CSEM web site, in which it is stated that their primary purpose is to develop "high-performance, first-principles based computational models of the space environment" and to use "these models to predict 'Space Weather', to understand space mission data and to further our understanding of the solar system." Under the "Models and Tools" section on the "Home" page, they claim that "the primary focus of CSEM is developing highly accurate numerical models of the space environment using state-of-the-art numerical techniques." The next statement is important for our purposes: "We strive to make these models and results available to the community through collaborations, toolkits and analysis."

In the "Models and Tools" web page, they list four major models/algorithms: SWMF/BATSRUS, CRASH, FDIPS, and GITM. Within the introduction description of SWMF, they mention ionospheric, thermospheric, ring current, polar wind, and radiation belts models. However, for our purposes we are interested in the Solar Corona (SC) and Inner Heliospheric (IH) components of SWMF, along with any other algorithms that provide boundary and initial values for their execution. An example is the FDIPS mentioned above, which can create a potential magnetic field solution on the SC computational grid as initial values.

Clicking the SWMF/BATSRUS link takes you to the "SWMF Home web page." A short explanation of space weather is presented in the "About" section, in which is stated that space weather refers to the conditions in the domains from the Sun to the Earth's thermosphere that can impact technological systems and thus interrupt human activities. A knowledge of fundamental physical processes of space weather is stressed, and first-principle numerical models are stated as a necessary part of providing advanced warning of space weather events. CSEM strives to develop and demonstrate such space weather models through the experience of their research personnel. The intention is that the SWMF modeling suite is available as a common operating system, in which its various components provide the user with control over how they can be executed and interact with each other.

On the SWMF Home web page, the other sections listed are "Downloads", "Documentation", "Citing SWMF", "SWMF Validation" (currently disabled), and "SWMF Support." Going first to the Downloads section, four explanatory or action sub-sections are listed: "Requirements", "Limitations", "Register", and "Download SWMF." Under the Requirements sub-section, they list four computational environments that must be present for SWMF to be used: UNIX (such as Linux) or MacOSX operating system; FORTRAN 90 compiler; a Message Passing Interface (MPI) library installation; a Perl interpreter. It is strongly recommended that the SWMF model components be executed on a parallel (multi-processor) computer architecture. In the Limitations and License sub-section, SWMF is stated as being a prototype model of the Sun-Earth system, considered preliminary in its maturity, and should be used in close collaboration with CSEM. The four-page license is presented for printing, and the prospective model user is asked to carefully read it, sign the last page, and send the completed page to CSEM. In the license, the user is prohibited from distributing or discussing the code to/with anyone. No aspect of the SWMF performance is to be communicated with anyone without receiving permission from CSEM. The code may only be changed through "user files" that affect things like boundary conditions and source terms, or to make changes to port the code to a new platform. In both cases, the user should contact CSEM. In the Register sub-section, the prospective model suite user is asked to fill out a brief registration form with standard contact information. In addition, three text sections are requested: "Briefly outline the research that you propose to do with SWMF"; "How did you learn about SWMF and this web site for downloading a public distribution?"; "Comments or Questions?" Once this information was

supplied, the form was submitted for approval consideration. It appears that, if the application was approved, an account would be established, and a login ID and password requested in the registration form would be activated.

At that point, one would then click the "Download SWMF" tab in the Downloads section to acquire the software suite. In this sub-section, contents of a "tar" file provided in the download are listed. It includes source code, manuals, test case run files, test case output files, and test case output plots. Before clicking a link to download the tar file, the following statement is shown: "We distribute only the Most Recent Stable Release, chosen from automated runs over the last 30 days. Get the MRSR materials here." When I clicked on the link there, I was prompted for a login ID and password. My application was approved the day after its submission, and I was given a login ID and password with which I successfully passed through to the login page. The Most Recent Stable Release offered four files: README text file, SWMF code and documentation tar file, SWMF data files tar file, and CRASH (a related code) data files tar file. The statement shown said that the most stable version of SWMF was included, and contained the latest bug fixes, patches and features that were stable. I downloaded these files, and transferred the SWMF code/documentation tar file and the SWMF data tar file to the Maui High Performance Computing Center supercomputer called "mana" and placed them on my scratch ($WORKDIR) disk there.

D. Developing Experience with the SWMF Software Suite

My first action with the acquired SWMF software was to read and follow the provided README text file to "install" the SWMF and "create the manuals." The first instruction was to enter the SWMF software directory and to run a command "Config.pl –install" which apparently runs a segment of a Perl script to compile the software codes on the host system. To determine which compilers that the SWMF supports, I ran their command "Config.pl –compiler" and a list of compilers was generated. Not being familiar with the "mana" system, I investigated and found that the default "module" that governs commands includes the Intel compiler. I found that the Message Passing Interface (MPI) version of that compiler, using the default module, is mpif90. I therefore used the following version of the "install" script to attempt to compile the SWMF codes on mana: Config.pl –install –compiler=mpif90. I added the ",mpicc" compiler after "mpif90", also available on mana (under the Intel default module), but the command failed as the latter was not one of the compilers provided. I then tried the command without "mpicc" and script execution commenced. A lot of lines of text was generated, much of which unintelligible to me, but near the end the text line "Installation complete" was issued. I did not know where to find executable files that may have been created so at that point I was not able to confirm a successful compilation of the software codes.

I next attempted to follow the README instructions to "create the manuals." I was able to confirm that the procedure "ps2pdf" was available on mana, and being satisfied with a PDF version of the manuals, I followed the direction and typed "make PDF." This process printed some text output before stalling at a point where the text indicated that a necessary file was not found – yet it appeared to be one of their files and that it was related to creating an HTML document which I did not request (the instructions say that is accomplished in the command "make HTML"). In any case, no desired PDF manuals were created in the "doc" directory, so I contacted the person at CSEM that had helped me with acquiring the software from their web site – he is the webmaster. He told me that he was not familiar with the process of creating the

manuals, and they had been having some problems with it. He advised me to download the single document available in the SWMF web page link "Documentation" called "Space Weather Modeling Framework User Manual" for Code Version 2.2 and dated July 25, 2007. The consultant confirmed that this was the most current version of the user manual. Subsequently, the webmaster informed me that a new set of manuals, dated April 2013, was available at a link which he supplied. I was able to download the new set, which included the newest version of the "Space Weather Modeling Framework User Manual" subtitled "Code Version 2.3."

The next step was to act on the recommendation in the README file to run the "standard test suite" about which there is no information supplied. Because the instructions indicated that multiple computing cores were required, I wrote a batch script that executed a command script that put command into the main SWMF directory, then ran the single recommended statement "make test MPIRUN=`mpirun –np 4`." I submitted the batch script and the job ran for multiple wallclock time hours. I contacted the webmaster and he referred me to Dr. Gabor Tóth, who wrote back to point out words at the end of the README file: "the results of the test are summarized in test_swmf.res – successful passing of the test is indicated by *.diff files." Dr. Tóth included a test_swmf.res file that he had just created that I could use as a reference for the one I had generated. They list many files that are created produced by the Unix "diff" command that compares many compilations that my test run attempted with standard compilation results. It appears that the *.diff files exist for many basic model function codes (like test_freq, test_coord_transform, test_axes, test_io_unit, etc.) and for specific tests of certain combinations of the SWMF components (like test1_pw.diff, test1_ie.diff, test1_gm.diff). Each non-zero *.diff file indicates some type of inability of the standard test suite to match their reference, usually resulting from failing to compile a code. This is apparent from listings of the *.diff files later in test_swmf.res. In the *.diff files for the function codes, Tóth's test_swmf.res showed about 9% that were non-zero while my test_swmf.res listed 37% non-zero. In looking at the subsequent listing of these, some of them include mention of "compile" (e.g., test_cometfluids_compile…). Dr. Tóth told me in his message that when the *.diff file contains "compile" it means that the test did not compile. Others, like test_func.diff (which was zero for him) listed repeated error messages of some sort (*filename* could not be opened). In regards to the tests of the SWMF components, there were multiple components included in each test (like the test1 example given above). Of the nine multiple component tests listed, at least one component had a non-zero *.diff file in three of them for Dr. Tóth, while seven tests had non-zero *.diff files in them in my experience. Interestingly, the SWMF component name in the *.diff files did not necessary lead to a failure in every test in which it was involved. For example, test1_gm.diff, where "gm" represents the global magnetosphere (GM) component, was non-zero (including "test1_compile…" and "test1_rundir…") whereas test2_gm.diff was zero in size (indicating no difference from the standard). This suggests that the GM code itself may not have been a problem, but it was perhaps that a code item included in test1 may not have compiled. As a final attempt, I repeated the test with the command "make test MPIRUN=`mpirun –np 2`" to see if using just two processors made a difference in the outcome. This time eight of the tests contained non-zero *.diff files. In the np=4 case, test3 seemed to compile and run but printed a truncated *.diff numerical output from standard, while in np=2 test8 had that experience. Overall, the tests did not seem consistent among three attempts, suggesting an unfortunate sensitivity among them. It didn't seem profitable to continue to pursue this, so I turned to begin reading the SWMF User Manual Code Version 2.3. My notes of the User Manual are included in the document "SWMF_User_Manual_Note_20130513."

E. Experience with SWMF Tests and Independent Execution

In an attempt to determine my level of understanding of the basics of the SWMF modeling system as described in the User Manual, I first conducted two of the recommended modeling tests. The README file of the downloaded distribution as mentioned in the third paragraph of Section D above encourages the reader to conduct the overall test of SWMF, what I called the "standard test suite." I downloaded a fresh installation of the SWMF software onto the "riptide" supercomputer at the Maui High Performance Computing Center (MHPCC). I first enacted the Config.pl command to utilize the mpiifort compiler. In the shell script I mentioned in Section D, I again ran the command "make test MPIRUN=`mpirun –np 4`." This time, the resulting *.diff files indicating differences from the reference outputs indicated that three tests had zero length files indicating a match with the reference – (test 2, test 7 and test 9). Test 2 is of particular interest to this project, because it involves the two components SC and IH in its first execution (governed by PARAM.in.test.SCIH) followed by interaction between the two components IH and GM in a restart execution. I therefore established a new directory from the downloaded software and called it SWMF_Test2. In this directory, I configured the executable file SWMF.exe with the Config.pl command, again using the mpiifort compiler, but specifying the three components involved: GM/BATSRUS, IH/BATSRUS, and SC/BATSRUS. I then executed the Test 2 experiment in the shell script with the command "make test2 MPIRUN=`mpirun –np 4`." I was able to follow the actions of the canned test2 script recorded in the combined standard error/standard output file I called swmf_Test2_0710.log. Interestingly, their script included, before the compilation of SWMF from GM, IH, and SC, the following included in three sequential Config.pl commands:
./Config.pl -v=Empty,SC/BATSRUS,IH/BATSRUS,GM/BATSRUS
./Config.pl -o=SC:u=Sc,e=MhdCorona,IH:u=Ih,e=Mhd,GM:u=Default,e=Mhd
./Config.pl -g=SC:4,4,4,6200,1,IH:8,8,8,400,1,GM:8,8,8,700,1
The second and third lines indicate specific forms of the components and computational grid for each one. After their compilation, PARAM.in.test.SCIH and LAYOUT.in.test.SCIH were brought into the "run_test" subdirectory in which SWMF.exe was to be executed to govern the first phase of the test. This involved setting up parameters for SC and IH, disabling IH and running SC in steady state 100 time steps, making a modification and running another 100 time steps, then turning on IH and coupling SC and IH for one time step to pass information to-from both components, and finally turning off SC and integrating IH in steady state for 100 time steps. The output from IH was saved at that point. With that execution finished, the script brought in PARAM.in.test.IHGM and LAYOUT.in.test.IHGM and then executed SWMF.exe again, this time directed by the instructions and parameter settings in these files. The saved files from the last time step of the previous IH integration was provided along with its parameters, and parameters were specified for GM. Then a one-way coupling of information from IH to GM was accomplished during the first of 100 time steps integrated by the GM component, while IH was prevented from integrating forward.

I then tested my understanding of the execution basics by setting up a new SWMF directory that I called SWMF_SCIH. My intention was to set up a script that would mimic Test 2 with basic commands explained by the SWMF User Manual. First, I repeated the same three Config.pl commands given above in SWMF_SCIH to be sure that I was using the same model components and computational grids. Then I constructed a script called run_swmf_SCIH.csh

that first executes the make command for overall compilation of SWMF.exe based on the GM, IH, and SC components. I then ran "make PIDL" to create the executable bin/PostIDL.exe that would produce images from output files from each of the components. Next, the script included the command "make EARTH_TRAJ" to create the executable bin/EARTH_TRAJ.exe to supply data for the component IH/BATSRUS. It then created the "run" directory and moved the necessary executables, post-processor and restart scripts, and component subdirectories needed for the execution of SWMF.exe for both SC-IH and IH-GM phases. Next the PARAM.in and LAYOUT.in files were brought into what I had called the "run_scih" directory for the SC-IH phase, and then executed EARTH_TRAJ.exe to create earth_traj.dat needed by IH. Now we were ready for the SC-IH mode of SWMF.exe, which I ran in 16 processors in SWMF_SCIH to see if it would run properly. The resulting "runlog" file created by the execution confirmed that 16 cores were used and that the SC-IH phase ran to completion.

The final three steps in the run_swmf_SCIH.csh script was: post-process the output files from SC and IH to produce the image files; run the Restart.pl procedure to set up the "restart tree" directory that I called RESTART_scih having the last time step values from IH in 16 files from the processors, and a RESTART.out file to be used as an #INCLUDE file in the PARAM.in file for the subsequent IH-GM SWMF.exe execution; confirm that the log files from SC and IH were identical to the Test 2 results resulting in zero length *.diff files. With respect to post-processing, I found that the usual PostProc.pl script does not allow for preserving the original *.idl files directly produced by the component models, and that it was necessary to run the command ./pIDL –k –m –v > pIDL_out.txt within both the SC and IH subdirectories in run_scih to preserve them. What pIDL does is to collect the *.idl files from each of the processors and combine them into a single *.out file for each output time specified in the PARAM.in file. With the –m option, it can then collect the resulting *.out files for all output times and make an animation called a *.outs file. At the time of this writing, I did not know the format of any of these files, and the SWMF User Manual does not explain them. I made a request to CSEM personnel for information describing IDL post-processing from SWMF outputs.

Once I was able to confirm that run_swmf_SCIH.csh did replicate the SC-IH phase of Test 2, I then made a script called run_swmf_IHGM.csh that would conduct the IH-GM phase of Test 2. I used the same parent directory, SWMF_SCIH, and the same run directory, run_scih, so I did not have to recompile code. Therefore, I simply had to copy in the relevant PARAM.in and LAYOUT.in files to supply parameters for IH and GM and direct the execution. Then as with the SC-IH phase, I ran the execution with the command "mpirun –np 16 ./SWMF.exe > runlog." After the execution, I ran the post-processing command "./pIDL –k –m –v > pIDL_out.txt" in the GM subdirectory of run_scih that contained the 16 *.idl files, which created a *.out for each set, followed by a single *.outs animation file. They were copied to a RESULTS/restart directory along with the log file from the GM component integration. The script Restart.pl then moved the saved files containing the last time step data from the GM integration, along with the accompanying RESTART.out file, to RESULTS/restart/RESTART in case another execution would be begun from the end stage of GM. Finally, the GM log file was compared with that of the corresponding Test 2 log file, and was found to be identical resulting in a zero length *.diff file.

I also attempted to run some example executions, for Example 1 and Example 2, as described in Chapter 4 of the SWMF User Manual. Section 4.1 reviewed the configuration of the desired version of SWMF using Config.pl and the compilation of the subsequent model components using "make." Interactively, I set up a "master" SWMF directory called

SWMF_Ex1-2 on the Maui High Performance Computer Center supercomputer called "riptide" on their $WORKDIR directory. In anticipation of conducting the experiments of Example 1 and 2, I selected the components GM/BATSRUS, IH/BATSRUS_share, and SC/BATSRUS for the configuration of SWMF as instructed in the manual. Apparently, the necessary software for IH/BATSRUS_share was not included in the current release, because the configuration check after running ./Config.pl displayed the following error for IH:
make: *** No rule to make target `srcBATL/BATL_size.f90'. Stop.
BATSRUS/Config.pl ERROR: could not open srcBATL/BATL_size.f90
I sent a request to CSEM personnel to check on the availability of the necessary IH/BATSRUS_share software in the release. I was informed by reply that the experiments in Chapter 4 were out of date and many of the files mentioned are obsolete. So I included IH/BATSRUS in the configuration of SWMF.exe. I ran an experiment run_swmf_Ex1 in which I ran 200 steps of SC, removing any mention of IH in the PARAM.in.test.SCIH file used in SWMF Test 2. I saved the restart at the end of the execution. Then I ran an experiment run_swmf_Ex2 commanded by PARAM.in.test.restart.SCIH to two-way couple SC-IH every 100 time steps and keep SC activated but only run it at 100 time step intervals (for coupling). I then ran the code (SC and IH) for 200 more time steps.

I next attempted to create two-dimensional plots of the output data created by the #SAVEPLOT commands in PARAM.in.test.SC (for SC) and PARAM.in.test.restart.SCIH (for IH) in which I used the plotform = idl_ascii parameter in each of the three plotarea plot types that I requested: x=0, y=0, and z=0 planes of the computational domain. I brought the resulting ASCII files created by the script pIDL with the names x=0_mhd_1_n0000200.out, y=0_mhd_2_n0000200.out, z=0_mhd_3_n0000200.out, for the nIteration = 200 computational iterations completed for both SC and IH, back to my home Linux workstation that has an IDL license. I also brought back the GM/BATSRUS/Idl sub-directory in the SWMF software to create the plots. In following the directions in the "IDL Visualization" section of an older manual named USERMANUAL.pdf provided to me by CSEM personnel, I found that the SWMF software plotting codes contained many functions that were not included in the sub-directory and were not inherent IDL algorithms. Therefore, I was unable to run their codes to create the desired plots. I requested and updated IDL code sub-directory from CSEM, but I was also prepared to write new IDL plotting codes in the near future to generate the plots that I desired to make.

F. Understanding the Process for Setting Initial and Boundary Values in SC and IH

A primary goal of this project is to determine the steps that existing solar corona and inner heliosphere numerical models take to set boundary values and initial values for subsequent integration. Once understood, the plan was to follow a similar approach in providing initial and boundary values for the prototype solar dynamo SC and IH components. I took the following three sequential actions to attempt to accomplish this goal. First, I again reviewed some of the journal articles describing SWMF, as mentioned in the literature review and Section B above, for relevant descriptions of setting boundary and initial values. Second, I thoroughly studied the file PARAM.in.test.SCIH and the SC-IH phase runlog from the SWMF_SCIH experiment, along with consulting Chapter 5 of the User Manual, for information that might provide clues on how initial and boundary values were set for the executions of SC and IH. Third, I contacted CSEM personnel about my specific interest and asked if there was someone who could provide me with

additional needed information. The following sub-sections relate what I found from these investigative actions.

1. SMWF SC and IH Published Literature

The SWMF component SC serves as the base for the interaction between Sun and Earth. This component simulates the plasma characteristics and magnetic field configuration of the solar corona based on realistic conditions of the solar photosphere and chromosphere. To start the SC integration, initial values must be imposed on its computational grid including its inner boundary nearest to the Sun. According to Tóth et al. (2005), plasma density, pressure and velocity are specified on the inner boundary positioned near the photosphere. A magnetogram of the photosphere, with grid point values of the radial magnetic field, can be used to set magnetic field values on the inner boundary. If the imposed boundary values are held constant on the inner boundary during the integration, the simulation is considered to be in steady-state mode. Constant forcing from the Sun should establish a physically consistent corona configuration through convergence of the model solution. In this case SC performs a sequence of time steps but the solution is never considered time dependent. If the values on the inner boundary are allowed to change with time, by supplying temporally varying values that may have been interpolated to time steps between intervals of the photospheric state, then the solution of SC is said to be time accurate. For simplicity in this discussion, we will consider only the steady-state mode.

If the inner boundary values are going to remain constant with time, their distribution around the Sun must be physically consistent with the coronal state to be simulated on a given date. The magnetogram based on photospheric magnetic field measurements preceding and on that date will ensure that the radial magnetic field boundary values are sound. But what about the plasma characteristic distribution on the inner boundary? Tóth et al. (2005) states that those conditions "may vary with longitude and latitude to achieve the most realistic solar wind near the Sun and at 1AU." Since solar wind changes in time and space continuously in the heliosphere, this implies that the plasma boundary values must be imposed in a distribution that is also representative of the case to be simulated. Tóth et al. (2005) does not address how this requirement is met.

Downs et al. (2010) considered formulations for the thermodynamic energy equation in the SWMF SC model to investigate energy transport mechanisms in the lower corona. In describing the basic SC component, they mention the research reported by Cohen et al. (2007) that they state constituted the "standard SC model." Because it was considered a standard version of the component, I studied the method used in the Cohen et al. (2007) to provide boundary and initial values for SC. In their research on coronal heating processes and the consequent plasma acceleration manifest in solar wind, they seek to improve the steady-state simulations of the SC and IH components. They use the corona magnetic field distribution produced by the Wang-Sheeley-Arge (WSA, Arge et al., 2004) model as initial conditions for the SC component, which they then use to attempt to simulate the coronal heating and solar wind expansion into the inner heliosphere. WSA inputs a photospheric magnetogram, either for a complete Carrington rotation of the Sun (over ~27 days) or that is updated daily using the current day's magnetographs of line-of-sight magnetic field. WSA uses the potential field source surface (PFSS) model (Altschuler and Newkirk, 1969) to expand the radial magnetic field onto a spherical grid from the surface of the photosphere ($r = R_s$) to a source surface at $r = 2.5\ R_s$. WSA uses the magnetic

field at the photosphere and at the source surface to compute an expansion factor. It then uses an empirical expression of the expansion factor and the angular distance of open flux tubes from coronal hole boundaries to compute radial solar wind speed on the source surface. In incorporating the source surface solar wind speed into the initial values of the SC model, Cohen et al. (2007) relates it to the spatial distribution of the Bernoulli integral throughout the corona and inner heliosphere. The integral is the work done by plasma expansion from the pressure at a given radial distance from the Sun to zero pressure, which is equal to the total energy of the plasma parcel at that position. Conserving total energy along a solar wind streamline and assuming adiabatic expansion, Cohen et al. (2007) derive an expression for the polytropic index γ at the inner boundary of SC (that is, $r = R_s$) in terms of the coronal base temperature and the source surface solar wind speed given by the WSA expression.

Cohen et al. (2007) explained how they used a Carrington rotation magnetogram to provide initial values for the SC model simulation in a steady-state mode. They derive the initial values of the radial magnetic field from R_s to the source surface 2.5 R_s from the PFSS model applied to the magnetogram. Then the empirical expression computes the source surface solar wind speed by tracing the potential field line through each grid point. The polytropic index is computed at the footpoint R_s using the expression mentioned above and assuming a constant coronal base temperature. The for each grid point, the polytropic index is interpolated outward from R_s to the source surface value of $\gamma = 1.1$. Beyond that point, on grid points out to 12.5 R_s, γ is interpolated to 1.5 and then set at 1.5 above 12.5 R_s. Near the current sheet, γ is set to 1.1 since the Bernoulli integral approach does not hold true.

Cohen et al. (2007) assumed a constant temperature for the inner boundary values of the SC. For the plasma density, the inner boundary values are set at each grid point to be a factor of 1×10^9 cm^{-3} in which the factor is the square of the ratio of the overall minimum source surface wind speed and the actual source surface wind speed. Thus the faster solar wind in open field lines has a smaller base density that the slow wind in closed field lines.

Downs et al. (2010) used the PFSS model in a similar way to provide initial magnetic field values for SC. They also mention the Cohen et al. (2007) use of the WSA model for SC initial conditions, implying that it is used in their simulation as well. With their focus on the lower corona, they used two different methods to prescribe inner boundary values of temperature and density. In the simpler method, they used uniform values characteristic of the lower chromosphere. In the other method, they assumed heat balance between the higher temperature of the transition region and the top of the chromosphere, and integrated the thermodynamic equation from chromosphere top to high transition region to obtain a variable inner boundary density.

van der Holst et al. (2010) provide initial values of the magnetic field in the corona by starting with a Carrington rotation GONG magnetogram to supply the radial magnetic field at the photosphere. The PFSS model solves the Laplace equation for the potential field Φ that matches the magnetogram at the photosphere and is set to zero (assumes a strictly radial magnetic field B) at the source surface. The gradient of the resulting spherical harmonics for $\Phi(r,\theta,\varphi)$, which constitute the harmonics of the radial, latitudinal, and longitudinal components of B, is usually evaluated by spherical harmonic expansion using a limited number of harmonics at each grid point location. The SC computational grid is spherical that is staggered, with the potential field at the grid cell center and the magnetic field on the cell faces. van der Holst (2010) evaluated the potential field solution with a limited number of harmonics, then used a finite difference method

called Bi-CGSTAB to compute the magnetic field components rather than the spherical harmonic expansion in the B components.

The resulting magnetic field is used as the initial conditions for SC in the corona between R_s and the source surface $R_{ss} = 2.5\ R_s$. From R_{ss} to the outer boundary of SC the initial magnetic field is the strictly radial component at R_{ss}. In their numerical solution of magnetic field in SC, they solve for the departure of magnetic field from the initial magnetic field imposed from the PFSS model. No assumption is made that the departure is small compared to the initial magnetic field in their splitting scheme. The steady-state solution implies that the departure from the radial magnetic field at the inner boundary, set at $r = 1.035\ R_s$, remains zero. The magnetic field solution in the corona evolves in the simulation and will differ from the PFSS initial condition configuration.

van der Holst et al. (2010) set the inner boundary conditions of density and electron temperature for their version of the SC model using differential emission measure topography (DEMT) applied to extreme ultraviolet imagery. They use the WSA model to obtain an estimate of the radial solar wind speed at 1 AU, starting with the PFSS model solution. The resulting magnetic field lines are used to compute the flux tube expansion factor at the 2.5 R_s source surface. The PFSS model solution includes coronal holes with open field lines, and the field lines are also used to compute the angular distance in latitude and longitude between the field line foot point at R_s and the nearest coronal hole boundary. Then the expansion factor and angular distance at each grid point latitude-longitude position are used in the WSA model empirical expression tuned to GONG magnetograms to estimate the radial solar wind speed at the source surface. They assume that the same grid point distribution of radial solar wind speed is also applicable to 1 AU. This they use to compute the Alfvén wave pressure at the inner SC boundary.

In the setup of the SC and IH components for their experiments, van der Holst et al. (2010) changed the polytropic index from the value of $\gamma = 1.5$ used by Cohen et al. (2007) to a value of $\gamma = 5/3$. This newer version is available in the SWMF software suite. The SC model computational domain extends from -24 R_s (behind the Sun) to 24 R_s (earthward of Sun) in a Cartesian grid framework. The computational grid was make up of blocks in each of the x, y and z directions having four grid cells in each direction, a total of 64 grid cells. The computational grid cells within the blocks have a width of about 16,300 km nearest the inner boundary and increase to about 525,000 km at the outer boundary. van der Holst et al. (2010) state that they use "Parker's hydrodynamic isothermal solar wind solution (Parker, 1958)" to provide initial conditions for the solar wind. This "spherically symmetric hydrodynamic expansion velocity" (Parker, 1958) is a function of the radial direction only, and is parameterized for selected values of the isothermal temperature. The PFSS solution is assigned as the initial conditions for the magnetic field out to 2.5 R_s, and the 2.5 R_s strictly radial values are extended out to the outer boundary as mentioned above. They execute the governing equations in a heliographic rotating frame to steady-state subject to the boundary conditions mentioned above. Adaptive mesh refinement (AMR) is applied to the heliospheric current sheet as the solution converges to the steady-state. The SWMF component IH solves for the magnetic field and plasma conditions from the outer boundary of the corona through the inner heliosphere. van der Holst et al. (2010) set the inner boundary of IH at 16 R_s out to a radial distance of 250 R_s in x, y, and z on all sides of the Sun. This results in an overlap of SC and IH domains between 16 and 24 R_s. IH inner boundary conditions are acquired from these overlapping regions of the SC component through a coupling. They used four Cartesian computational blocks in all three coordinates, with

increasingly larger grid cells from about 343,000 km to 2.73 M km from inner to outer boundaries.

Evans et al. (2012) used the same method to specify the initial and boundary values for experiments with their version of the SWMF SC component. They make it clear that the isothermal Parker solar wind solution (Parker, 1958) is used to specify initial conditions for the single-fluid plasma density and the solar wind speed. A factor of 1.8 was applied to the radial magnetic field strength to the GONG photospheric magnetogram because of its coarse spatial resolution. Evans et al. (2012) used the PFSS model to compute the magnetic field out to the source surface of $R_{ss} = 2.5 R_s$. It is assumed that they carried the radial magnetic field out to the outer boundary at 24 R_s following van der Holst et al. (2010). DEMT was used to provide inner boundary conditions for the density and temperature. They also follow van der Holst et al. (2010) in using the WSA model to estimate radial solar wind speed at 1 AU to compute the wave energy at the inner boundary of SC in areas of open field lines (it is set to zero at closed field lines). The same 64 cells per block were used as in the SC component for van der Holst et al. (2010). The smallest cells within the blocks with a width of 16,400 km were positioned at the inner boundary, and the heliospheric current sheet was resolved with cells with a width of about 65,600 km.

Sokolov et al. (2013) use a Carrington rotation magnetogram from the Helioseismic and Magnetic Imager (HMI) from the Solar Dynamics Observatory (SDO) to supply data-driven inner boundary values of the magnetic field. The magnetic grid has a latitude-longitude spacing of 0.1°. They solve for the coronal potential field from the magnetogram using the Finite Difference Iterative Potenial-field Solver (FDIPS) as an alternative to the PFSS model. This supplies the initial values of the magnetic field throughout the domain of the SC component. Another difference is that they used a spherical grid in place of a Cartesian grid. The SWMF SC component is set to have an inner boundary at 1 R_s and an outer boundary of 20 R_s. They used a total of 250,000 computational blocks each having 6 cells in radial, 4 in latitudinal and 4 in longitudinal directions. The cell widths ranged from 700 km to 560,000 km, and used AMR to resolve the heliospheric current sheet. No mention by the authors is made of specifying the inner boundary values of density or temperature, nor the initial values of the radial solar wind speed. Sokolov et al. (2013) do mention that they set the boundary condition for temperature and density at the top of the chromosphere to constant values, but its relationship to SC inner boundaries is not clear.

2. SWMF User Manual Documentation

Chapter 5 of the SWMF User Manual gives a description of the commands and parameters available for use in the PARAM.in file that directs a SWMF.exe execution. I read and documented commands and accompanying parameters that were relevant to SC and IH operation. My notes are in "Chapter 5" of the SWMF_User_Manual_Notes_20130513.docx document. Much of the documentation deals with general commands intended for directing the control module of SWMF, as in Section 5.1. The only discussion relevant to initial and boundary values in that section was the #STARTTIME command, in which the exact actual date and time of model simulation should begin. This would have to be the valid date and time of the initial and boundary values for the execution. The commands specific to the BATSRUS components, including SC and IH, were described in Section 5.2. Though I gleaned much information from this section that was not directly related, I did take special note of the facets

that were relevant to imposing initial and boundary values for SC and IH. I consulted with the PARAM.in.test.SCIH sections specific to SC and IH to see which commands were actually used in the test run of the components that I accomplished as a check on their relevance.

The first was Sub-Section 5.2.5, Initial and Boundary Conditions. I distinguish initial and boundary conditions from initial and boundary values in that the former is design used for the model formulation, while the latter describes physical MHD variable values provided to populate the computational grid before execution begins. While the latter is more our interest, there were some aspects of initial and boundary conditions for the model that were pertinent. One is the TypeIoUnit parameter in the #IOUNITS command. The choice of the parameter dictates the physical units of the parameters, including any imposed boundary conditions, read from the PARAM.in file. In the case of our PARAM.in file, #IOUNITS was not listed which meant that the default TypeIoUnit = HELIOSPHERIC was in force, where the units are: distance in solar radius, time in seconds, speed in km s^{-1}, angles in degrees, and centigrade-gram-seconds units for density (mass and number), pressure, magnetic field, and current. Another command imposing boundary conditions for SC or IH is #OUTERBOUNDARY, which as its name implies sets the formulation for the outer boundary of the component's computational domain. For a Cartesian grid there can be parameters set for each of the six outer boundary faces. The major boundary condition options are: "float" or "outflow", a zero gradient of the MHD values across a boundary; "vary" or "inflow" for time dependent boundary conditions when the component is executed in time accurate mode with another component on its outer boundary; "fixed" when constant MHD values are imposed on the outer boundary and are held constant during the component execution. In the case of the experiments conducted by van der Holst et al. (2010), they used the "float" parameter on their outer boundary, and assumed a zero gradient for all the MHD variables. The same was true in our PARAM.in for both SC and IH. The counterpart command is #INNERBOUNDARY, which determines the function of the cells lying on the Sun-most sides of the computational grid. There is only a single parameter for this command called TypeBcInner with the options of: "float", a zero gradient of MHD variables across the inner boundary regardless if they are steady-state or time-varying; "coronatoih" for the IH component that indicates its inner boundary is supplied from the coupling with SC. In our PARAM.in file, no explicit #INNERBOUNDARY command was issued for SC, even though the documentation clearly states that SC and IH executions must have the command. At this point my assumption is that it was superseded by "MAGNETOGRAM" command (to be discussed below) that would have supplied inner boundary values. However, the IH component section of PARAM.in that coupled with SC and then ran a subsequent integration did use TypeBcInner = coronatoih. Also, in my Example 2 experience in which I ran a restart of SC to couple with IH and then IH ran 200 iterations and SC ran only at 100 iteration intervals, I had to supply a #INNERBOUNDARY parameter value of TypeBcInner = float for the SC section of PARAM.in so that SC could run. This necessity lends credence to my assumption that #MAGNETOGRAM must have taken care of dictating the inner boundary conditions for SC in its initial integration.

At this point, I had to skip down in the SWMF Chapter 5 documentation to just the commands in PARAM.in.test.SCIH ("PARAM.in file") relevant to boundary values and initial values. Within the BEGIN_COMP SC section of the PARAM.in file, the first command that dictates boundary and initial values is MAGNETOGRAM. Its parameters are explained in Sub-Section 5.2.15, "Corona Specific Commands." If its first parameter is "True", SC is directed to input a file for the spherical harmonics of the coronal magnetic field that is previously derived from a photospheric magnetogram by the PFSS model. From these spherical harmonics

coefficients, the model can determine the three components of the magnetic field at each grid point from the photosphere to the source surface in accordance to the potential field solution. At the source surface, only the radial component of the magnetic field is nonzero. The next two parameters are the radial distance of the photosphere and the source surface, which are usually set to 1.0 and 2.5 respectively. Next is the radial distance of the inner boundary surface above the photosphere, set to zero in most cases. The next two parameters are the file name of the spherical harmonics coefficients specific to a magnetogram (either by Carrington rotation or daily update) and its number of header lines. The magnetogram coefficients must be prepared in advance of the SC execution, so the PFSS model must be applied to the magnetogram of photospheric radial magnetic field on a regular grid. A parameter called PhiShift can be provided to give the longitude difference between the magnetogram central meridian (in Carrington longitude) and 180°. Setting PhiShift = -1.0 causes the code to determine the central meridian coordinate from the spherical harmonics file. A final parameter allows the user to change the magnitude of the magnetogram data for use in SC.

There were no other indications of setting initial or boundary values in the PARAM.in commands as listed in the SWMF User Manual or in PARAM.in.test.SCIH. I assume from this that some of the initial value settings described in Section F.1. above must be included in the model code. An example of this is the Parker solar wind solution (Parker, 1958) in which radial solar wind speed is set as a function of the radial component only. The statement of van der Holst et al. (2010) that the initial solar wind speed is "parameterized" for selected isothermal temperatures indicates that code was added to accommodate this.

3. CESM Personnel

Darren DeZeeuw was helpful in answering questions about documentation availability, creating plots of SC and IH outputs, and how to identify SWMF code most relevant to setting initial and boundary values. For example, since the MAGNETOGRAM input to SC was in spherical harmonics coefficients which would have needed to be generated in advance, I asked him if the PFSS model would be available through the SWMF release. I will continue to direct my questions to him as I seek to understand the specification of initial and boundary values in SC and IH.

G. References

Altschuler, M. D., and G. Newkirk, Jr. (1969), Magnetic fields and the structure of the solar corona. I: Methods of calculating coronal fields, *Solar Phys.*, **9**, 131-149, doi:10.1007/BF00145734.

Arge, C. N., J. G. Luhmann, D. Odstrcil, C. J. Schrijver and Y. Li (2004), Stream structure and coronal sources of the solar wind during the May 12th, 1997 CME, *J. Atmos. Sol. Terr. Phys.*, **66**, 1295-1309, doi:10.1016/j.jastp.2004.03.018.

Cohen, O., I. V. Sokolov, I. I. Roussev, C. N. Arge, W. B. Manchester, T. I. Gombosi, R. A. Frazin, H. Park, M. D. Butala, F. Kamalabadi, and M. Velli (2007), A semiempirical magnetohydrodynamical model of the solar wind, *Astrophys. J.*, **654**, L163-L166, doi: 10.1086/511154.

Downs, C., I. I. Roussev, B. van der Holst, N. Lugaz, I. V. Sokolov, and T. I. Gombosi (2010), Toward a realistic thermodynamic magnetohydrodynamic model of the global solar corona, *Astrophys. J.*, **712**, 1219-1231, doi:10.1088/0004-637X/712/2/1219.

Evans, R. M., M. Opher, R. Oran, B. van der Holst, I. V. Sokolov, R. Frazin, T. I. Gombosi, and A. Vásquez (2012), Coronal heating by surface Alfvén wave damping: Implementation in a global magnetohydrodynamics model of the solar wind, *Astrophys. J.*, **756**, 155-167, doi:10.1088/0004-637X/756/2/155.

Gombosi, T. I., G. Tóth, D. L. De Zeeuw, K. G. Powell, and Q. F. Stout (2001), Adaptive mesh refinement MHD for global simulations, *Proceedings of ISSS-6*, J. Büchner, C. T. Dum, and M. Scholer, eds., Copernicus Gesellschaft, 1-8.

Groth, C. P. T., D. L. De Zeeuw, T. I. Gombosi, and T. I. Gombosi (2000), Global three-dimensional MHD simulation of a space weather event: CME formation, interplanetary propagation, and interaction with the magnetosphere, J. Geophys. Res., 105, A11, 25053-25078, doi:10.1029/2000JA900093.

Parker, E. N. (1958), Dynamics of the interplanetary gas and magnetic fields, *Astrophys. J.*, **128**, 664-676, doi: 10.1086/146579.

Powell, K. G., P. L. Roe, T. J. Linde, T. I. Gombosi, and D. L. De Zeeuw (1999), A solution-adaptive upwind scheme for ideal magnetohydrodynamics, *J. Comput. Phys.*, **154**, 284-309, doi:10.1006/jcph.1999.6299.

Sokolov, I. V., B. van der Holst, R. Oran, C. Downs, I. I. Roussev, M. Jin, W. B. Manchester, R. M. Evans, and T. I. Gombosi (2013), Magnetohydrodynamic waves and coronal heating: unifying empirical and MHD turbulence models, *Astrophys. J.*, **764**, 23-35, doi:10.1088/0004-637X/764/1/23.

Tóth, G., and co-authors (2005), Space Weather Modeling Framework: A new tool for the space science community, *J. Geophys. Res.*, **110**, A12226, doi:10.1029/2005JA011126.

van Der Holst, B., W. B. Manchester, R. A. Frazin, A. M. Vasquez, G. Toth, and T. I. Gombosi (2010), A data-driven, two-temperature solar wind model with Alfvén waves, *Astrophys. J.*, **725**, 1373-1383, doi:10.1088/0004-637X/725/1/1373.

LIST OF SYMBOLS, ABBREVIATIONS, AND ACRONYMS

ACE	Advanced Composition Explorer
ASCII	American Standard Code for Information Interchange
AU	astronomical units
B	three-dimensional magnetic field
CME	coronal mass ejections
CORHEL	Coupled MAS and Enlin
CSEM	University of Michigan Center for Space of Environmental Modeling
GM	global magnetosphere
IDL	Interactive Data Language
IH	inner heliosphere
IMF	interplanetary magnetic field
MAS	Magnetohydrodynamics Around a Sphere
MHPCC	Maui High Performance Computing Center
MHD	magnetohydrodynamics
NiCT	National Institute of Information and Communication Technology
ρ	density
PFSS	potential field source surface
Rho	mass density
R_s	solar radii
SC	solar corona
SIP-AMR-CESE	Solar-Interplanetary Adaptive Mesh Refinement Space-Time Conservative Element and Solution Element
SWMF	Space Weather Modeling Framework
T	temperature
UTC	Coordinated Universal Time
V	plasma velocity
WSA	Wang-Sheeley-Arge

DISTRIBUTION LIST

DTIC/OCP
8725 John J. Kingman Rd, Suite 0944
Ft Belvoir, VA 22060-6218   1 cy

AFRL/RVIL
Kirtland AFB, NM 87117-5776   1 cy

Official Record Copy
AFRL/RDSM/Jeffrey Yepez   1 cy